An investigation of the role of mucin gels in disease progression and transmission

By

Nicole A. Bustos

B.S.
Carnegie Mellon University, 2017

S.M.
Massachusetts Institute of Technology, 2021

Submitted to the Department of Mechanical Engineering
in Partial Fulfillment of the Requirements for the Degree of

DOCTOR OF PHILOSOPHY IN MECHANICAL ENGINEERING

at the

MASSACHUSETTS INSTITUTE OF TECHNOLOGY

FEBRUARY 2024

Authored by: Nicole A. Bustos
Department of Mechanical Engineering
August 25, 2023
Certified by: Katharina Ribbeck
Professor of Biological Engineering, Thesis Supervisor
Accepted by: Nicolas Hadjiconstantinou
Chairman, Department Committee on Graduate Theses

An investigation of the role of mucin gels in disease progression and transmission

by

Nicole A. Bustos

Submitted to the Department of Mechanical Engineering

on August 25, 2023, in partial fulfillment of the requirements for the degree of

Doctor of Philosophy in Mechanical Engineering

Abstract

Mucus is a biological hydrogel that coats every wet epithelial surface of the body, including the respiratory tract. Within the body, mucus serves as a barrier: a mesh network made of mucin polymers that act as a size and biochemical filter, trapping small molecules, including pathogens. When mucus is cleared from the respiratory tract via exhalations such as coughing or sneezing, it can act as a vessel for infectious material from infected individuals that can be carried to other potential hosts or remain in the environment. The high shear rates associated with violent exhalations cause respiratory mucus to fragment into droplets spanning a range of sizes. Once emitted, droplets are propelled to nearby surfaces or entrained and advected in ambient air flows. Larger droplets may settle quickly to the ground, whereas smaller aerosolized droplets may remain suspended in the air and evaporate over time.

In this thesis, we investigate the role of mucins in these within-host and external disease processes. In mucosal layers within the host, mucus plays an important role in limiting the progression of infectious pathogens. The pathogen's ability to penetrate mucus, in many cases, determines its ability to reach its target cell and initiate infection before being cleared by the body. We begin by studying the impact of mucins on the transport of virus-sized particles. First, we examine the transport of bacteriophage, a model system for viruses, and nanoparticles of comparable size in reconstituted mucin gels simulating the respiratory tract and intestinal environment. Our findings reveal that phage have different transport abilities tied to their geometry, size, and surface chemistry. In addition, they are relatively unhindered in concentrated mucin gels compared to similar-sized nanoparticles. We show that in different phage populations, diffusive Brownian motion is associated with both Gaussian (normally distributed) and non-Gaussian population-level and particle-level step size distributions, which consequently impacts the spread and confinement of these particles in mucin gels. Moreover, we establish that the degree of Gaussianity is influenced by mucin type, suggesting that mucin-phage biochemical interactions play a significant role in phages' mucin specific transport, as opposed to differences in the mucin network structure.

Next, we study the effect of mucins and nanoparticles on the fragmentation dynamics of biological fluids. Polymers are known to shift and broaden the droplet size distributions of complex fluids compared to their Newtonian counterparts. Yet, the impact of mucus' main solid component, mucin, along with pathogens, on the size and dispersal of emitted droplets remains incompletely unresolved. We use varying concentrations of charged nanoparticles to simulate pathogen load in several mucus polymer model systems. This highlights the importance of incorporating native mucin properties and mucin-pathogen interactions in the modeling of biological fragmentation processes. Our measurements show that the shear rheology of mucin

gels are insensitive to the presence of particle load. On the other hand, the extensional rheological properties of mucin gels, including the characteristic relaxation time and thread lifetime, were greatly modified by suspensions of nanoparticles. Accordingly, the average droplet size of sprayed mucin gels is increased and the spatial distribution (depth and clustering) of droplets was shown to vary depending on particle charge. By comparison, other mucus polymer models did not recapitulate the same behaviors.

The findings of this thesis underscore the importance of pathogen-mucin dynamics across multiple length scales. Integrating mucosal barriers into experimental systems is crucial for understanding the mechanistic and biophysical principles underlying disease transmission and initial host infection.

Thesis supervisor: Katharina Ribbeck
Title: Professor, Biological Engineering, MIT

Thesis supervisor: Caroline Wagner
Title: Assistant Professor, Bioengineering, McGill

Acknowledgments

First and foremost, I would like to thank my advisors Katharina and Caroline for guidance, support, and understanding throughout my academic journey.

I would also like to thank my thesis committee, Gareth McKinley and Giovanni Traverso, for their feedback on my work.

To the Ribbeck Lab: thank you for answering my many questions, teaching me new techniques, and your thoughtful input on my work. I thank you for making this a great lab environment. I am especially thankful to George Degen, Chloe Wu, and Corey Stevens who I worked directly with on several projects.

Thanks to several members of the MIT community who I collaborated with to improve transitional support across MIT and who I worked with to develop advising resources for MechE graduate students. Thanks to the MechE Advising Working group: Vishnu, Noam, Crystal, Ippolyti, and April for all coming together to create resources and planning events to support MechE grad students. Thanks to Prof. Betar Gallant for supporting our efforts. Thanks to the Transitional Support Working Group, especially Prof. Anne E. White and Suraiya Baluch. Thank you for listening to my input, my experiences, and allowing me to be part of initiatives to improve advising.

Thank you to my MIT friends: Souha, Rishabh, Stephane, Sungkwon, Jack, and Sanghyun. To the ‘day ones’, although we went through a difficult time in our first few years together at MIT, I feel lucky to have met you all. You have all taught me so much.

To my family: thank you for your encouragement (“si se puede”), love, and prayers throughout my entire academic journey. It has not been an easy road; there were times when I doubted my abilities and was not confident that I could surmount the next challenge. You have given me much needed strength at times, either through your words or through old memories we share, to keep on going in this work. Thank you to my dad for inspiring my passion and curiosity around science and engineering. My enthusiasm for building devices/experimental setups and running experiments was born out of our time spent making a homemade rocket, a large-scale model of an animal cell, a 3-dimensional foldable board game, and many more projects.

To my fiancé, Alex: thank you for helping me smell the roses. There are times when I get so focused on what comes next in our lives and in our careers, but you remind me that *where I am now is where I once dreamed I would be*. I could not have made it through this journey without you, and I can’t wait to marry you.

Table of Contents

List of figures

Chapter 1

Introduction

When new respiratory infectious diseases emerge, questions arise surrounding how a given disease is transmitted among individuals; more specifically, questions concerning the pathogen load required to initiate infection in a susceptible individual and the mode of transmission (i.e. aerosol/airborne, droplet, or contact/fomite) which are both closely tied to the bio-physical processes that occur within hosts and external to hosts at the point of transmission (illustrated and summarized in **Figure 1.1**). Mucus barriers are critical components that influence disease pathogenesis and transmission via physicochemical interactions with viruses; mucus can modify the viral dynamics within hosts and the viability of viruses emitted from the respiratory tract of hosts in the form of mucosalivary droplets.

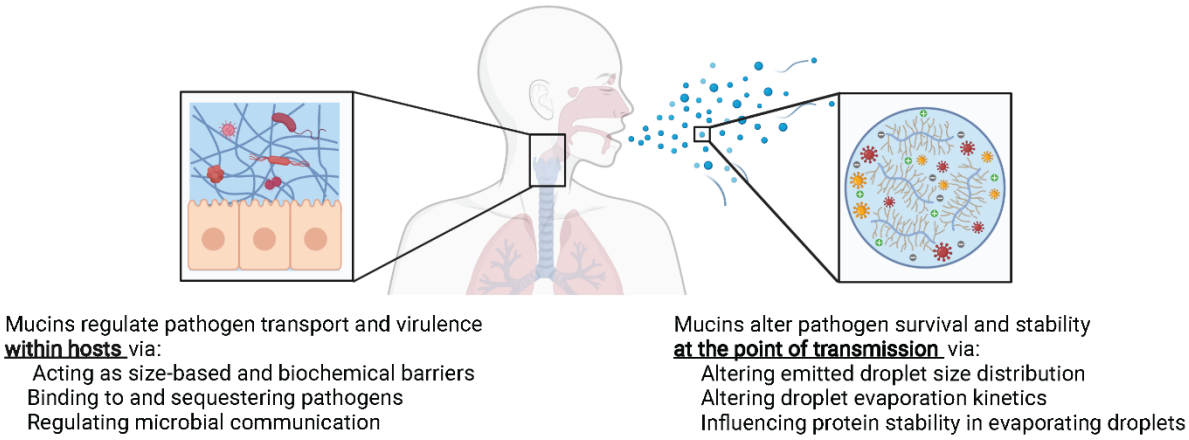

Figure 1.1 Mucins influence processes both within hosts and external to hosts at the point of transmission. The illustration demonstrates (left) a mucus layer lining epithelial cells with suspended bacteria and viruses and (right) droplets expelled from the respiratory tract containing a mixture of mucins, viruses, and ions.

Mucus is composed primarily of water (95%), salts (0.5-1%), lipids (1-2%), and proteins [1]. The primary structural component of mucus that is responsible for its viscoelastic properties is the glycoprotein mucin. Broadly, mucin is a negatively charged protein composed of a protein

backbone and glycan structures arranged in a bottlebrush-like fashion [1,2]. Together, mucins form a network of hydrated polymers maintained by physical entanglements, and cross-linking, a result of covalent and noncovalent interactions [3,4]. While different mucin types contain similar structures, individual mucins have specialized functions and roles depending on the regions where they are expressed. Respiratory mucus serves a multitude of functions; it maintains the lubricity and hydration of the underlying epithelial surface [5], protects against mechanical damage from shear-induced forces involved in swallowing and exhalation (e.g., coughing and sneezing) [6], and provides a 'first line of defense' against the external environment by trapping foreign and harmful substances (e.g., toxins, heavy metals, or biological substances such as pathogenic bacteria, viruses, or parasites) [7,8]. In a healthy respiratory tract, the steady production and shedding of mucus, mucociliary clearance, and innate immune defenses play a key role in protecting the respiratory system. However, in diseased airways, mucin hypersecretion, changes in mucin, or dysregulation of water and ions, often leads to thickened mucus and consequently poor mucociliary clearance [9–11]. This form of dysfunctional mucus is most notably seen in individuals who suffer from chronic respiratory diseases such as cystic fibrosis (CF). Poor mucociliary clearance prevents clearance of pathogens from the respiratory tract leading to repeated infection; CF patients experience frequent and prolonged courses of respiratory viral infections [12].

There is a significant interest in understanding the role of mucus and the coordination between different mucus components and pathogens in shaping both disease progression within-host and transmission between hosts; in particular, how do the physicochemical properties of mucus and the presence of pathogens set the dominant mode by which a pathogen spreads. Additionally, how do mucins affect the spatiotemporal distribution of pathogens in mucus layers and consequently pathogen load when pathogen-laden mucus is expelled from the body. Experimental studies with mucins have largely focused on "micro-scale" processes: for example, the transport or bulk diffusion of particles (e.g., nanoparticles [13], viruses [14], or bacteria [15]) through mucus, the microstructural organization of the polymer network [16,17], or the altered gene expression of pathogens in mucus [18]. Yet, the use of purified native mucins in "large-scale" experiments, in particular those modeling exhalations is limited. Frequently, the limited availability of purified native mucin results in the experimental use of commercial mucins or synthetic polymers as substitutes. However, these materials may show significant differences from mucins across length scales and may not recapitulate the unique bioactivity of human mucins (e.g., binding, antiviral and anti-bacterial properties) [17]. At

the macroscale, the bulk viscoelastic properties of mucus not only govern its ability to lubricate but also influence the way in which mucus breaks up and clears away pathogens. At smaller length scales, the microstructural organization and biochemical properties of mucin can impact the passage of small molecules, including drug-delivery vehicles. Within the body, mucin may act as a trap for pathogens, yet outside of the body, mucin may be advantageous to pathogens; mucosalivary droplets may act as vesicles shielding pathogens from the non-native conditions of the ambient environment.

Bridging the dynamics across both length scales, pathogen-mucin interactions within hosts and at the point of transmission is crucial to several aspects: our understanding of the biophysics of disease spread, building disease models, and informing public health guidelines. Therefore, the goal of this thesis is to study how mucins modulate the transport of virus-sized particles across mucus layers and how mucin-particle interactions influence the formation and dispersal of mucus droplets. We begin in **Chapter 2** by providing a literature review of the physicochemical features of mucus and its biological functions in the body, including how mucus layers filter pathogens. In particular, this chapter focuses on the properties of mucus' primary solid component, the mucin glycoprotein, and provides a discussion of mucin's role in disease transmission and its application to the "small-scale" and "large-scale" experimental systems used in this work. In **Chapter 3**, we investigate the physical transport of bacteriophage in reconstituted mucin gels using single particle tracking. We use bacteriophage as a virus model system to gain insight into how geometry and surface chemistry influences transport behavior. In **Chapter 4**, we provide background on the rheological characterization of viscoelastic fluids and discuss techniques and considerations for weakly viscoelastic fluids used in this work. In **Chapter 5**, we study the impact of bulk physical properties of mucin gels and suspensions of virus-sized particles on the breakup and dispersion of sprayed mucus; we additionally study common commercial mucus polymer models to highlight specific native mucin effects and discuss the biological implications of mucin-particle interactions on disease transmission. Finally, in **Chapter 6**, we provide concluding remarks and future directions.

1.1 References

[1] R. Bansil, B.S. Turner, The biology of mucus: Composition, synthesis and organization, Adv. Drug Deliv. Rev. 124 (2018) 3–15. https://doi.org/10.1016/j.addr.2017.09.023.

[2] R. Shogren, T.A. Gerken, N. Jentoft, Role of Glycosylation on the Conformation and Chain Dimensions of O-Linked Glycoproteins: Light-Scattering Studies of Ovine Submaxillary Mucin, Biochemistry. 28 (1989) 5525–5536. https://doi.org/10.1021/bi00439a029.

[3] J. Leal, H.D.C. Smyth, D. Ghosh, Physicochemical properties of mucus and their impact on transmucosal drug delivery, Int. J. Pharm. 532 (2017) 555–572. https://doi.org/10.1016/j.ijpharm.2017.09.018.

[4] O. Lieleg, K. Ribbeck, Biological hydrogels as selective diffusion barriers, Trends Cell Biol. 21 (2011) 543–551. https://doi.org/10.1016/j.tcb.2011.06.002.

[5] R. Bansil, E. Stanley, J. Thomas LaMont, Mucin biophysics, Annu. Rev. Physiol. 57 (1995) 635–657. https://doi.org/10.1146/annurev.ph.57.030195.003223.

[6] S. Girod, J.M. Zahm, C. Plotkowski, G. Beck, E. Puchelle, Role of the physicochemical properties of mucus in the protection of the respiratory epithelium, Eur. Respir. J. 5 (1992) 477–487.

[7] M. Zanin, P. Baviskar, R. Webster, R. Webby, The Interaction between Respiratory Pathogens and Mucus, Cell Host Microbe. 19 (2016) 159–168. https://doi.org/10.1016/j.chom.2016.01.001.

[8] S.K. Linden, P. Sutton, N.G. Karlsson, V. Korolik, M.A. McGuckin, Mucins in the mucosal barrier to infection, Mucosal Immunol. 1 (2008) 183–197. https://doi.org/10.1038/mi.2008.5.

[9] J. V. Fahy, B.F. Dickey, Airway Mucus Function and Dysfunction, N. Engl. J. Med. 363 (2010) 2233–2247. https://doi.org/10.1056/nejmra0910061.

[10] M.A. Khan, Z.A. Khan, M. Charles, P. Pratap, A. Naeem, Z. Siddiqui, N. Naqvi, S. Srivastava, Cytokine storm and mucus hypersecretion in COVID-19: Review of mechanisms, J. Inflamm. Res. 14 (2021) 175–189. https://doi.org/10.2147/JIR.S271292.

[11] M. Chatterjee, J.P.M. van Putten, K. Strijbis, Defensive Properties of Mucin Glycoproteins during Respiratory Infections — Relevance for SARS-CoV-2, MBio. 11 (2020) e02374-20.

[12] M.R. Kiedrowski, J.M. Bomberger, Viral-Bacterial Co-infections in the Cystic Fibrosis Respiratory Tract, Front. Immunol. 9 (2018) 1–12. https://doi.org/10.3389/fimmu.2018.03067.

[13] O. Lieleg, I. Vladescu, K. Ribbeck, Characterization of particle translocation through mucin hydrogels, Biophys. J. 98 (2010) 1782–1789. https://doi.org/10.1016/j.bpj.2010.01.012.

[14] L. Kaler, E. Iverson, S. Bader, D. Song, M.A. Scull, G.A. Duncan, Influenza A virus diffusion through mucus gel networks, Commun. Biol. 5 (2022) 1–9. https://doi.org/10.1038/s42003-022-03204-3.

[15] N.A. Licata, B. Mohari, C. Fuqua, S. Setayeshgar, Diffusion of Bacterial Cells in Porous

Media, Biophys. J. 110 (2016) 247–257. https://doi.org/10.1016/j.bpj.2015.09.035.

[16] C.E. Wagner, Micro- and macro-rheological studies of the structure and association dynamics of biopolymer gels, PhD Thesis. (2018).

[17] C.E. Wagner, M. Krupkin, K.B. Smith-Dupont, C.M. Wu, N.A. Bustos, J. Witten, K. Ribbeck, Comparison of Physicochemical Properties of Native Mucus and Reconstituted Mucin Gels, Biomacromolecules. 24 (2023) 628–639.

[18] J. Takagi, K. Aoki, B.S. Turner, S. Lamont, S. Lehoux, N. Kavanaugh, M. Gulati, A. Valle Arevalo, T.J. Lawrence, C.Y. Kim, B. Bakshi, M. Ishihara, C.J. Nobile, R.D. Cummings, D.J. Wozniak, M. Tiemeyer, R. Hevey, K. Ribbeck, Mucin O-glycans are natural inhibitors of Candida albicans pathogenicity, 2022. https://doi.org/10.1038/s41589-022-01035-1.

Chapter 2

Physicochemical properties of mucin gel networks

Given mucus' relevance to the majority of the work in this thesis, this chapter is devoted to a discussion of the physicochemical features of mucus with special attention to mucin, the primary structural component of mucus that is largely responsible for its bulk physical properties and biochemical properties. We begin this chapter by discussing the biochemistry of mucus and its biological functions in the human body. Next, we discuss how mucin interacts with molecules, including viruses, and how this may influence particle transport in mucus layers. Finally, we end this chapter with a discussion on the role of mucins in infectious disease transmission and its applications as a model system for mucus in 'small' scale and 'large' scale experiments like those done in this thesis.

2.1 Mucus biochemistry

Mucus is a biological hydrogel that lubricates every wet epithelial surface of the body, including the respiratory tract, gastrointestinal tract (GI), and female reproductive tract. This lubricious characteristic is essential in protecting epithelia against mechanical damage from shear-induced forces involved in digestion, blinking, and exhalation [1–3]. Mucus serves as a dynamic physicochemical semipermeable barrier that permits the transport and exchange of select molecules (i.e., nutrients, water, gases, odorants, hormones) while trapping and immobilizing foreign and harmful substances (i.e., toxins, heavy metals, or biological substances such as pathogenic bacteria, viruses, or parasites) [4,5].

Native mucus is a biological hydrogel that is primarily water (95%) with the remaining 5% comprised of salts, lipids, and proteins [6]. The primary structural component of mucus that is responsible for its viscoelastic and gel-like properties is the glycoprotein mucin. Different mucosal surfaces throughout the body produce different types of mucins that are present at varying concentrations: 1%-5% in the GI [7], up to 2% in the airways [8], and at lower concentrations in salivary fluid (~0.3%) [9] and tear fluid (<0.02%) [10]. To date, 21 mucin-type glycoproteins that belong to the MUC gene family have been identified in humans (www.genenames.org); mucin can be divided into two subgroups: secreted and membrane-

bound [11]. Within secreted mucins, there exist gel-forming mucins (MUC2, MUC5AC, MUC5B, MUC6, MUC19) as well two nonpolymeric glycoproteins (MUC7 and MUC8) [12]. In the GI tract, MUC2 and MUC5AC are the most abundantly secreted mucins [7,12,13]. MUC5AC is not only the predominant mucin in gastric mucus [12], but also in tear fluid [10], respiratory tract fluid [14], and the cervicovaginal mucus [15]. MUC5B is also broadly expressed in the human body and is the major mucin found in the airways, female reproductive tract [14,15], and salivary glands [16]. Secreted mucin can span several microns long, whereas membrane-bound mucins are relatively short and only span hundreds of nanometers [17]. Individual subunits of secreted mucin polymerize via end-to-end disulfide bonds to form large mucin chains [18]. Mucins typically have molecular weights in the range of 0.5 to 40 MDa [18]; nearly 80% of the mucin mass is attributed to its heavy glycosylation while the remaining mass represents the protein backbone [6,19]. The protein backbone is composed of a variable number of tandem repeats (VNTR) rich in proline, threonine, and/or serine (PTS domains), along with cysteine-rich regions spread between PTS domains and at the amino and carboxy terminus [11]. PTS sequences along the protein backbone are sites of dense O-linked glycosylation, where glycans are anchored onto the serine and threonine residues and structurally resemble “bottle-brushes” [6,19]. Various other carbohydrates can be glycosylated to mucin including fucose, mannose, sulfate, and sialic acid [19]. The high sialic acid and sulfate content of mucins confers an overall negative charge to the molecule which results in intramolecular repulsion under aqueous conditions [20]. Although the different mucin types contain similar structures, variability in the PTS domains, sequence, and VNTRs give mucin different biochemical properties.

In aqueous solutions, mucin form polymeric networks maintained by chain entanglements, electrostatic repulsion between the negatively charge polysaccharide side chains, and covalent and noncovalent interactions [7,21]. Although noncovalent binding is relatively weaker than covalent binding, the cumulative effect of van der Waals, hydrophobic, ionic, hydrogen bonding, and other binding interactions can result in strong, long-lived mucin-mucin interactions [7,21]. Mucus’ physical structure, the strength of interactions within its network, and its bulk properties are regulated by variations in pH, ionic concentration, and modifications to mucus hydration via changes in mucin glycan density or identity [11]. As a result, different mucus layers possess different mechanical and biochemical properties depending on their location. For example, the highly acidic environments found in the GI tract are believed to promote phase separation which increases bulk viscoelasticity. This increased mucus viscoelasticity results in stiffer mucus gel lining in the stomach, serving as a protective barrier against acidic gastric juices [22]. Although increased viscoelasticity may have a

protective effect in certain areas, there can be negative effects in other areas like the respiratory tract, where severely thickened mucus reduces effective mucociliary clearance. Typically, lung mucus, nasal mucus, and saliva have a neutral pH [17].

2.2 Mucin networks as within-host semi-permeable barriers

Humans continuously secrete mucus, amounting to approximately 10 liters per day [23]. Mucus layers are subsequently shed, discarded, or digested and renewed by the continued mucus secretion of underlying epithelial cells. The lifetime or “clearance time” of mucus is short, often observed between minutes and hours, with the fastest turnover typically observed in the thinnest mucus layers (i.e., nasal tract) [17]. Thus, biological or synthetic particles must penetrate mucus faster than the natural turnover to reach their target sites. Their movement through mucus relies on common principles that govern the filtration of molecules in hydrogels. Broadly, the transport of a solute through a gel is controlled by two methods: size filtering and interaction filtering. In the following three sections, we discuss these two methods in more detail and additionally expand on how these concepts are relevant for virus transport.

2.2.1 Size filtering

Entangled and cross-linked mucin form a microscopic mesh capable of limiting or permitting the passage of select molecules. The distance between adjacent links or junctions in the network corresponds to the pore size or mesh size; assuming inert particles, particles smaller than the mesh size diffuse through pores, while particles on the order of the mesh size and bigger are hindered or immobilized (illustrated in **Figure 2.1**). The pore size of mucin gels spans tens of nanometers to thousands of nanometers (~20-1800 nm) depending on the location in the body [7]. Disease states associated with mucosal dysfunction can also alter pore size. For instance, the typical pore size for respiratory mucus is approximately 500 nm; however, the pore size decreases to approximately 150 nm in patients with cystic fibrosis [24]. In the GI tract, the inner colonic mucus layer is believed to form a barrier separating bacteria form colonic epithelium. However, in inflammatory diseases such as ulcerative colitis, bacteria can have enhanced penetration which is attributed to a compromised mucus structure [25].

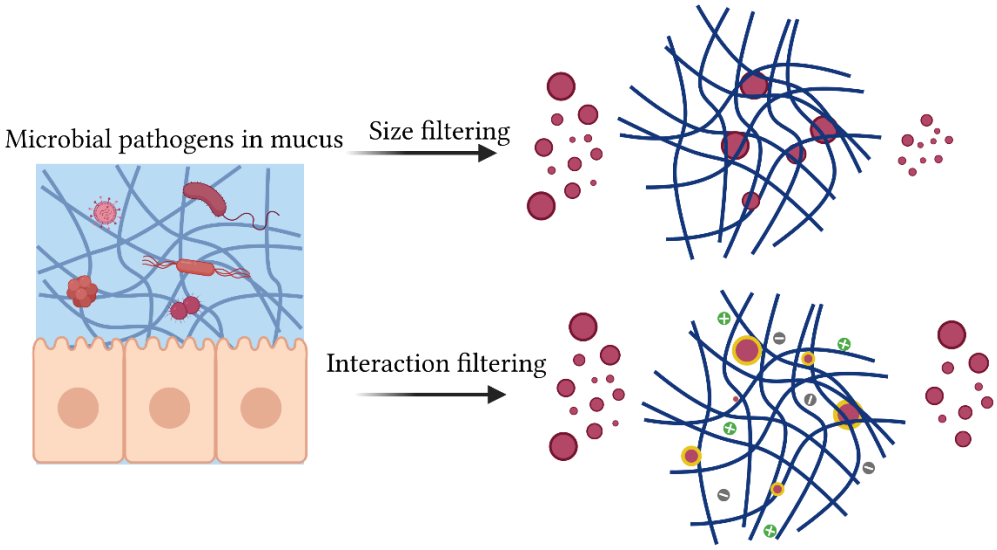

Figure 2.1 Illustration of filtering mechanisms regulating mucus permeability: size filtering and interaction filtering. Size filtering allows molecules and particles smaller than the mucin network mesh size to cross, while larger molecules are rejected. Interaction filtering allows particles to be selected according to their surface properties and binding interactions with the mucin network. Some particles interact strongly with mucus and trapped (particles with thick-yellow-orange edges), whereas other particles exhibit only weak interactions and pass through the network (particles with thin dark edges).

On a macroscopic level, the mucus network increases the bulk viscosity of mucus gels by nearly 1,000 to 10,000 times greater than the viscosity of water [17]. Assuming bulk viscosity, classical application of the Stokes-Einstein equation would predict particle displacements much smaller than the typical thickness of mucus layers over timescales relevant for mucus clearance of viruses or hydrophilic macromolecules. However, several studies have observed a decrease in particle mobility through mucus with increasing particle size that is inconsistent with the theoretical prediction of the Stokes-Einstein relationship [26–29]. This indicated that particles smaller than the mesh size diffuse at a rate corresponding to the viscosity of the aqueous solution contained within pores. Although larger macromolecules are predicted to be trapped and confined based on steric interactions, evidence has shown that certain macromolecules larger than the pore size are capable of rapidly diffusing through mucus [30,31] demonstrating that a combination of methods of filtration control mucus permeability.

2.2.3 Interaction filtering

In addition to filtration by size, particle transport through mucus can be influenced by mucin-particle interactions. Mucin-particle interactions allow for particle filtration on the basis of particle properties such as surface chemistry, binding affinity, and binding site density (illustrated in **Figure 2.1**). Some particles, even those smaller than the characteristic pore size, may interact frequently or strongly with mucus components and become constrained or completely immobile, while other particles can exhibit weak, low-frequency interactions, enabling particles to freely diffuse. Moreover, particles or certain mucus treatments can alter the pore size, enabling larger particles to penetrate through mucus. For example, the diffusion of nanoparticles [32] and influenza virus [33] in mucus treated with mucolytic agents was greater than that observed in untreated mucus. In contrast, in the presence of emulsifiers (i.e. carboxyl methylcellulose), researchers observed a lower mucus pore size and lower diffusion rates of *Escherichia coli* [34]. Similarly, modified nanoparticles coated with mucolytic proteases show enhance transport through mucus as a result of their ability to degrade mucin polymers [35]. In drug delivery applications, overcoming the mucus barrier and proper distribution of drug vehicles is a challenge that has been attempted with different types of drug carriers, including 'mucoadhesive' [36] and 'mucus-penetrating' particles [17].

Mucus can form adhesive interactions with particles via electrostatic interactions, Van der Waals forces, hydrophobic forces, hydrogen bonding, and chain entanglement [37]. The presence of carboxyl (-COOH) and sulfate groups ($-SO_4^{2-}$) on mucin allows penetration of similarly charged particles via electrostatic repulsions. On the other hand, oppositely charged particles form polyvalent adhesive interactions with mucin via electrostatic forces that restrains their motion. However, despite having a negative surface charge, some particles may still interact with mucin due to the formation of hydrophobic adhesive interactions with disulfide stabilized hydrophobic regions along mucin [17,23]. Although polar/hydrophilic particles can evade hydrophobic entrapment, interactions with mucin are possible through hydrogen bonding [38].

Apart from the particle's surface chemistry, the number of particle binding sites with an affinity for mucus can impact its degree of interaction with mucins. For instance, small, relatively hydrophobic molecules show enhanced diffusivity through mucus relative to larger, biochemically similar molecules because they form only a few low-affinity, short-lived bonds with mucin. In contrast, the negatively charged glycan domains on mucins are sites where small cationic molecules and polyvalent cations can attach strongly [39]. Although a higher positive

charge is associated with stronger binding between the particle and mucus, the overall surface charge is not an exact predictor for the strength of binding and resulting transport. This finding is supported by work demonstrating that the geometric arrangement of positive and negative charges for the equivalent overall surface charge can influence transport [40].

2.2.4 Within-host mucin/virus interactions

In a host, the mucus layer lining the respiratory tract serves as the “first line of defense” against inhaled pathogens [41]. Viruses are generally 20–200 nm in diameter, which allows them to penetrate the pores of mucin gels [23]. However, adhesive interactions with mucus may slow this diffusion depending on the surface properties of the virus [41]. Instead of secreting mucin-degrading enzymes as bacterial species do, viruses have evolved surface chemistries that favor minimal biochemical interactions with the components of mucus barriers [42,43]. Non-enveloped viruses, such as human papilloma virus and norovirus, are believed to be minimally adhesive to mucin due to the mixture of positive and negative surface charges that result in an overall neutral surface charge [44]. In addition to their net charge, non-enveloped viruses may not interact with mucin via hydrophobic interactions because they have few hydrophobic regions [45]; enveloped viruses, on the other hand, have hydrophobic viral envelopes.

Recent evidence suggests that viruses may more effectively spread and infect target cells as an aggregate of infectious units [46]. Variations in pH and salt concentration have been shown to produce viral aggregates in saliva [47]. However, the benefits of forming these larger virion aggregates in terms of greater infection potential can be expected to be offset by enhanced steric or adhesive interactions with the mucin network, illustrating a mechanism by which mucus may display anti-viral properties.

Early researchers determined that influenza A viruses (IAVs) have an affinity for mucus [48]. During transmission, the virus initially encounters respiratory tract mucus in the nasal cavity or oral cavity and must overcome this barrier to reach its target epithelial cells. Among other purified salivary proteins, MUC5B from human whole saliva has been show to inhibit IAVs at physiologically relevant concentrations [49]. It has been long hypothesized that mucus may act as a barrier against IAV infection by imitating cell surface receptors [50]. Mucins are rich in terminal sialic acids (Sias), which are thought to act as “decoy receptors” that can trap IAVs in the mucus layer and then clear viruses by the natural turnover of mucus [50–52]. In the human respiratory tract, the distribution of terminal Sias alpha2,6 and alpha2,3, which are also

expressed in the porcine respiratory tract [41], varies along the respiratory tract and with aging [53]. Specific sialic acid types are more abundant in certain hosts and in particular physiological locations. For example, alpha2,3-linked Sias are more abundant in the GI tract of avian hosts, while alpha2,6-linked Sias are more abundant in the human upper respiratory tract [41,53]. Viruses also have a Sias binding preference: human influenza viruses preferentially bind alpha2,6-linked Sias, while avian and equine influenza viruses preferentially bind to alpha2,3-linked Sias [54,55]. Thus, host restriction (i.e., virus receptor specificity vs. host receptor availability) and susceptibility may be significantly influenced by factors such as structural variations in sialic acid linkages, spatial distribution of linkages in hosts, and Sias binding preferences [56]. Other viruses are also reported to bind to Sias including OC43 [57], SARS-CoV, SARS-CoV-2 [58], and MERS [59]. Viruses express a range of viral surface proteins that may confer an ability to diffuse through mucus unhindered.

Two surface proteins of IAVs, hemagglutinin (HA) and neuraminidase (NA), have specialized functions that initiate infection. HA binds to sialic acid receptors on the surface of cells and induces membrane fusion [60]. NA is responsible for releasing the virus into cells by cleaving the receptors [61]. While mucus is protective against IAVs, NA potentially circumvents entrapment of the virus by cleaving mucin's "decoy receptor" and enabling the virus to transport across the mucus barrier to infect the epithelium. In an *in vitro* investigation in which influenza viruses were added to a layer of porcine respiratory mucus [52], the degree of penetration of the viruses in the mucus layer was shown to be enhanced by the addition of NA, while the addition of oseltamivir, an NA inhibitor, demonstrated reduced penetration of the viruses [52]. Similarly, in another *in vitro* study with swine- and human-origin viruses, purified sialylated human salivary mucins competitively inhibited NA cleavage in a dose-dependent manner, whereas porcine submaxillary mucin (PSM) could not prevent infection of underlying Madin–Darby canine kidney cells [50]. Although PSM also contains sialic acids, the presentation of sialic acid differs between PSM and human salivary mucin. Human influenza viruses bind alpha2,6-linked N-glycolylneuraminic acid (Neu5Ac), while PSM and many other animal models express N-glycolylneuraminic acid (Neu5Gc) [62]. This aspect is especially important to note in the selection of animal mucus models because the studied virus may not interact with receptors encountered in the native mucus environment.

2.3 Role of mucus in infectious disease transmission

A vast array of research has demonstrated unique characteristics of mucins that can be

potentially advantageous or deleterious to pathogens by promoting binding and sequestration within hosts. Yet, many questions remain in our understanding of the mechanistic details by which mucus, particularly mucins, interact with pathogens and modulates disease progression and transmission both within and external to hosts. Here we present the findings of existing studies that studied respiratory aerosols and the viability of viruses in mucus droplets.

When a virus is emitted, whether through coughing, sneezing, talking, or breathing, it is enveloped in respiratory tract fluid, and its successful onward transmission depends on it remaining viable until its transfer to a new host. Real-time reverse transcription PCR detection results for throat, nasal, saliva, and sputum specimens from individuals with respiratory infections (e.g., influenza and SARS-CoV-2) have shown that exhalation emissions originating from different regions of the respiratory tract can exhibit a range of viral loads. Air samples in areas with nearby infected individuals not only contain viral RNA but also live, culturable viruses, supporting the route of aerosol transmission. Respiratory droplets traveling in the air will be entrained and advected in ambient air flows or the cloud of moist buoyant air emitted by the individual [63,64]. Larger droplets may settle quickly to the ground and contribute to infection via fomites, whereas smaller aerosolized droplets may remain suspended in the air [13, 115]. In general, the presence of polymers shifts the size distributions of droplets generated when solutions are sprayed, as occurs during sneezing and coughing [65–67]. Under different ambient temperature and humidity conditions, droplets will undergo different degrees of evaporation, which induce a variety of physicochemical transformations to the droplet determining the duration of pathogen viability.

Researchers have extensively studied the effect of external climate factors or ambient conditions, such as temperature and humidity (particularly relative humidity [RH]), on virus viability [68–74]. Among two early studies on this subject, only one found increased virus viability at lower temperatures [69], but both concluded varied effects of RH for the types of viruses tested [68,69]. More recent studies have found IAV viability in droplets to be highest at low RH [72], or highest at low and high RH and lowest in intermediate RH ranges [75]. The latter finding, including decreased viability with increasing temperature, was also observed in work combining experimental data for SARS-CoV-2 and other human coronaviruses [71]. The interplay among ionic strength, pH, and RH in the droplet complicates the identification of physical mechanisms for pathogen inactivation and survival. As the droplet evaporates and shrinks, the concentrations of salts, proteins, and other components increase by nearly an

order of magnitude due to water loss by evaporation [76], which can alter the pH of the droplet environment [74]. Consequently, evolving concentrations induce conformational changes to mucin and structural changes to viruses, and alter evaporation behavior (e.g., droplet lifetime, droplet morphology, and final residue or nucleus size).

The effect of the presence of proteins, particularly mucins, on the viability of viruses in droplets remains unresolved. Early work found that the addition of bovine serum albumin to Langat virus droplets increased survival across a range of RH values [77]. A more recent study showed that the presence of bovine serum albumin protected both bacteriophage MS2, a non-enveloped virus, and bacteriophage φ6, an enveloped virus, from inactivation in droplets [70]. At intermediate RHs, the viability of IAV decreased in saline solutions, yet increased dramatically in the presence of salt and mucus [74]. However, protein-rich media alone with salt did not significantly alter the viability, highlighting a potentially unique effect of mucins in mitigating adverse effects of elevated salt concentrations on virus survival [74]. Salts in solution, such as sodium chloride, challenge the survival of enveloped viruses such as φ6, influenza, or coronaviruses, due to the osmotic pressure difference across the lipid membrane. Without the ability to transport water across the virus lipid membrane due to a lack of water regulatory channels, enveloped viruses are vulnerable to osmotic damage [78]. A previous study evidenced enhanced inactivation of viruses by salts at specific pH levels [79], leading to alterations in membrane structure; however, the exact mechanism has not been identified [74]. While salts appear to be toxic to enveloped viruses, salts improve the viability of non-enveloped viruses; they are reportedly more resistant to inactivation and contain critical proteins responsible for cell attachment on their capsids. Both non-enveloped and enveloped viruses are generally more susceptible to inactivation in acidic and basic solutions than in pH-neutral solutions [80].

In recent work, the remains or dried residue of water droplets with varying concentrations of salt, mucin, and surfactant showed distinguishing characteristics between saline droplets and salt–mucin droplets evaporating on superhydrophobic substrates emulating the drying of aerosol droplets [78]. In the former droplets, a single crystal shape remained; meanwhile, in the latter, a “bone-like” structure remained, indicating a disruption in crystallization by the presence of the protein (shown in **Figure 2.2**) [78]. Similarly, on more wetting surfaces, modified crystallization patterns arose in the presence of mucins (shown in **Figure 2.2**) [81]. The evaporation-induced solution concentration gradient near the droplet surface not only rearranges the deposition of solutes but also slows the drying or evaporation process.

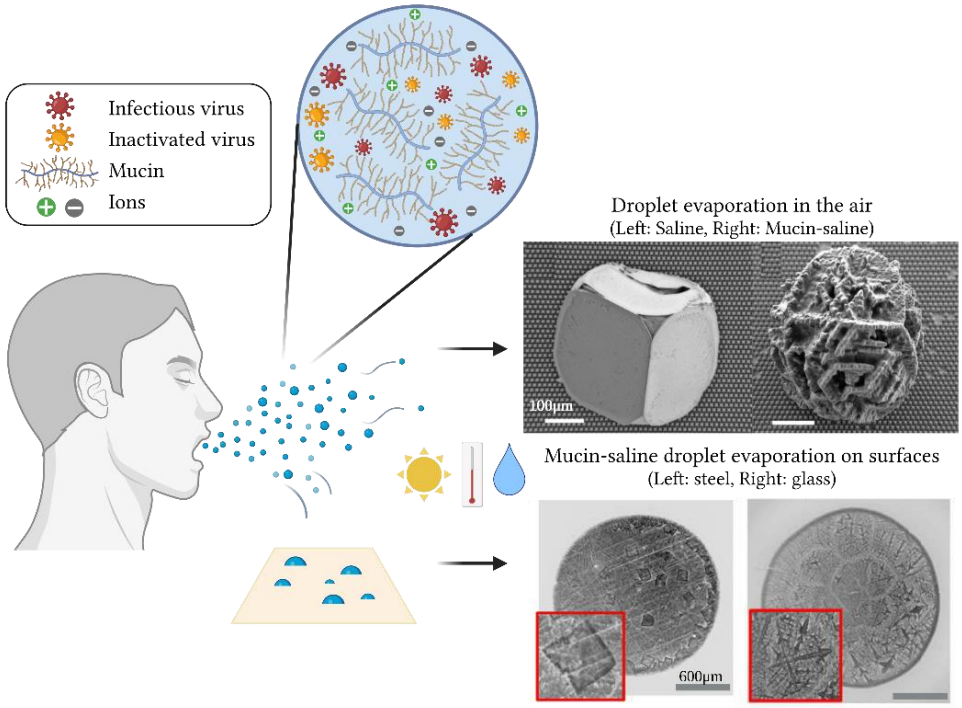

Figure 2.2 The surrounding environment (sunlight, temperature, moisture) and composition of respiratory droplets affect their evaporation behavior, as well as the ionic concentration and pH of the droplet environment over time. The evaporation of droplets on superhydrophobic surfaces to simulate evaporation in the air of saline and mucin – saline results in distinct final residues upon drying (image reproduced with permission from [78] in the top right panel). Similarly, evaporation on surface results in flat residues with distinctive morphologies depending on the surface properties and droplet contents (image reproduced from [81] in the bottom right panel). Altogether, the temporal evolution of droplet composition and resulting deposition patterns modulate the infectivity and viability of pathogens encapsulated in mucosal droplets.

Apart from studying the infectivity and survivability of viruses in droplets, researchers have also studied the droplet size distribution of laboratory generated aerosols and aerosols from human subjects. Studies that used healthy human subjects to record exhalations (e.g., breathing, talking, coughing, or sneezing) typically included small sample groups and used varying techniques to measure droplet size [82–86]. While native mucus preserves the structure and composition of mucins, the high degree of variability between individuals and even within an individual, and mucus' heterogeneity can make it difficult to interpret results from experiments; there may be important differences in the "quality" of the exhaled aerosol (e.g., droplet size and

spatial dispersion) between individuals [87]. Variability in mucus and the quality of the aerosol can be attributed to several factors including differences in fluid material properties, origin of expelled mucus (e.g., sputum versus mucosalivary fluid), respiratory physiology (e.g., lung volume), and environmental conditions (e.g., temperature, humidity). Consequently, it is challenging to understand how different components of mucus (e.g., mucin concentration, salt type/concentration, protein, presence of pathogens, etc.) contribute to dispersion and droplet size. An understanding of how different components of mucus affect droplet size is important because the particle deposition in the respiratory system of a nearby host is size-dependent; small virus-containing droplets are more likely to deposit deeper into the respiratory tract while larger virus-containing droplets are more likely to land in the upper airways [88]. The penetration of droplets in the respiratory tract may affect the severity of infection; compared with upper respiratory infections, lower respiratory tract infections are associated with increased severity, morbidity, and fatality [89]. In addition, the droplet size distribution will determine the total duration infectious particles remain suspended in the air, their distance and spread in environment external to the host. This can impact the number of susceptible individuals that may inhale droplets or come in contact with droplets on surfaces. Importantly, the risk of transmission is associated with viral load [90] which has been shown to depend on droplet size and virus type [91–94].

Although some studies do incorporate the effect of mucins, a majority rely on commercial porcine gastric mucins (PGM) to model mucosalivary droplets. Commercial, industrially purified PGM does not form gels and exhibits dramatically lower anti-viral and anti-bacterial activity [95,96], as well as inferior lubricity [97]. At the other extreme, some computational models and experiments on the transport and viability of airborne viruses assume that exhaled fluid can be modeled as water or ion/water solution. However, this oversimplification ignores the complex composition and interactions that occur between respiratory tract fluids and pathogens. In fact, assuming that pathogen-laden droplets emitted during exhalation events are Newtonian liquids would result in an underestimation of mean droplet sizes as a result of omission of viscoelasticity [67,98,99]. Viscoelastic effects contribute to strong extensional flows in aerosolized fluid threads that break up to form larger droplets [67,98].

2.4 Mucin gels as model system for native mucus

Although the *in vivo* composition and structure of mucus are preserved in native harvested mucus, the heterogeneity of mucus and the extensive variation in composition between individuals, and even within an individual, can make it difficult to interpret and compare experiments with native mucus [11]. The model system chosen to study pathogen transport through mucus and transmission external to hosts are critical. As such, gels reconstituted from purified mucin molecules are an accepted experimental model for mucus that mimics selected properties of mucus and is relatively more homogenous than native samples because of the removal of other mucus components. Reconstituted mucin gels not only have a well-defined composition, but produce well-controlled, reproducible environments for assessing the influence of select conditions. In the following sections we discuss mucin harvesting and purification methods and the use of mucin in experiments.

2.4.1 Mucus harvesting and mucin purification

Mucins are commonly extracted from various animal sources including pigs and cows which have served as the primary sources of mucus due to their wide availability and the large amounts of mucus they contain relative to other sources. Researchers can isolate mucins from mucosal tissues by either extracting mucus layers [100] or homogenizing whole tissues [101]. Depending on the source, researchers apply different techniques to animal tissues, such as mucus scraping, to extract mucin-containing material [102]. In this thesis, porcine-derived mucins were purified from fresh pig scrapings (MUC5AC) or fresh pig intestinal scrapings (MUC2) following previously described methods in [103,104].

Purification is achieved by making use of mucin's unique physical and chemical characteristics, including their solubility, large size, and strong negative charge. Importantly, mucins are not completely resistant to degradation: the glycosylated fractions of mucins are relatively better protected against proteolytic degradation, while the unglycosylated portions are more vulnerable. Hence, researchers must take care both during mucin purification and when working with native mucus samples to mitigate mucin degradation or they must account for such processes in any physicochemical readouts of mucin gel properties [105].

Human mucin sources [102] may be more difficult to access and less abundant than animal tissue sources. Because of the limited availability of human mucins, research has relied heavily on commercial sources of mucins, specifically the porcine gastric mucin MUC5AC and the bovine submaxillary mucin MUC5B, which are the most relevant mucin models to humans.

The two most widely used commercial purified mucins come in powdered form and are produced by Sigma Aldrich: “mucin from porcine stomach, Type II” and “mucin from porcine stomach, Type III” [106]. Unfortunately, the harsh treatment processes during commercial mucin purification have been associated with altered mucin structures [11], causing changes to the physicochemical properties of gels reconstituted from these materials [96,107]. In fact, industrially purified mucins have been found to have a lower capacity for forming gels [106,108], and the resulting gels are less lubricious [106,109] than native mucin purified in-lab.

2.4.2 Multi-scale experiments with mucin gels

Although mucin’s sugar chains provide anti-proteolytic properties, mucins are not completely resistant to degradation by bacterial species or other changes to their structure by environmental factors such as ambient air, temperature, or light. Bacterial enzymes can degrade mucins through proteolytic or polysaccharide cleavage, which enhances bacterial permeability through mucus and accommodates microbial growth [110]. In addition, to enzymatic degradation, native mucus is also sensitive to mechanical manipulation such as freeze-thaw cycles [111]. Because of this, synthetic polymers such as methylcellulose have been used to simulate the mechanical properties of mucus, however biochemically, methylcellulose does not interact with microbes or other molecules in the same way that native mucus does [103].

A growing number of studies have used gels reconstituted from lab-purified mucins, which retain physicochemical properties relative to native mucus, enabling researchers to interrogate structure–function relationships of mucin glycoproteins [22,103,112–114]. Ultimately, the choice of an appropriate mucus model system may be highly dependent on the length scale relevant to the physiological process being studied; the ability to represent all mucus properties in one experimental model, including its mechanical, biological, and chemical properties, is experimentally challenging [115]. For example, modeling large-scale phenomena such as mucus clearance, may require that the mucus model reflects the macrorheological properties of native mucus to study droplet formation and dispersion. At the same time, in the modeling of small-scale processes, such as the transport of biological substances through the mucus barrier, a mucus model system that exhibits native mucus’ “sticky” character and related biochemical properties may be more appropriate. However, this may be an oversimplified view since macroscale properties of mucus may be reliant on a series of nanoscale or microscale interactions (e.g., mucin-particle interactions) that occur within the mucus structure; in other

words, the mucin-specific biochemistry may also be an important characteristic to consider when modeling large-scale physiological processes.

2.5 References

[1] P. Argüeso, I.K. Gipson, Epithelial mucins of the ocular surface: Structure, biosynthesis and function, Exp. Eye Res. 73 (2001) 281–289. https://doi.org/10.1006/exer.2001.1045.

[2] S. Girod, J.M. Zahm, C. Plotkowski, G. Beck, E. Puchelle, Role of the physicochemical properties of mucus in the protection of the respiratory epithelium, Eur. Respir. J. 5 (1992) 477–487.

[3] C.T. Nordgård, K.I. Draget, Dynamic responses in small intestinal mucus: Relevance for the maintenance of an intact barrier, Eur. J. Pharm. Biopharm. 95 (2015) 144–150. https://doi.org/10.1016/j.ejpb.2015.01.024.

[4] A. Allen, R.H. Pain, T.R. Robson, Model for the structure of the gastric mucous gel, Nature. 264 (1976) 88–89. https://doi.org/10.1038/264088a0.

[5] S.K. Linden, P. Sutton, N.G. Karlsson, V. Korolik, M.A. McGuckin, Mucins in the mucosal barrier to infection, Mucosal Immunol. 1 (2008) 183–197. https://doi.org/10.1038/mi.2008.5.

[6] R. Bansil, B.S. Turner, The biology of mucus: Composition, synthesis and organization, Adv. Drug Deliv. Rev. 124 (2018) 3–15. https://doi.org/10.1016/j.addr.2017.09.023.

[7] J. Leal, H.D.C. Smyth, D. Ghosh, Physicochemical properties of mucus and their impact on transmucosal drug delivery, Int. J. Pharm. 532 (2017) 555–572. https://doi.org/10.1016/j.ijpharm.2017.09.018.

[8] D.F. Rogers, Airway Mucus Hypersecretion in Asthma and COPD: Not the Same?, in: Airw. Dis., 2009: pp. 211–223. https://doi.org/10.1016/B978-0-12-374001-4.00017-1.

[9] A. Sarkar, F. Xu, S. Lee, Human saliva and model saliva at bulk to adsorbed phases – similarities and differences, Adv. Colloid Interface Sci. 273 (2019) 102034. https://doi.org/10.1016/j.cis.2019.102034.

[10] H. Zhao, J.E. Jumblatt, T.O. Wood, M.M. Jumblatt, Quantification of MUC5AC protein in human tears, Cornea. 20 (2001) 873–877. https://doi.org/10.1097/00003226-200111000-00019.

[11] C.E. Wagner, K.M. Wheeler, K. Ribbeck, Mucins and Their Role in Shaping the Functions of Mucus Barriers, Annu. Rev. Cell Dev. Biol. 34 (2018) 189–215. https://doi.org/10.1146/annurev-cellbio-100617-0628181.

[12] D.J. Thornton, K. Rousseau, M.A. McGuckin, Structure and function of the polymeric mucins in airways mucus, Annu. Rev. Physiol. 70 (2008) 459–486. https://doi.org/10.1146/annurev.physiol.70.113006.100702.

[13] V. Strugula, A. Allen, P.W. Dettmar, J.P. Pearson, Colonic mucin: methods of mesauring mucus thickness, Proc. Nutr. Soc. 62 (2003) 237–243.

[14] J.R. Davies, N. Svitacheva, L. Lannefors, R. Kornfa, Identification of MUC5B, MUC5AC, and small amounts of MUC2 mucin in cystic fibrosis airway secretions, Society. 330 (1999) 321–330.

[15] G. Lacroix, V. Gouyer, F. Gottrand, J.L. Desseyn, The cervicovaginal mucus barrier, Int. J. Mol. Sci. 21 (2020) 1–23. https://doi.org/10.3390/ijms21218266.

[16] L.A. Bobek, H. Tsai, A.R. Biesbrock, M.J. Levine, Molecular cloning, sequence, and specificity of expression of the gene encoding the low molecular weight human salivary mucin (MUC7), J. Biol. Chem. 268 (1993) 20563–20569. https://doi.org/10.1016/s0021-9258(20)80762-5.

[17] S.K. Lai, Y.Y. Wang, J. Hanes, Mucus-penetrating nanoparticles for drug and gene delivery to mucosal tissues, Adv. Drug Deliv. Rev. 61 (2009) 158–171. https://doi.org/10.1016/j.addr.2008.11.002.

[18] J.K. Sheehan, I. Carlstedt, Hydrodynamic properties of human cervical-mucus glycoproteins in 6M-guanidinium chloride, Biochem. J. 217 (1984) 93–101. https://doi.org/10.1042/bj2170093.

[19] R. Bansil, B.S. Turner, Mucin structure, aggregation, physiological functions and biomedical applications, Curr. Opin. Colloid Interface Sci. 11 (2006) 164–170. https://doi.org/10.1016/j.cocis.2005.11.001.

[20] R. Shogren, T.A. Gerken, N. Jentoft, Role of Glycosylation on the Conformation and Chain Dimensions of O-Linked Glycoproteins: Light-Scattering Studies of Ovine Submaxillary Mucin, Biochemistry. 28 (1989) 5525–5536. https://doi.org/10.1021/bi00439a029.

[21] O. Lieleg, K. Ribbeck, Biological hydrogels as selective diffusion barriers, Trends Cell Biol. 21 (2011) 543–551. https://doi.org/10.1016/j.tcb.2011.06.002.

[22] J.P. Celli, B.S. Turner, N.H. Afdhal, R.H. Ewoldt, G.H. McKinley, R. Bansil, S. Erramilli, Rheology of gastric mucin exhibits a pH-dependent sol-gel transition, Biomacromolecules. 8 (2007) 1580–1586. https://doi.org/10.1021/bm0609691.

[23] R.A. Cone, Mucus, in: Mucosal Immunol., 2005: pp. 49–72.

[24] J. V. Fahy, B.F. Dickey, Airway Mucus Function and Dysfunction, N. Engl. J. Med. 363 (2010) 2233–2247. https://doi.org/10.1056/nejmra0910061.

[25] M.E.V. Johansson, J.K. Gustafsson, J. Holmen-Larsson, K.S. Jabbar, L. Xia, H. Xu, F.K. Ghishan, F.A. Carvalho, A.T. Gewirtz, H. Sjovall, G.C. Hansson, Bacteria penetrate the normally impenetrable inner colon mucus layer in both murine colitis models and patients with ulcerative colitis, Gut. 63 (2014) 281–291. https://doi.org/10.1136/gutjnl-2012-303207.

[26] M. Dawson, D. Wirtz, J. Hanes, Enhanced Viscoelasticity of Human Cystic Fibrotic Sputum Correlates with Increasing Microheterogeneity in Particle Transport, J. Biol. Chem. 278 (2003) 50393–50401. https://doi.org/10.1074/jbc.M309026200.

[27] L. Kaler, E. Iverson, S. Bader, D. Song, M.A. Scull, G.A. Duncan, B. Program, G. Duncan, Influenza A virus diffusion through mucus gel networks, BioRxiv. (2020) 2020.08.14.251132. https://doi.org/10.1101/2020.08.14.251132.

[28] X. Murgia, P. Pawelzyk, U.F. Schaefer, C. Wagner, N. Willenbacher, C.M. Lehr, Size-Limited Penetration of Nanoparticles into Porcine Respiratory Mucus after Aerosol Deposition, Biomacromolecules. 17 (2016) 1536–1542. https://doi.org/10.1021/acs.biomac.6b00164.

[29] H.M. Yildiz, C.A. McKelvey, P.J. Marsac, R.L. Carrier, Size selectivity of intestinal mucus to diffusing particulates is dependent on surface chemistry and exposure to lipids, J. Drug Target. 23 (2015) 768–774. https://doi.org/10.3109/1061186X.2015.1086359.

[30] S.S. Olmsted, J.L. Padgett, A.I. Yudin, K.J. Whaley, T.R. Moench, R.A. Cone, Diffusion of macromolecules and virus-like particles in human cervical mucus, Biophys. J. 81 (2001) 1930–1937. https://doi.org/10.1016/S0006-3495(01)75844-4.

[31] S.K. Lai, D.E. O'Hanlon, S. Harrold, S.T. Man, Y.Y. Wang, R. Cone, J. Hanes, Rapid transport of large polymeric nanoparticles in fresh undiluted human mucus, Proc. Natl. Acad. Sci. U. S. A. 104 (2007) 1482–1487. https://doi.org/10.1073/pnas.0608611104.

[32] J.S. Suk, S.K. Lai, N.J. Boylan, M.R. Dawson, M.P. Boyle, J. Hanes, Rapid transport of muco-inert nanoparticles in cystic fibrosis sputum treated with N-acetyl cysteine, Nanomedicine. 6 (2011) 365–375. https://doi.org/10.2217/nnm.10.123.

[33] L. Kaler, E. Iverson, S. Bader, D. Song, M.A. Scull, G.A. Duncan, Influenza A virus diffusion through mucus gel networks, Commun. Biol. 5 (2022) 1–9. https://doi.org/10.1038/s42003-022-03204-3.

[34] J.Y. Lock, T.L. Carlson, C.M. Wang, A. Chen, R.L. Carrier, Acute Exposure to Commonly Ingested Emulsifiers Alters Intestinal Mucus Structure and Transport Properties, Sci. Rep. 8 (2018) 1–14. https://doi.org/10.1038/s41598-018-27957-2.

[35] I. Pereira De Sousa, B. Cattoz, M.D. Wilcox, P.C. Griffiths, R. Dalgliesh, S. Rogers, A. Bernkop-Schnürch, Nanoparticles decorated with proteolytic enzymes, a promising strategy to overcome the mucus barrier, Eur. J. Pharm. Biopharm. 97 (2015) 257–264. https://doi.org/10.1016/j.ejpb.2015.01.008.

[36] H. Takeuchi, H. Yamamoto, Y. Kawashima, Mucoadhesive nanoparticulate systems for peptide drug delivery, Adv. Drug Deliv. Rev. 47 (2001) 39–54. https://doi.org/10.1016/S0169-409X(00)00120-4.

[37] P. Prasher, M. Sharma, S.K. Singh, M. Gulati, N.K. Jha, P.K. Gupta, G. Gupta, D.K. Chellappan, F. Zacconi, T. de Jesus Andreoli Pinto, Y. Chan, G. Liu, K.R. Paudel, P.M. Hansbro, B.G.G. Oliver, K. Dua, Targetin mucus barrier in repsiratory disease by chemically modified advanced delivery systems, Chem. Biol. Interact. 365 (2022).

[38] B.S. Lele, A.S. Hoffman, Mucoadhesive drug carriers based on complexes of poly(acrylic acid) and PEGylated drugs having hydrolysable PEG-anhydride-drug linkages, J. Control. Release. 69 (2000) 237–248. https://doi.org/10.1016/S0168-3659(00)00303-5.

[39] J. Witten, T. Samad, K. Ribbeck, Selective permeability of mucus barriers, Curr. Opin. Biotechnol. 52 (2018) 124–133. https://doi.org/10.1016/j.copbio.2018.03.010.

[40] L.D. Li, T. Crouzier, A. Sarkar, L. Dunphy, J. Han, K. Ribbeck, Spatial configuration and composition of charge modulates transport into a mucin hydrogel barrier, Biophys. J. 105 (2013) 1357–1365. https://doi.org/10.1016/j.bpj.2013.07.050.

[41] M. Zanin, P. Baviskar, R. Webster, R. Webby, The Interaction between Respiratory Pathogens and Mucus, Cell Host Microbe. 19 (2016) 159–168. https://doi.org/10.1016/j.chom.2016.01.001.

[42] A. Heidari, I. Righetto, F. Filippini, Electrostatic Variation of Haemagglutinin as a Hallmark of the Evolution of Avian Influenza Viruses, Sci. Rep. 8 (2018) 1–8. https://doi.org/10.1038/s41598-018-20225-3.

[43] E. Joonaki, A. Hassanpouryouzband, C.L. Heldt, O. Areo, Surface Chemistry Can Unlock Drivers of Surface Stability of SARS-CoV-2 in a Variety of Environmental Conditions, Chem. 6 (2020) 2135–2146. https://doi.org/10.1016/j.chempr.2020.08.001.

[44] J. Witten, K. Ribbeck, The particle in the spider's web: Transport through biological hydrogels, Nanoscale. 9 (2017) 8080–8095. https://doi.org/10.1039/c6nr09736g.

[45] T.L. Carlson, J.Y. Lock, R.L. Carrier, Engineering the Mucus Barrier, Annu. Rev. Biomed. Eng. 20 (2018) 197–220. https://doi.org/10.1146/annurev-bioeng-062117-121156.

[46] A. Leeks, R. Sanjuán, S.A. West, The evolution of collective infectious units in viruses, Virus Res. 265 (2019) 94–101. https://doi.org/10.1016/j.virusres.2019.03.013.

[47] V. Anschau, R. Sanjuán, Fibrinogen gamma chain promotes aggregation of vesicular stomatitis virus in saliva, Viruses. 12 (2020). https://doi.org/10.3390/v12030282.

[48] F.M. Burnet, Mucoproteins in Relation to Virus Action, Physiol. Rev. 31 (1951).

[49] M.R. White, E.J. Helmerhorst, A. Ligtenberg, M. Karpel, T. Tecle, W.L. Siqueira, F.G. Oppenheim, K.L. Hartshorn, Multiple components contribute to ability of saliva to inhibit influenza viruses, Oral Microbiol. Immunol. 24 (2009) 18–24. https://doi.org/10.1111/j.1399-302X.2008.00468.x.

[50] M. Cohen, R. Schooley, M. Cohen, X. Zhang, H.P. Senaati, H. Chen, N.M. Varki, R.T. Schooley, Influenza A penetrates host mucus by cleaving sialic acids with neuraminidase Influenza A penetrates host mucus by cleaving sialic acids with neuraminidase, Virol. J. 10 (2013) 1. Virology Journal.

[51] R.A. Cone, Barrier properties of mucus, Adv. Drug Deliv. Rev. 61 (2009) 75–85. https://doi.org/10.1016/j.addr.2008.09.008.

[52] X. Yang, L. Steukers, K. Forier, R. Xiong, K. Braeckmans, K. Van Reeth, H. Nauwynck, A beneficiary role for neuraminidase in influenza virus penetration through the respiratory mucus, PLoS One. 9 (2014) e110026. https://doi.org/10.1371/journal.pone.0110026.

[53] J.M. Nicholls, M.C.W. Chan, W.Y. Chan, H.K. Wong, C.Y. Cheung, D.L.W. Kwong, M.P. Wong, W.H. Chui, L.L.M. Poon, S.W. Tsao, Y. Guan, J.S.M. Peiris, Tropism of avian influenza A (H5N1) in the upper and lower respiratory tract, Nat. Med. 13 (2007) 147–149. https://doi.org/10.1038/nm1529.

[54] Y. Suzuki, T. Ito, T. Suzuki, R.E. Holland, T.M. Chambers, M. Kiso, H. Ishida, Y. Kawaoka, Sialic Acid Species as a Determinant of the Host Range of Influenza A Viruses, J. Virol. 74 (2000) 11825–11831. https://doi.org/10.1128/jvi.74.24.11825-11831.2000.

[55] L. Sánchez-Felipe, E. Villar, I. Muñoz-Barroso, α;2-3-And α;2-6-N-linked sialic acids allow efficient interaction of Newcastle Disease Virus with target cells, Glycoconj. J. 29 (2012) 539–549. https://doi.org/10.1007/s10719-012-9431-0.

[56] M. Matrosovich, G. Herrler, H.D. Klenk, Sialic Acid Receptors of Viruses, Top Curr Chem. 367 (2015) 1–28. https://doi.org/10.1007/128.

[57] C.L. Wardzala, A.M. Wood, D.M. Belnap, J.R. Kramer, Mucins Inhibit Coronavirus Infection in a Glycan-Dependent Manner, ACS Cent. Sci. 8 (2022) 351–360. https://doi.org/10.1021/acscentsci.1c01369.

[58] L. Bò, M. Miotto, L. Di Rienzo, E. Milanetti, G. Ruocco, Exploring the Association Between Sialic Acid and SARS-CoV-2 Spike Protein Through a Molecular Dynamics-Based Approach, Front. Med. Technol. 2 (2021) 1–10. https://doi.org/10.3389/fmedt.2020.614652.

[59] W. Li, R.J.G. Hulswit, I. Widjaja, V.S. Raj, R. McBride, W. Peng, W. Widagdo, M.A. Tortorici, B. Van Dieren, Y. Lang, J.W.M. Van Lent, J.C. Paulson, C.A.M. De Haan, R.J. De Groot, F.J.M. Van Kuppeveld, B.L. Haagmans, B.J. Bosch, Identification of sialic acid-binding function for the Middle East respiratory syndrome coronavirus spike glycoprotein, Proc. Natl. Acad. Sci. U. S. A. 114 (2017) E8508–E8517. https://doi.org/10.1073/pnas.1712592114.

[60] I. Ramos, A. Fernandez-Sesma, Cell receptors for influenza A viruses and the innate immune response, Front. Microbiol. 3 (2012) 1–6. https://doi.org/10.3389/fmicb.2012.00117.

[61] P.M. Colman, Influenza virus neuraminidase: Structure, antibodies, and inhibitors, Protein Sci. 3 (1994) 1687–1696. https://doi.org/10.1002/pro.5560031007.

[62] C.M. Spruit, N. Nemanichvili, M. Okamatsu, H. Takematsu, G.J. Boons, R.P. de Vries, N-glycolylneuraminic acid in animal models for human influenza a virus, Viruses. 13 (2021) 1–17. https://doi.org/10.3390/v13050815.

[63] L. Bourouiba, Turbulent Gas Clouds and Respiratory Pathogen Emissions: Potential Implications for Reducing Transmission of COVID-19, JAMA - J. Am. Med. Assoc. 323 (2020) 1837–1838. https://doi.org/10.1001/jama.2020.4756.

[64] R.R. Netz, W.A. Eaton, Physics of virus transmission by speaking droplets, Proc. Natl. Acad. Sci. U. S. A. 117 (2020) 25209–25211. https://doi.org/10.1073/pnas.2011889117.

[65] L. Bourouiba, E. Dehandschoewercker, J.W.M. Bush, Violent expiratory events: On coughing and sneezing, J. Fluid Mech. 745 (2014) 537–563. https://doi.org/10.1017/jfm.2014.88.

[66] H. Zhu, R.W. Dexter, R.D. Fox, D.L. Reichard, R.D. Brazee, H.E. Ozkan, Effects of polymer composition and viscosity on droplet size of recirculated spray solutions, J. Agric. Eng. Res. 67 (1997) 35–45. https://doi.org/10.1006/jaer.1997.0151.

[67] B. Keshavarz, E.C. Houze, J.R. Moore, M.R. Koerner, G.H. McKinley, Ligament Mediated Fragmentation of Viscoelastic Liquids, Phys. Rev. Lett. 117 (2016) 1–6. https://doi.org/10.1103/PhysRevLett.117.154502.

[68] F.E. Buckland, D.A.J. Tyrrell, Experiments on the spread of colds, J. Hyg. Camb. 64 (1964) 365–378.

[69] G.J. Harper, Airborne micro-organisms: Survival tests with four viruses, J. Hyg. (Lond). 59 (1961) 479–486. https://doi.org/10.1017/S0022172400039176.

[70] K. Lin, C.R. Schulte, L.C. Marr, Survival of MS2 and Φ6 viruses in droplets as a function of relative humidity, pH, and salt, protein, and surfactant concentrations, PLoS One. 15 (2020) e0243505. https://doi.org/10.1371/journal.pone.0243505.

[71] D.H. Morris, K.C. Yinda, A. Gamble, F.W. Rossine, Q. Huang, T. Bushmaker, R.J. Fischer, M. Jeremiah Matson, N. van Doremalen, P.J. Vikesland, L.C. Marr, V.J. Munster, J.O. Lloyd-Smith, Mechanistic theory predicts the effects of temperature and humidity on inactivation of sars-cov-2 and other enveloped viruses, Elife. 10 (2021). https://doi.org/10.7554/ELIFE.65902.

[72] J.D. Noti, F.M. Blachere, C.M. McMillen, W.G. Lindsley, M.L. Kashon, D.R. Slaughter, D.H. Beezhold, High Humidity Leads to Loss of Infectious Influenza Virus from Simulated Coughs, PLoS One. 8 (2013) e57485. https://doi.org/10.1371/journal.pone.0057485.

[73] A.J. Prussin, D.O. Schwake, K. Lin, D.L. Gallagher, L. Buttling, L.C. Marr, Survival of the enveloped virus Phi6 in droplets as a function of relative humidity, absolute humidity, and temperature, Appl. Environ. Microbiol. 84 (2018). https://doi.org/10.1128/AEM.00551-18.

[74] W. Yang, L.C. Marr, Mechanisms by which ambient humidity may affect viruses in aerosols, Appl. Environ. Microbiol. 78 (2012) 6781–6788. https://doi.org/10.1128/AEM.01658-12.

[75] W. Yang, L.C. Marr, Dynamics of airborne influenza A viruses indoors and dependence on humidity., PLoS One. 6 (2011) e21481. https://doi.org/10.1371/journal.pone.0021481.

[76] E.P. Vejerano, L.C. Marr, Physico-chemical characteristics of evaporating respiratory fluid droplets, J. R. Soc. Interface. 15 (2018) 1–10. https://doi.org/10.1098/rsif.2017.0939.

[77] J.E. Benbough, Some factors affecting the survival of airborne viruses., J. Gen. Virol. 10 (1971) 209–220. https://doi.org/10.1099/0022-1317-10-3-209.

[78] C. Seyfert, J. Rodríguez-Rodríguez, D. Lohse, A. Marin, Stability of respiratory-like droplets under evaporation, Phys. Rev. Fluids. 7 (2022) 1–12. https://doi.org/10.1103/PhysRevFluids.7.023603.

[79] R.J. Salo, D.O. Cliver, Effect of acid pH, salts, and temperature on the infectivity and physical integrity of enteroviruses, Arch. Virol. 52 (1976) 269–282. https://doi.org/10.1007/BF01315616.

[80] Y.Y. Feng, S.L. Ong, J.Y. Hu, X.L. Tan, W.J. Ng, Effects of pH and temperature on the survival of coliphages MS2 and Qβ, J. Ind. Microbiol. Biotechnol. 30 (2003) 549–552. https://doi.org/10.1007/s10295-003-0080-y.

[81] A. Rasheed, S. Sharma, P. Kabi, A. Saha, S. Chaudhuri, S. Basu, Precipitation dynamics of surrogate respiratory sessile droplets leading to possible fomites, J. Colloid Interface Sci. 600 (2021) 1–13. https://doi.org/10.1016/j.jcis.2021.04.128.

[82] C.Y.H. Chao, M.P. Wan, L. Morawska, G.R. Johnson, Z.D. Ristovski, M. Hargreaves, K. Mengersen, S. Corbett, Y. Li, X. Xie, D. Katoshevski, Characterization of expiration air jets and droplet size distributions immediately at the mouth opening, J. Aerosol Sci. 40 (2009) 122–133. https://doi.org/10.1016/j.jaerosci.2008.10.003.

[83] Duguid JP, The and droplet-nuclei.size and duration of air-carriage of respiratory droplets, J Hyg. 44 (1944) 471–479.

[84] S. Yang, G.W.M. Lee, C.-M. Chen, C.-C. Wu, K.-P. Yu, The Size and Concentration of Droplets Generated by Coughing in Human Subjects, J. Aerosol Med. 20 (2007) 484–494. https://doi.org/10.1089/jam.2007.0610.

[85] R.S. PAPINENI, F.S. ROSENTHAL, The Size Distribution of Droplets in the Exhaled Breath of Healthy Human Subjects, J. Aerosol Med. 10 (2009) 105–116. https://doi.org/10.1089/jam.1997.10.105.

[86] G. Zayas, M.C. Chiang, E. Wong, F. MacDonald, C.F. Lange, A. Senthilselvan, M. King, Cough aerosol in healthy participants: Fundamental knowledge to optimize droplet-spread infectious respiratory disease management, BMC Pulm. Med. 12 (2012). https://doi.org/10.1186/1471-2466-12-11.

[87] M. Abkarian, S. Mendez, N. Xue, F. Yang, H.A. Stone, Speech can produce jet-like transport relevant to asymptomatic spreading of virus, Proc. Natl. Acad. Sci. U. S. A. 117

(2020) 25237–25245. https://doi.org/10.1073/pnas.2012156117.

[88] J. Gralton, E. Tovey, M.-L. McLaws, W.D. Rawlinson, The role of particle size in aerosolised pathogen transmission: a review., J. Infect. 62 (2011) 1–13. https://doi.org/10.1016/j.jinf.2010.11.010.

[89] J. Macfarlane, W. Holmes, P. Gard, R. Macfarlane, D. Rose, V.B. Weston, M. Leinonen, P. Saikku, S. Myint, Prospective study of the outcome of adult Lower Resperatory Tract illness (LRTi) in the community and the relationship to aetiology and management, Thorax. 54 (1999) 109–114.

[90] D. Bhavnani, E.R. James, K.E. Johnson, S. Beaudenon-Huibregtse, P. Chang, P.J. Rathouz, M. Weldon, A. Matouschek, A.E. Young, SARS-CoV-2 viral load is associated with risk of transmission to household and community contacts, BMC Infect. Dis. 22 (2022) 1–11. https://doi.org/10.1186/s12879-022-07663-1.

[91] S. Anand, Y.S. Mayya, Size distribution of virus laden droplets from expiratory ejecta of infected subjects, Sci. Rep. 10 (2020) 1–9. https://doi.org/10.1038/s41598-020-78110-x.

[92] Z. Zuo, T.H. Kuehn, H. Verma, S. Kumar, S.M. Goyal, J. Appert, P.C. Raynor, S. Ge, D.Y.H. Pui, Association of airborne virus infectivity and survivability with its carrier particle size, Aerosol Sci. Technol. 47 (2013) 373–382. https://doi.org/10.1080/02786826.2012.754841.

[93] C. Alonso, P.C. Raynor, P.R. Davies, M. Torremorell, Concentration, size distribution, and infectivity of airborne particles carrying swine viruses, PLoS One. 10 (2015) 1–12. https://doi.org/10.1371/journal.pone.0135675.

[94] M. Pan, L. Carol, J.A. Lednicky, A. Eiguren-Fernandez, S. Hering, Z.H. Fan, C.Y. Wu, Determination of the distribution of infectious viruses in aerosol particles using water-based condensational growth technology and a bacteriophage MS2 model, Aerosol Sci. Technol. 53 (2019) 583–593. https://doi.org/10.1080/02786826.2019.1581917.

[95] O. Lieleg, C. Lieleg, J. Bloom, C.B. Buck, K. Ribbeck, Mucin biopolymers as broad-spectrum antiviral agents, Biomacromolecules. 13 (2012) 1724–1732. https://doi.org/10.1021/bm3001292.Mucin.

[96] V.J. Schömig, B.T. Käsdorf, C. Scholz, K. Bidmon, O. Lieleg, S. Berensmeier, An optimized purification process for porcine gastric mucin with preservation of its native functional properties, RSC Adv. 6 (2016) 44932–44943. https://doi.org/10.1039/c6ra07424c.

[97] B. Winkeljann, K. Boettcher, B.N. Balzer, O. Lieleg, Mucin Coatings Prevent Tissue Damage at the Cornea–Contact Lens Interface, Adv. Mater. Interfaces. 4 (2017) 1–10. https://doi.org/10.1002/admi.201700186.

[98] A. Gaillard, R. Sijs, D. Bonn, What determines the drop size in sprays of polymer solutions?, J. Nonnewton. Fluid Mech. 305 (2022) 104813. https://doi.org/10.1016/j.jnnfm.2022.104813.

[99] B. Keshavarz, E.C. Houze, J.R. Moore, M.R. Koerner, G.H. McKinley, Rotary atomization of newtonian and viscoelastic liquids, Phys. Rev. Fluids. 5 (2020). https://doi.org/10.1103/PhysRevFluids.5.033601.

[100] J.R. Davies, I. Carlstedt, Isolation of large gel-forming mucins., Methods Mol. Biol. 125 (2000) 3–13. https://doi.org/10.1385/1-59259-048-9:003.

[101] R.J. Simpson, Homogenization of mammalian tissue, Cold Spring Harb. Protoc. (2010). https://doi.org/10.1101/pdb.prot5455.

[102] Biopolymers for Biomedical and Biotechnological Applications, 2020. https://doi.org/10.1002/9783527818310.

[103] N.L. Kavanaugh, A.Q. Zhang, C.J. Nobile, A.D. Johnson, K. Ribbeck, Mucins suppress virulence traits of Candida albicans, MBio. 5 (2014) 1–8. https://doi.org/10.1128/mBio.01911-14.

[104] B.F. Smith, J.T. LaMont, Hydrophobic binding properties of bovine gallbladder mucin, J. Biol. Chem. 259 (1984) 12170–12177. https://doi.org/10.1016/s0021-9258(20)71335-9.

[105] C.E. Wagner, G.H. McKinley, Age-dependent capillary thinning dynamics of physically-associated salivary mucin networks, J. Rheol. (N. Y. N. Y). 61 (2017) 1309–1326. https://doi.org/10.1122/1.4997598.

[106] M. Marczynski, K. Jiang, M. Blakeley, V. Srivastava, F. Vilaplana, T. Crouzier, O. Lieleg, Structural Alterations of Mucins Are Associated with Losses in Functionality, Biomacromolecules. 22 (2021) 1600–1613. https://doi.org/10.1021/acs.biomac.1c00073.

[107] J. Kočevar-Nared, J. Kristl, J. Šmid-Korbar, Comparative theological investigation of crude gastric mucin and natural gastric mucus, Biomaterials. 18 (1997) 677–681. https://doi.org/10.1016/S0142-9612(96)00180-9.

[108] A.W. Larhed, P. Artursson, E. Björk, The influence of intestinal mucus components on the diffusion of drugs, Pharm. Res. 15 (1998) 66–71. https://doi.org/10.1023/A:1011948703571.

[109] N. Nikogeorgos, N.J. Patil, B. Zappone, S. Lee, Interaction of porcine gastric mucin with various polycations and its influence on the boundary lubrication properties, Polymer (Guildf). 100 (2016) 158–168. https://doi.org/10.1016/j.polymer.2016.08.030.

[110] M. Derrien, M.W.J. Van Passel, J.H.B. Van De Bovenkamp, R.G. Schipper, W.M. De Vos, J. Dekker, Structural Mucin of Intestinal Mucus in Human and Mouse, Gut MicrobesM. 1 (2010) 254–268. www.landesbioscience.com.

[111] K.B. Smith-Dupont, C.E. Wagner, J. Witten, K. Conroy, H. Rudoltz, K. Pagidas, V. Snegovskikh, M. House, K. Ribbeck, Probing the potential of mucus permeability to signify preterm birth risk, Sci. Rep. 7 (2017) 10302. https://doi.org/10.1038/s41598-017-08057-z.

[112] J.P. Celli, B.S. Turner, N.H. Afdhal, S. Keates, I. Ghiran, C.P. Kelly, R.H. Ewoldt, G.H. McKinley, P. So, S. Erramilli, R. Bansil, Helicobacter pylori moves through mucus by reducing mucin viscoelasticity, Proc. Natl. Acad. Sci. U. S. A. 106 (2009) 14321–14326. https://doi.org/10.1073/pnas.0903438106.

[113] E.S. Frenkel, K. Ribbeck, Salivary mucins protect surfaces from colonization by cariogenic bacteria, Appl. Environ. Microbiol. 81 (2015) 332–338. https://doi.org/10.1128/AEM.02573-14.

[114] P. Georgiades, P.D.A. Pudney, D.J. Thornton, T.A. Waigh, Particle tracking microrheology of purified gastrointestinal mucins, Biopolymers. 101 (2014) 366–377. https://doi.org/10.1002/bip.22372.

[115] C.E. Wagner, M. Krupkin, K.B. Smith-Dupont, C.M. Wu, N.A. Bustos, J. Witten, K.

Ribbeck, Comparison of Physicochemical Properties of Native Mucus and Reconstituted Mucin Gels, Biomacromolecules. 24 (2023) 628–639.

2.5 Acknowledgements

Text from this chapter has been adapted from: N.A. Bustos, K. Ribbeck, C.E. Wagner. The role of mucosal barriers in disease progression and transmission. Adv. Drug Deliv. https://doi.org/10.1016/j.addr.2023.115008

This research was supported by the funding from the National Science Foundation, a GRFP award to N.A.B. (grant no. 1745302).

Chapter 3

Transport of physiochemically diverse bacteriophage viruses in mucin gels

3.1 Abstract

One of the most abundant biological groups in the mucosal environment are bacteriophages, or phages; these viruses specifically target and kill bacteria. Phages influence nearly all processes bacteria perform in our body- from digesting food, to building vitamins, and metabolizing drugs. While phages have been extensively studied in the absence of mucus, the contributions of mucin, mucus' native polymer, to their physical transport remains an area of interest for studying viral dynamics. Given their accessibility and relative safety compared to infectious human viruses, we use several 'tailed' phage as a semi wildtype viral particle model system to study the effect of different native mucins on the transport of viruses with different physical and biochemical properties. Specifically, we track fluorescent phage dispersed in reconstituted mucin gels simulating the intestinal and respiratory mucus layers using single particle tracking methods. We observe that phage have different transport properties not only influenced by their geometrical size but also by their surface chemistries. In particular, we found that T3, T4, and T7 phage are relatively unhindered by the presence of mucins, while T5 phage are slowed down and exhibit subdiffusive behavior. Importantly, we found that phage with normal diffusive dynamics (i.e., T3, T4, and T7) had varying degrees of Gaussian to non-Gaussian distributed step sizes. Ultimately, an understanding of phage transport may guide the synthesis of engineered phage with tunable transport properties and provides a framework for modeling viruses in within-host disease models.

3.2 Introduction

Bacteriophage (phage) are bacterial viruses that are the most abundant and diversified biological entity on Earth [1]; they can be detected in all areas where bacteria exist including the human body [2]. The human gut alone contains approximately 10^{15} phage [3]. The microbiota and phage are supported by the nutrients and the physical network provided by mucus covering

epithelial surfaces of the body. The role of phages residing in the gut on human health and disease has only recently started to be recognized; phage can live among bacterial communities or modify microbiota by affecting mucus (i.e., phage-mucus interactions) or changing bacterial abundance, diversity, and virulence (i.e., phage-bacteria interactions) [2,4]. Phage are also being introduced into the body as therapies to treat gastrointestinal diseases [5] and pulmonary infections [6], in particular those caused by multi-drug resistant pathogens.

Apart from their role in shaping bacterial population dynamics and evolution, phage are considered model systems for studying virus emergence and viral ecology given their ease of use in the laboratory and their biological safety level compared to infectious human viruses [7–10]. Although in vitro mucus environments may not capture all aspects of the natural host environment, they can be used to carefully manipulate single factors (such as mucin type, physical network structure, or phage population size) to determine their influence on viral progression or viral transport behavior.

Phage typically consist of a capsid or protein hull containing genetic material and some also have a ‘tail’ that serves for injecting genetic material into a bacteria [11]. They are classified according to various parameters, including their morphological characteristics, nucleic acid content, and bacterial target [12]. Many phage have evolved to encode specific glycan-binding and glycan-cleaving proteins that allow them to recognize not only a range of bacterial glycans but also human glycans displayed on mucins, the primary structural component of mucus [12,13]. By degrading mucus, phage may influence the network of mucus and consequently, modify the spatial-temporal behaviors of phage and other molecules. By binding to mucus, phage mobility may be facilitated or constrained thus impacting their ability to penetrate through mucus and potentially impacting their killing behavior [4]. In addition to phage encoded-proteins, phage particle charge, phage geometry, and physical properties of mucus including pore size, structure, and viscosity may impact their transport through mucus.

Phage libraries of natural and ‘engineered’ phage contain a diversity of phage with different geometries and surface properties, however, the study of their mobility in mucus is limited. Work by Barr and colleagues using mucus from reconstituted commercial mucin demonstrated that T4 moves through mucus by sub-diffusion to increase their encounter rate with bacterial hosts [14,15]. There is great scientific interest in the physical and biochemical properties of phage. This interest extends beyond guiding the development of phage with predictable transport properties for therapeutic applications [5,6], as it also contributes to informing the modeling of virus progression.

Here, we study the transport of several natural phages, including T3, T4, T5, T7 and nanoparticles of comparable size in mucin gels. In order to reduce the effects of the variability in mucus composition, reconstituted solutions of purified mucins were used to capture the rheological and bioactive properties of native mucus. We found that phage have different transport abilities influenced by their geometries and surface chemistries and are relatively unhindered in the mucin environment compared to nanoparticles. We begin this chapter by explaining the preparation of samples and experimental technique and analysis for measuring particle transport, referred to as single-particle tracking (SPT). Then, we conclude this chapter with SPT results and discussion.

3.3 Materials and Methods

3.3.1 Experimental details

Mucin Purification and Reconstitution of Mucin Hydrogels

MUC5AC mucins were purified from fresh pig stomach scrapings and MUC2 mucins were purified from fresh pig intestinal scrapings following the methods described previously [16]. Briefly, the mucus scrapings were solubilized in sodium chloride buffer containing protease inhibitors and sodium azide to prevent mucin degradation and bacterial proliferation, respectively [17], and then centrifuged to remove insoluble components. The mucins were isolated using gel filtration chromatography on a Sepharose column (CL2B), and then concentrated, desalted, and lyophilized [17]. Mucins were weighed and solubilized for 24 hours with gentle shaking at 4 °C in SM buffer (100 mM NaCl, 8 mM $MgSO_4 \bullet 7H_2O$, 50 mM Tris-Cl (pH 7.5) [18]). A viscous micropipette was used to adequately mix gels before performing tests.

Preparation of Carboxymethylcellulose (CMC) gels

CMC sodium salt, average molecular weight = 250 kDa and degree of substitution = 0.7 (CAS: 9004-32-4) purchased from Acros Organics (Thermo Fisher Scientific, Waltham, MA, USA) was used to prepare a solution of CMC in distilled water at 50 mg/mL. The CMC solution was dialyzed against distilled water in an Amicon stirred cell (UFSC40001, Amicon) equipped with a 100 kDa molecular weight cut-off membrane. Dialysis was performed with two exchanges of water and the resulting solution was concentrated before lyophilization. Dried CMC was stored at -80 °C until use. CMC was weighed and solubilized for 24 hours with gentle shaking at 4 °C in

SM buffer. Following gentle shaking overnight, the CMC solution was then micropipetted up and down several times to ensure adequate mixing.

Preparation of Sigma Porcine Gastric Mucin (PGM) Gels

PGM (Sigma Aldrich, St. Louis, MO, USA) was weighed and solubilized for 24 hrs with gentle shaking and 4 C in d_2H_2O buffer. Following gentle shaking overnight, the PGM solution was then micropipetted up and down to ensure adequate mixing and was diluted in equal parts with 2X SM buffer for use in SPT tests as “unfiltered PGM”. For tests with “filtered PGM”, PGM solution centrifuged at 5,000 $\times$ g for 20 min and passed through a 0.45 μm filter to remove insoluble components. Next, 100% EtOH was added to a final concentration of 70% (v/v) to precipitate the soluble PGM. This solution was centrifuged at 5,000 $\times$ g for 20 min. The supernatant was discarded, and the pellet was resuspended in d_2H_2O. This solution was snap frozen by plunging into liquid nitrogen and lyophilized. The subsequent purified material was weighed and dissolved in SM buffer.

Preparation of phage

Phage were amplified using methods as previously described [19]. Briefly, an overnight of a permissive host (BL 21 DE3 for T3, T4, T7, and MG1655 for T5) was diluted 1:10 into fresh media. The culture was grown at 37 C until reaching an optical density (O.D.) of approximately 0.2. Then, approximately 10^6 PFU of phage was added to the culture and incubated at 37 °C, shaking at 200 rpm until the culture completely lysed. Chloroform was added to the flask for a final concentration of 10% (v/v) and the sample was vortexed and centrifuged for 10 min at 5000 $\times$ g. The supernatant was transferred to a new tube. The amplified phages were purified by adding one volume of a precipitation buffer (20% polyethylene glycol (PEG) 8,000 and 2.5 M sodium chloride (NaCl)). The phages were precipitated at 4 °C overnight and then centrifuged for 10 min at 10,000 $\times$ g at 4 °C. The supernatant was removed and the phage pellet was resuspended in SM buffer. The purified phage was titered using a permissive host and previously established methods. Phage were fluorescently labeled by incubating with 10x SYBR gold (Thermo Fisher Scientific, Waltham, MA) and shaking at room temperature for one hour. Excess dye was removed by pelleting the phage through adding one volume of 20% (w/v) PEG, 2.5 M NaCl solution and incubating 4 °C for three hours. The solution was centrifuged at 4 °C at 10,000 $\times$ g for 14 min. The supernatant was discarded, and the pellet was resuspended in SM buffer. The labeled phages were titered using established protocols and stored at 4 °C until use.

Particle characterization

Hydrodynamic diameter and zeta potential of phage and nanoparticles were determined with dynamic light scattering using a Zetasizer Nano ZS (Malvern Panalytical, Malvern, UK). Particles were diluted in MilliQ water to a final concentration between 10^5-10^6 particles/mL. Approximately 740 μL of sample was placed in a disposable plastic cuvette which was then sealed with a dip cell. This was repeated three times for size and zeta potential tests, respectively. We report the mode size from the volume distribution because the mode size population will make up the greatest proportion of the tracked population in SPT. By contrast, identifying the peak size from the intensity distribution, may heavily bias large particles, even if only a smaller proportion are present, because they scatter more light relative smaller particles. An average and standard deviation was calculated from replicates. We additionally report the polydispersity index (PI) calculated by the Zetasizer Nano ZS software; the index is a number calculated from a parameter fit to the dynamic light scattering correlation data. An average and standard deviation was calculated from replicates. The PI is a dimensionless number and is scaled such that low PI values (PI<0.05) are indicative of highly monodisperse particles while values greater than 0.7 are indicative of samples with a broad size distribution.

SPT experiments

In SPT, the spatial location of particles dispersed in a sample of interest is recorded over time. For the experiments performed in this chapter, SPT samples were prepared by combining samples with nanoparticles or phage at different dilutions. Previously diluted nanoparticles were combined with samples at a ratio of 60:1 (sample:nanoparticle solution); this resulted in an overall dilution ratio of 1:12,000 for the nanoparticles. Several fluorescent nanoparticles were used in this study, including: negatively charged (carboxylated) particles 200 nm in diameter (Magsphere, Inc., Cat No. CAYF-200NM), positively charged (aminated) particles 200 nm in diameter (Magsphere, Inc., Cat No. AMYF-200NM), negatively charged particles 100 nm in diameter (Magsphere, Inc., Cat No. CAYF-100NM), positively charged particles 100 nm in diameter (Magsphere, Inc., Cat No. AMYF-100NM), and negatively charged particles 500 nm in diameter (Magsphere, Inc., Cat No. CAYF-500NM). Phage concentrations varied and were much lower than commercial nanoparticles. Phage were combined with samples at a ratio of 1:30, 1:80, 1:2, and 1:10, for T3, T7, T5, and T4, respectively.

All particle-laden samples were adequately mixed using a pipette and loaded into either a channel fabricated using a microscope slide and cover slip or borosilicate square capillaries

(Vitrocom, Part No. 8290) depending on the size of the particle. Microscope slide channels were used for all phage, 100 nm diameter nanoparticles, and 200 nm diameter nanoparticles. Capillaries were used for 500 nm diameter particles. In brief, for the microscope slide channel, two pieces of double-sided tape were placed parallel to each other on a microscope slide and a cover slip was pressed on top. Approximately 10 μL of sample was pipetted into a fabricated microscope slide channel and approximately 30 μL was required to fill 2 cm long borosilicate capillaries. The ends of the microscope slide channel and the ends of the capillaries were sealed with a 1:1:1 mixture of Vaseline, lanolin, and paraffin, to prevent evaporation.

Slide samples were imaged at room temperature with an Axio Observer D.1 inverted microscope either a Zeiss LD Plan-Apochromat 100x/1,4 Oil Ph3 objective lens (for all phage, 100 nm diameter nanoparticles, and 200 nm diameter nanoparticles) or Zeiss LD Plan-Neofluar 40x/0.4 Corr Ph2 objective lens (for 500 nm diameter nanoparticles) and Hamamatsu Flash 4.0 C11440022CU camera. Imaging was done at a frame rate of 30.3 frames per second and an exposure time of 33 ms to record 10 second movies. Between 10 and 12 movies at different spatial locations within the channel were recorded for each sample.

All image frames were processed using a modified version of a publicly available SPT MATLAB (Natwick, MA) code to identify and track particles [20,21]. The code identifies particles by the brightest pixels and then the positions of every candidate particle are adjusted using an intensity-weighted centroid method. The code then generated particle trajectories by linking particle positions in adjacent frames using criteria such as feature size, maximum displacement between consecutive frames, and minimum trajectory length (i.e., minimum number of frames to form a trajectory). Finally, a drift correction [21] was applied to all SPT data; the correction subtracts the center of mass motion of all particles in a given time frame from each individual trajectory. The SPT data was then semi-automatically reviewed using an in-house code; the code categorizes trajectories as “good” or “bad” tracks using the population step size distributions and directionality of individual particle trajectories. “Good” tracks are used for analysis. “Bad” tracks are tracks erroneously connected by the SPT code, which can be a result of noise (spurious) pixels connected to each other or aggregates of particles and/or non-particle components that are connected to form a trajectory. From the population step size distributions, trajectories with step sizes with low probability ($P<0.02$) compared to the rest of the particle population are removed; this removes trajectories that have large improbable step sizes. In addition, the directionality of trajectories is determined by calculating the angle of consecutive steps in particle’s trajectory; a trajectory is categorized as “bad” if the particle moved in a

straight line for several steps. The user may also review the tracks and manually remove tracks including misidentified particles.

3.3.2 Theory and analysis

Following verification for erroneous trajectories and misidentified particles, particle trajectories were analyzed to extract population-level and particle-level descriptions of transport including diffusivity, heterogeneity of particle motions, and space-filling ability of particle trajectories. In homogenous Newtonian fluids, passive particles undergo motion normal diffusion or Brownian motion, whereby the motion of particles is dictated by the random collisions of passive particles with solvent molecules [22]. In normal diffusion, particle step sizes are normally distributed and the particle mean squared displacement increases linearly with time. In biological hydrogels such as mucus, particles can have subdiffusive or anomalous diffusive behavior leading to non-Gaussian or exponentially distributed step sizes. This can be attributed to binding interactions between the particle and the hydrogel (discussed in Section 2.2), polydispersity of the particle population [23], and heterogeneity of the hydrogel [24,25].

Determination of mean squared displacement (MSD)

The time averaged mean squared displacement (TAMSD, in two dimensions (2D)) of the jth particle for a movie with M images was calculated from the drift corrected data and is given by [22,26]

$$\Delta r_j^2\bar{(}\Delta\tau) = \frac{1}{M-\frac{\Delta\tau}{\Delta t}}\sum_{i=1}^{M-\frac{\Delta\tau}{\Delta t}}[(x_j(i\Delta t+\Delta\tau)-x_j(i\Delta t))^2+(y_j(i\Delta t+\Delta\tau)-y_j(i\Delta t))^2], \quad (3.1)$$

where Δt is the time between successive frames and $\Delta\tau$ is the lag time. The ensemble averaged MSD (MSD) over all N tracked particles is given by averaging over all TAMSDs as follows [22]:

$$MSD = <\Delta r^2(\Delta\tau)> = \frac{1}{N}\sum_{j=1}^{N}\Delta r_j^2\bar{(}\Delta\tau)\,. \quad (3.2)$$

We calculated MSD fold change at a given lagtime by comparing MSD values in mucin gels to MSD values in buffer as follows:

$$Fold\ change = \frac{MSD_{gels}-MSD_{buffer}}{MSD_{buffer}}, \quad (3.3)$$

We used the overall average MSD value at a given lag time for particles in buffer (MSD_{buffer}) and used the individual replicate experimental MSD values at a given lag time for particles in gels (MSD_{gels}).

To extract mobility parameters, the MSD determined from equation 3.2 is fitted to the general 2D power law form as [22]

$$< \Delta r^2(\Delta\tau) > = 4D_\alpha \Delta\tau^\alpha \quad (3.4)$$

where D_α is a generalized diffusion coefficient and α is the diffusional exponent. When α <1, the motion of the particle is subdiffusive, and when α >1, the motion is super diffusive. Normal diffusion or Brownian motion is assigned when α =1. While the MSD can vary with lag time, here a characteristic diffusion exponent α and generalized diffusion coefficient D_α are defined by fitting equation 3.3 to the MSD data for lag times 0.033≤ $\Delta\tau$ ≤0.33 s (i.e., first 10 data points). This analysis was repeated for each sample replicate; in addition, for each replicate, the generalized diffusion coefficient and α were extracted from each TAMSD (i.e., individual particle MSDs). Each condition was done in triplicate. The total number of trajectories per replicate varied. For each replicate, all the good trajectories were used for analysis, but in cases where the number of good trajectories exceeded 1000 (47 out of 63 total samples), we randomly selected a subset of 1000 trajectories to use for analysis. In samples where fewer than 1000 good trajectories were retained (16 out of 63 total samples), there was an average of 519 trajectories per sample that were used for analysis.

Heterogeneity and van Hove distribution

Analyzing distributions of particle step sizes or van Hove distributions is a common way to investigate spatial or temporal heterogeneity in the behavior of individual particles. The one-dimensional step size distribution for a random walk at a given lag time $\Delta\tau$ is a Gaussian distribution about a mean displacement Δx=0 given by [27]

$$P(\Delta x, \Delta\tau) = \frac{1}{\sqrt{4\pi D\Delta\tau}} e^{-\frac{\Delta x^2}{4D\Delta\tau}}, \quad (3.4)$$

where D is the diffusion coefficient of the particle in the medium. For a Gaussian distribution, the kurtosis (or ratio of the 4th moment to the 2nd moment of the distribution) is 3. Hence, deviations from the above expression can be quantified using a “non-Gaussian parameter” defined as [28]

$$\kappa = \frac{<\Delta x^4>}{3<\Delta x^2>^2} - 1. \quad (3.5)$$

For normal Brownian motion, we expect $|\kappa| \ll 1$. A κ value was calculated for each replicate and the average value over three replicates is reported along with its standard deviation. Similarly, an average Van Hove distribution was plotted by averaging over the Van Hove's of three replicates and calculating the standard deviation for each histogram bin.

Space-filling capacity

The total area covered by individual trajectories (termed "coverage area" in the results) was determined by calculating the area encompassed within a 2-D boundary around the x and y points of the trajectory. This was done using the *boundary* function in MATLAB R2022a. The median area for each replicate was determined and an average value over three replicates was plotted along with its standard deviation.

In the following section, we utilize these analytical methods to interpret the motion of phage and nanoparticle in mucin gels.

3.4 Results and discussion

3.4.1 Characterization of phage and nanoparticles

We studied the transport of 4 fluorescently labeled phage, including T3, T4, T5, and T7, with different heights and widths reported in literature [29] (**Figure 3.1a**) in reconstituted mucin gels. Mucin gels with suspensions of phage were pipetted into microscope slide channels (**Figure 3.1b**) and their motion was recorded over ~10s, followed by SPT analysis to define ensemble averaged transport and individual particle transport. In addition, we determined the size and zeta potential of phage and charged nanoparticles for comparison. The charge of phage particles was similar to each other (average charge between -5.86 mV and -12.0 mV) and close to neutral charge (comparable to PEG coated particles [30]) despite differences in their physical structure (**Figure 3.1c**). On the other hand, carboxylated particles had a significantly greater electronegative charge (approximately -38 mV for 100 nm diameter and 500 nm diameter nanoparticles) and aminated particles had a large electropositive charge (47.96$\pm$7.0 mV for 200 nm diameter particles and 56.78$\pm$5.4 mV for 100 nm diameter particles) (**Figure 3.1c** and **Supplementary Figure S3.1a**). The hydrodynamic diameter of nanoparticles (**Figure 3.1d** and **Supplementary Figure S3.1b**) was consistent with the diameter of a sphere while the

hydrodynamic diameter of T4 and T5 diverged from their dimensions cited in literature (**Figure 3.1d**) likely due to their long tails; T3 and T7 have relatively short tails by comparison and measured a diameter proportional to the size of their capsid.

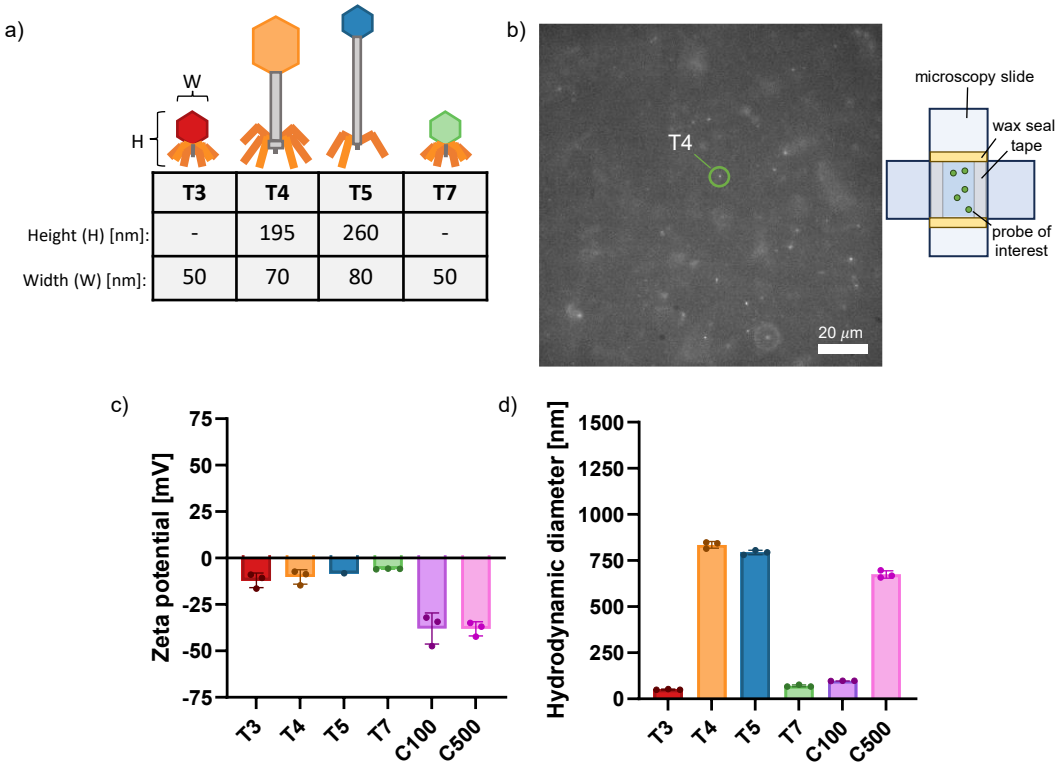

Figure 3.1 Bacteriophages (phages) have different geometries and surface charges. a Illustration of the 4 phages (T3, T4, T5, and T7) used in the study with their corresponding geometrical sizes cited in the literature [29]. **b** Microscopy images (left) of fluorescent T4 suspended in reconstituted 1% Muc2 mucin gels. Scale bar is 20 μm. The illustration (right) depicts the probes of interest suspended in an assembled microscopy slide channel (see Methods) used for single particle tracking (SPT). (**c, d) c** Zeta potential and **d** hydrodynamic diameter of phages and nanoparticles in MilliQ water. Measurements were done using a Zetasizer Nano ZS (Malvern Panalytical, Malvern, UK). We report the mode size from the volume distribution. Two different commercially available nanoparticles were used for comparison: 100 nm diameter carboxylated (C100) and 500 nm diameter carboxylated (C500). Each point represents an independent replicate and error bars indicate the standard deviation (n=3).

3.4.2 Ensemble-averaged transport in mucin gels

To investigate how mucin impacts phage transport, we performed live fluorescence imaging of phage and tracked their motion in reconstituted native mucin gels, including Muc2 gels and Muc5AC gels. The ensemble-average mean squared displacements (MSDs) of phage and carboxylated nanoparticles in 1% Muc2 and 1% Muc5AC are shown in **Figure 3.2a** and **Figure 3.2c**, respectively. The diffusion of T3 was fastest overall in both 1% Muc2 and 1% Muc5AC, followed by T7 and T4, and T5 and carboxylated nanoparticles. Although aminated particles are positively charged, their ensemble MSDs in either 1% Muc2 and 1% Muc5AC gels (**Supplementary figure S3.2a and S3.2c)** showed that binding mediated interactions with the network of negatively charged mucin did not distinguishably slow 'small' particles (100 nm and 200 nm diameter particles) down compared to negatively charged (carboxylated) particles. Both 100 nm diameter carboxylated particles and phage, except for T5, exhibited weakly subdiffusive ($0.90 \leq \alpha < 1$) to normal diffusive behavior ($\alpha \approx 1$) (**Figure 3.2b**, **Figure 3.2d**, **Supplementary Figure S3.1b**, and **Supplementary Figure S3.2d**); T5 was subdiffusive ($\alpha = 0.70 \pm 0.02$) in 1% Muc2 and carboxylated 500 nm diameter particles were also subdiffusive in both Muc2 ($\alpha = 0.44 \pm 0.03$) and Muc5AC ($\alpha = 0.57 \pm 0.04$). The generalized diffusion coefficient and diffusion exponent are independent of each other; the diffusivities of T3, T4, and T7 were higher in 1% Muc2 than in 1% Muc5AC (**Supplementary Figure S3.3**). We found that the average area covered by phage (i.e., space filling ability) (**Supplementary Figure S3.4**) corresponded to how diffusive the phage were in mucin gels (the height of the MSDs); more diffusive phage 'explored' more area in the mucin gels compared to less diffusive or subdiffusive phage.

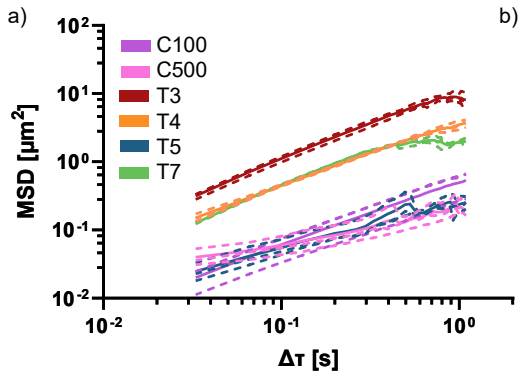

b)

	α
C100	0.93±0.03
C500	0.44±0.03
T3	1.08±0.02
T4	0.97±0.06
T5	0.70±0.05
T7	1.07±0.02

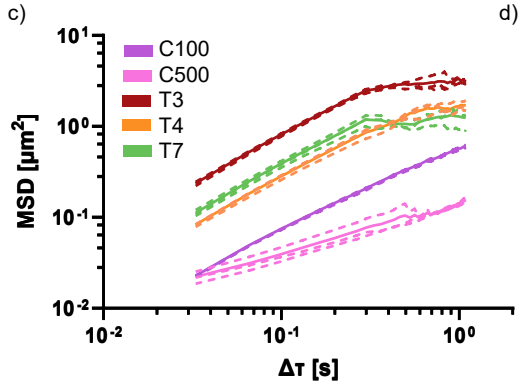

d)

	α
C100	0.99±0.02
C500	0.57±0.04
T3	1.05±0.01
T4	1.04±0.03
T5	NA
T7	1.03±0.03

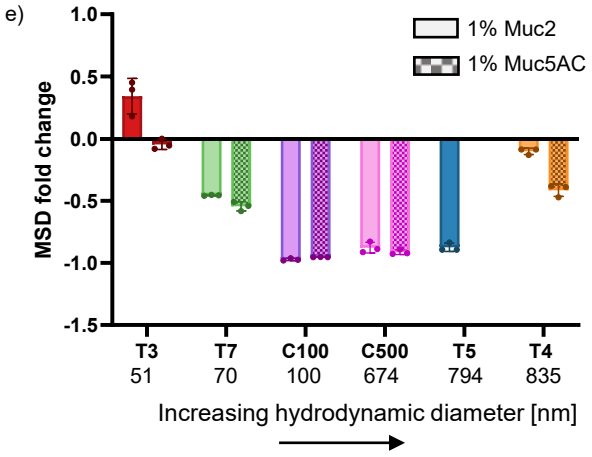

Figure 3.2 Phages have different diffusive behaviors in mucin gels that depend on both geometrical size and surface properties (e.g., charge and surface chemistry). (a, b) a Mean squared displacement (MSD) as a function of lag time ($\Delta\tau$) and **b** summary table of anomalous diffusion exponents, α, for different phage (T3, T4, T5, and T7), carboxylated 100 nm (C100) and 500 nm (C500) diameter nanoparticles in 1% Muc2. Dashed lines in **a** denote the ensemble-average MSD of an individual experiment and solid lines denote the

average over all experiments. **(c, d) c** Mean squared displacement (MSD) as a function of lag time ($\Delta\tau$) and **d** summary table of anomalous diffusion exponents, α, for different phage (T3, T4, and T7) and nanoparticles (C100 and C500) in 1% Muc5AC. Dashed lines in **c** denote the ensemble-average MSD of an individual experiment and solid lines denote the average over all experiments. **e** MSD fold change at $\Delta\tau$ = 0.198s for phage and nanoparticles in mucin gels compared to buffer. The fold change is calculated according to equation 3.2. 1% Muc2 is represented by a solid color and 1% Muc5AC is represented by a checker pattern. The x-axis is ordered by hydrodynamic diameter. The average hydrodynamic diameter is written below each corresponding x-axis label. Each point represents an independent replicate and error bars indicate the standard deviation (n=3).

The diffusional exponent (α) of T4 contrasted with previous results by Barr et al. who manually (i.e., user identified particles and linked their trajectories) measured the motion of T4 in commercial mucin (porcine gastric mucin (PGM) from Sigma) solubilized in SM buffer and reported subdiffusive behavior ($\alpha \approx 0.82$) [14]. We investigated whether differences in the ensemble diffusional exponent were due to mucin sources (e.g., commercial mucin versus lab purified mucin). We found that T4 followed normal diffusion in 1% Sigma PGM as we observed in lab purified mucin (**Supplementary Figure S3.5a**). From the TAMSDs of the population, the individual diffusional exponents of T4 demonstrate a range of diffusive behaviors (**Supplementary Figure S3.5b**); therefore, careful selection of tracking parameters, microscopy settings, prevention of user bias in both automatic or manual tracking is crucial to accurately capture the full range particle behaviors. Differences in the reported ensemble diffusional exponent of T4 in Sigma PGM was largely attributed to the preparation of PGM over the post-processing applied to SPT data (**Supplementary Figure S3.5c**). Unfiltered PGM (PGM that was used directly after solubilizing overnight) was observed to be more heterogenous compared to filtered PGM (PGM that was filtered after solubilizing overnight; see Methods). There were observable differences between the two PGM preparations; microscope images showed large fluorescent aggregates of insoluble PGM mixed with phage (compare **Supplementary Figure S3.5d** and **S3.5e**). T4 in unfiltered PGM had a lower ensemble diffusional exponent ($\alpha \approx 0.90 \pm 0.11$) compared to T4 in filtered PGM ($\alpha \approx 1.26 \pm 0.19$) (**Supplementary Figure S3.5c**); large aggregates were erroneously tracked as multiple constrained particles. By comparison, the post-processing of SPT data (see Methods) minimally affected the diffusive behavior (compare unfiltered PGM to unfiltered PGM* and filtered PGM to filtered PGM* in **Supplementary Figure S3.5c**); unfiltered PGM remained weakly subdiffusive and filtered PGM

went from apparent superdiffusive behavior to normal diffusive behavior after post-processing SPT data. We similarly found a range of diffusive behaviors and diffusivities for phages in 1% Muc2 (**Supplementary Figure S3.6**).

To determine whether phage are slowed down by the mucin network, particle transport in buffer (**Supplementary Figure S3.7a**) was measured to determine MSD fold change in buffer at a lagtime ($\Delta\tau$) of 0.198 s (**Figure 3.2e**). Particle transport in buffer was additionally compared to the theoretical MSDs of spherical particles diffusing in a Newtonian fluid with the viscosity of water (**Supplementary Figure S3.7b** and **S3.7c**). Among all phage and nanoparticles, T3 and T7 were observed to deviate the most from their corresponding theoretical MSD. Although all phage had a much higher polydispersity index relative to nanoparticles (**Supplementary Figure S3.7d**), indicating a broader size distribution, T3 and T7 were observed to have multiple peaks (1-2 additional peak sizes larger than the mode size in **Figure 3.1d**) in their volume distribution (not shown). Multiple peaks indicate distinct particle populations which we hypothesize contributed to TAMSDs that lowered the ensemble-average below the theoretical MSD. T3 also had the smallest mode size overall (~51 nm diameter), which may lead to an under sampling of “fast" trajectories because they may move quickly out of the focal plane and cannot be tracked or do not meet the minimum track length criteria.

MSD fold change was determined by comparing the MSD values of particles in mucin gels at $\Delta\tau$ = 0.198 s to the corresponding MSD values in buffer according to equation 3.3. We observed negative MSD fold changes for all particles except T3 (**Figure 3.2e**). A negative MSD fold change indicates that particles diffused faster in buffer compared to mucin gels. MSD fold changes closer to 0 indicate that the particle is minimally constrained, either by geometrical constraints or binding interactions, in the presence of the mucin network and travels comparable to its motion in buffer. Although T3 and T7 had similar hydrodynamic diameters and charge (**Figure 3.1c**, **3.1d**), T3 was unhindered in 1% mucin gels compared to T7 (**Figure 3.2e**). T3 was observed to travel faster in 1% Muc2 compared to buffer (positive MSD fold change) suggesting the possibility of interactions with mucin molecules that may enhance phage transport. However, this result may also be an artifact due to sampling issue in buffer as described above. In a similar fashion, T4 and T5 had similar size and charge (**Figure 3.1c**, **3.1d**), yet T5 was slowed down more in mucin gels (**Figure 3.2e**). Compared to nanoparticles of similar hydrodynamic diameter, T3, T7, and T4 were minimally constrained by the surrounding mucin network; this was most striking in the result of the MSD fold change of T4 compared to that of C500 because of its large hydrodynamic diameter. Importantly, the varied retention in

mucus was not strictly dependent on hydrodynamic diameter which demonstrated that surface properties, in addition to charge, influenced penetration through mucus.

3.4.3 Population and particle step-size distribution

The degree of heterogeneity of the motion of the ensemble population and individual particles in 1% Muc2 and 1% Muc5AC gels was investigated using van Hove distributions (i.e., distributions of step sizes at a given lag time). From the step size distributions of phage and nanoparticles at lag time 0.099 s (**Figure 3.3a** and **Figure 3.3b**), we calculated the non-Gaussian parameter (**Figure 3.3c** and **Figure 3.3d**). It is important to note that from the ensemble MSDs and diffusional exponents (**Figure 3.2a-d**) it is difficult to distinguish phage transport in Muc2 versus Muc5AC, however, from the step-size distributions we observed varying degrees of heterogeneity that suggest mucin-specific transport. We found that phage had varying degrees of Gaussian distributed step sizes. It is clear from the shapes of the distributions in Muc2 and Muc5AC that phage in Muc5AC deviated more from the expected parabolic-like profile (on a semi-log plot) for a Gaussian distribution. This deviation is also reflected in higher non-Gaussian parameter values, κ, in Muc5AC compared to κ in Muc2 for each phage. We hypothesize this effect is not largely due to differences in the physical mucin network structure of Muc2 gels and Muc5AC gels because carboxylated nanoparticles (of comparable length scales to phage in the study) did not show distinguishable differences in α or κ. It is possible that long tailed phage like T4 and T5 can undergo different steric interactions in Muc2 and Muc5AC that are not observed with spherical nanoparticles. Even T3, a small, short-tailed phage, which we expect is much smaller than the expected mesh size o fmucin gels, had differences in non-Gaussian parameter (κ=0.02 in Muc2 and κ=0.38 in Muc5AC) which suggest that heterogeneity of particle motions may arise from variation in physicochemical interactions between the phage and mucin molecules.

The maximum step size (at P=0.001) of T3, T7, and carboxylated 100 nm diameter nanoparticles remained approximately the same in both mucin types while the maximum step size of larger particles like T4 and carboxylated 500 nm diameter nanoparticles was marginally reduced in Muc5AC compared to the observed maximum step size in Muc2. This suggests that structural differences between Muc5AC and Muc2 may influence particle transport at length scales larger than the size of the phage and nanoparticles considered in this study. In addition

to differences in transport between gels of different mucin types, we also found that κ varied substantially in a given mucin gel between phage of comparable size, charge, and morphology (i.e., T3 and T7 vs T4 and T5). For instance, in Muc2, the motion of T3 phage was essentially Gaussian (κ = 0.02), while T7 phage exhibited a large degree of non-Gaussianity (κ = 0.51). These findings indicate that metrics other than overall surface charge and size may be critical in governing transport. For instance, previous work found that peptide probes of the same net charge but with different charge spatial configuration transport differently in mucin gels [31], which may also be the case here between different phage populations. Finally, we found that phage transport in 1% CMC gels, another negatively charged polymer that is frequently used as a synthetic mucin analog, was substantially different from that in mucin gels, particularly in terms of an overall greatly reduced maximum step size in CMC (**Supplementary Figure S3.8**).

To investigate the nature of individual particle trajectories in addition to the ensemble average, we calculated the non-Gaussian parameter for each particle trajectory ($\kappa_{particle}$) and plotted the results as a heatmap histogram in **Figure 3.3e** and **Figure 3.3f**. We show that on a single particle level several phage and nanoparticles showed broad variations (up to $\kappa \approx 0.6$) in the distributions of $\kappa_{particle}$. This held true even for T3 in Muc2 which had a Gaussian population κ ($\kappa = 0.02$) yet individual trajectories showed a range of $\kappa_{particle}$ between 0 and 0.4. By contrast, T5 had Gaussian distributed steps at the particle level and population Gaussian distributed steps. These results are different from our previous investigation [25] where we showed that the pooled step sizes across particles in different Newtonian environments produced exponentially distributed step sizes. Importantly, [25] explored spatial heterogeneity leading to non-Gaussian step-size distribution. In this study, we expect that mucin gels have low spatial heterogeneity and are single phase environments at neutral pH as shown in [24].

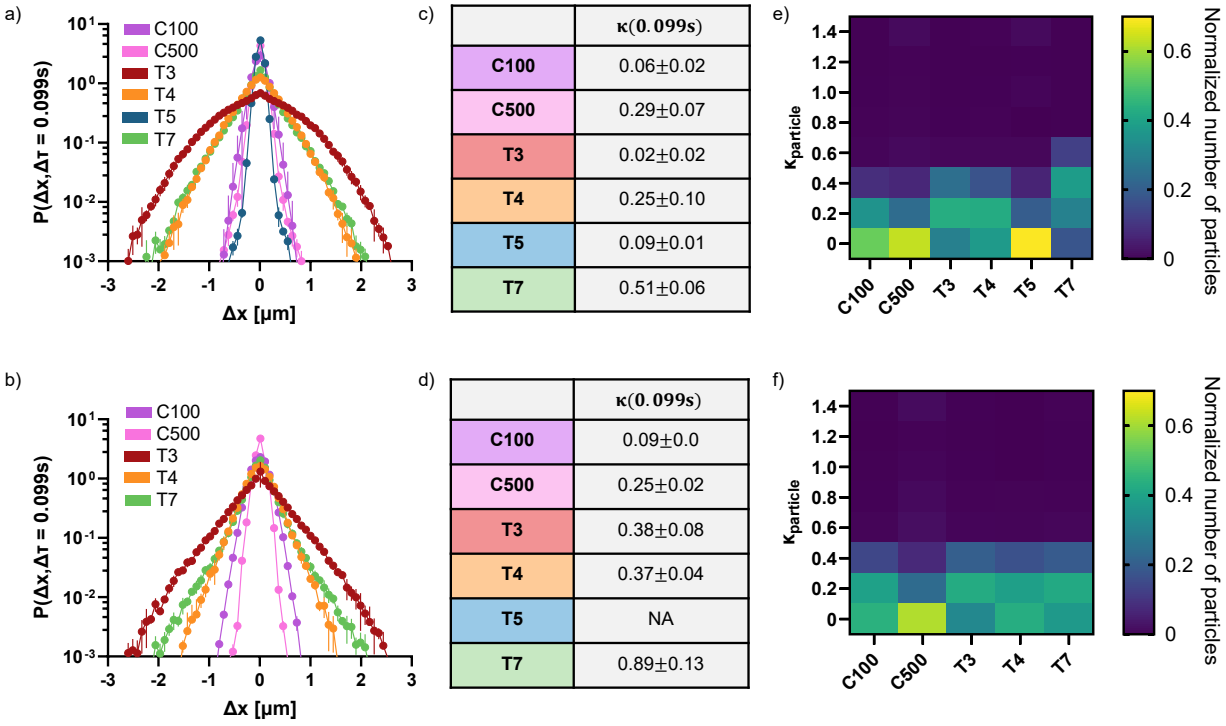

Figure 3.3 Phage diffuse with varying degrees of Gaussianity on a population level and single particle level. (a, b) van Hove correlations (i.e., distribution of all particle step sizes) in the x-direction (Δx) at lag time ($\Delta\tau$) 0.099s for **a** 1% Muc2 and **b** 1% Muc5AC gels. Each point represents the average of three replicates and the error bars represent the corresponding standard deviation (s.d.). **(c, d)** Summary table of the population non-Gaussian parameters (κ) at $\Delta\tau = 0.099$s for **c** 1% Muc2 and **d** 1% Muc5AC gels. The reported numbers represent the average±s.d. **(e, f)** Heatmap histogram of individual particle non-Gaussian parameter ($\kappa_{particle}$) for **e** 1% Muc2 and **f** 1% Muc5AC gels. The legend indicates the color that corresponds to the normalized number of particles (normalized by total number of tracked particles) with a κ value. $\kappa_{particle}$ was calculated from the van Hove correlation in the x-direction at lagtime 0.099 s. Two different commercially available nanoparticles were used for comparison: 100 nm diameter carboxylated (C100) and 500 nm

3.5 Conclusion

Using single particle tracking, we found that on average, phage diffused through mucin gels faster than nanoparticles of comparable size and one phage in particular, T3, was unhindered by the mucin network compared to its motion in buffer alone. In addition, the distribution of step sizes revealed additional characteristics of transport that could not be investigated by ensemble MSDs alone. Specifically, we found that phage that appeared to diffuse by normal diffusion ($\alpha \approx 1$) displayed variations in the Gaussianity of their step size distributions. This finding is important in the context of selecting or developing an appropriate transport model for these particles through complex media. Future work will explore how phage transport contributes to their replication and efficacy in killing bacteria. Ultimately, understanding the mechanism by which viruses move through mucus not only serves to improve existing disease progression models, but also for the development of strategies to sequester viruses before they reach their target cells.

3.6 References

[1] M.R.J. Clokie, A.D. Millard, A. V. Letarov, S. Heaphy, Phages in nature, Bacteriophage. 1 (2011) 31–45. https://doi.org/10.4161/bact.1.1.14942.

[2] Z. Naureen, A. Dautaj, K. Anpilogov, G. Camilleri, K. Dhuli, B. Tanzi, P.E. Maltese, F. Cristofoli, L. De Antoni, T. Beccari, M. Dundar, M. Bertelli, Bacteriophages presence in nature and their role in the natural selection of bacterial populations, Acta Biomed. 91 (2020) 1–13. https://doi.org/10.23750/abm.v91i13-S.10819.

[3] M. Dalmasso, C. Hill, R.P. Ross, Exploiting gut bacteriophages for human health, Trends Microbiol. 22 (2014) 399–405. https://doi.org/10.1016/j.tim.2014.02.010.

[4] D. Rothschild-Rodriguez, M. Hedges, M. Kaplan, S. Karav, F.L. Nobrega, Phage-encoded carbohydrate-interacting proteins in the human gut, Front. Microbiol. 13 (2023) 1–15. https://doi.org/10.3389/fmicb.2022.1083208.

[5] B. Gutiérrez, P. Domingo-Calap, Phage therapy in gastrointestinal diseases, Microorganisms. 8 (2020) 1–11. https://doi.org/10.3390/microorganisms8091420.

[6] R.Y.K. Chang, M. Wallin, Y. Lin, S.S.Y. Leung, H. Wang, S. Morales, H.K. Chan, Phage therapy for respiratory infections, Adv. Drug Deliv. Rev. 133 (2018) 76–86. https://doi.org/10.1016/j.addr.2018.08.001.

[7] J.J. Dennehy, Bacteriophages as model organisms for virus emergence research, Trends Microbiol. 17 (2009) 450–457. https://doi.org/10.1016/j.tim.2009.07.006.

[8] B. Koskella, C.A. Hernandez, R.M. Wheatley, Understanding the Impacts of Bacteriophage Viruses: From Laboratory Evolution to Natural Ecosystems, Annu. Rev. Virol. 9 (2022) 57–78. https://doi.org/10.1146/annurev-virology-091919-075914.

[9] C.A. Baker, A. Gutierrez, K.E. Gibson, Factors Impacting Persistence of Phi6 Bacteriophage, an Enveloped Virus Surrogate, on Fomite Surfaces, Appl. Environ. Microbiol. 88 (2022). https://doi.org/10.1128/aem.02552-21.

[10] C. Whitworth, Y. Mu, H. Houston, M. Martinez-Smith, J. Noble-Wang, A. Coulliette-Salmond, L. Rose, Persistence of bacteriophage phi 6 on porous and nonporous surfaces and the potential for its use as an ebola virus or coronavirus surrogate, Appl. Environ. Microbiol. 86 (2020) 1–11. https://doi.org/10.1128/AEM.01482-20.

[11] E. Beretta, Y. Kuang, Modeling and analysis of a marine bacteriophage infection, Math. Biosci. 149 (1998) 57–76. https://doi.org/10.1016/S0025-5564(97)10015-3.

[12] N. Principi, E. Silvestri, S. Esposito, Advantages and limitations of bacteriophages for the treatment of bacterial infections, Front. Pharmacol. 10 (2019) 1–9. https://doi.org/10.3389/fphar.2019.00513.

[13] D.J. Simpson, J.C. Sacher, C.M. Szymanski, Exploring the interactions between bacteriophage-encoded glycan binding proteins and carbohydrates, Curr. Opin. Struct. Biol. 34 (2015) 69–77. https://doi.org/10.1016/j.sbi.2015.07.006.

[14] J.J. Barr, R. Auro, N. Sam-Soon, S. Kassegne, G. Peters, N. Bonilla, M. Hatay, S. Mourtada, B. Bailey, M. Youle, B. Felts, A. Baljon, J. Nulton, P. Salamon, F. Rohwer, Subdiffusive motion of bacteriophage in mucosal surfaces increases the frequency of bacterial encounters, Proc. Natl. Acad. Sci. U. S. A. 112 (2015) 13675–13680. https://doi.org/10.1073/pnas.1508355112.

[15] J.J. Barr, R. Auro, M. Furlan, K.L. Whiteson, M.L. Erb, J. Pogliano, A. Stotland, R. Wolkowicz, A.S. Cutting, K.S. Doran, P. Salamon, M. Youle, F. Rohwer, Bacteriophage adhering to mucus provide a non-host-derived immunity, Proc. Natl. Acad. Sci. U. S. A. 110 (2013) 10771–10776. https://doi.org/10.1073/pnas.1305923110.

[16] E.S. Frenkel, K. Ribbeck, Salivary Mucins Protect Surfaces from Colonization by Cariogenic Bacteria, Appl. Environ. Microbiol. 81 (2015) 332–338.

https://doi.org/10.1128/aem.02573-14.
[17] N.L. Kavanaugh, A.Q. Zhang, C.J. Nobile, A.D. Johnson, K. Ribbeck, Mucins suppress virulence traits of Candida albicans, MBio. 5 (2014) 1–8. https://doi.org/10.1128/mBio.01911-14.
[18] SM buffer, Cold Spring Harb. Protoc. (2006).
[19] N. Bonilla, J.J. Barr, Phage on tap: A quick and efficient protocol for the preparation of bacteriophage laboratory stocks, Methods Mol. Biol. 1838 (2018) 37–46. https://doi.org/10.1007/978-1-4939-8682-8_4.
[20] E.M. Furst, Particle tracking with Matlab, (n.d.). https://lem.che.udel.edu/wiki/index.php?n=Main.Microrheology.
[21] V. Pelletier, M. Kilfoil, Software Research Tools, Kilfoil Lab, (2007). http://people.umass.edu/kilfoil/downloads.html.
[22] R. Metzler, J.H. Jeon, A.G. Cherstvy, E. Barkai, Anomalous diffusion models and their properties: Non-stationarity, non-ergodicity, and ageing at the centenary of single particle tracking, Phys. Chem. Chem. Phys. 16 (2014) 24128–24164. https://doi.org/10.1039/c4cp03465a.
[23] I.Y. Wong, M.L. Gardel, D.R. Reichman, E.R. Weeks, M.T. Valentine, A.R. Bausch, D.A. Weitz, Anomalous diffusion probes microstructure dynamics of entangled F-actin networks, Phys. Rev. Lett. 92 (2004). https://doi.org/10.1103/PhysRevLett.92.178101.
[24] C.E. Wagner, B.S. Turner, M. Rubinstein, G.H. McKinley, K. Ribbeck, A Rheological Study of the Association and Dynamics of MUC5AC Gels, Biomacromolecules. 18 (2017) 3654–3664. https://doi.org/10.1021/acs.biomac.7b00809.
[25] N.A. Bustos, C.M. Saad-Roy, A.G. Cherstvy, C.E. Wagner, Distributed medium viscosity yields quasi-exponential step-size probability distributions in heterogeneous media, Soft Matter. 18 (2022) 8572–8581. https://doi.org/10.1039/d2sm00952h.
[26] O. Lieleg, I. Vladescu, K. Ribbeck, Characterization of particle translocation through mucin hydrogels, Biophys. J. 98 (2010) 1782–1789. https://doi.org/10.1016/j.bpj.2010.01.012.
[27] R. Metzler, J. Klafter, The random walk's guide to anomalous diffusion: A fractional dynamics approach, Phys. Rep. 339 (2000) 1–77. https://doi.org/10.1016/S0370-1573(00)00070-3.
[28] F. Evers, C. Zunke, R.D.L. Hanes, J. Bewerunge, I. Ladadwa, A. Heuer, S.U. Egelhaaf, Particle dynamics in two-dimensional random-energy landscapes: Experiments and simulations, Phys. Rev. E - Stat. Nonlinear, Soft Matter Phys. 88 (2013) 22125. https://doi.org/10.1103/PhysRevE.88.022125.
[29] R.C. WILLIAMS, D. FRASER, Morphology of the seven T-bacteriophages., J. Bacteriol. 66 (1953) 458–464. https://doi.org/10.1128/jb.66.4.458-464.1953.
[30] O. Lieleg, I. Vladescu, K. Ribbeck, Characterization of particle translocation through mucin hydrogels, Biophys. J. 98 (2010) 1782–1789. https://doi.org/10.1016/j.bpj.2010.01.012.
[31] L.D. Li, T. Crouzier, A. Sarkar, L. Dunphy, J. Han, K. Ribbeck, Spatial configuration and composition of charge modulates transport into a mucin hydrogel barrier, Biophys. J. 105 (2013) 1357–1365. https://doi.org/10.1016/j.bpj.2013.07.050.

3.7 Acknowledgements

This chapter includes work that is being prepared for publication by N.A. Bustos, C. Griffin, C. E. Wagner, K. Ribbeck, and C. Stevens.

Contributions: N.A.B., C.E.W., K.R., and C.S. conceived and designed the SPT experiments. N.A.B., C.G., and C.S. performed and analyzed the SPT experiments. C.S. prepared phage and Sigma mucin. C.E.W., K.R., and C.S. supervised the study. N.B. wrote the text in this chapter and C.S. contributed to the methodology of preparing phage and Sigma mucin.

3.8 Supplementary Materials

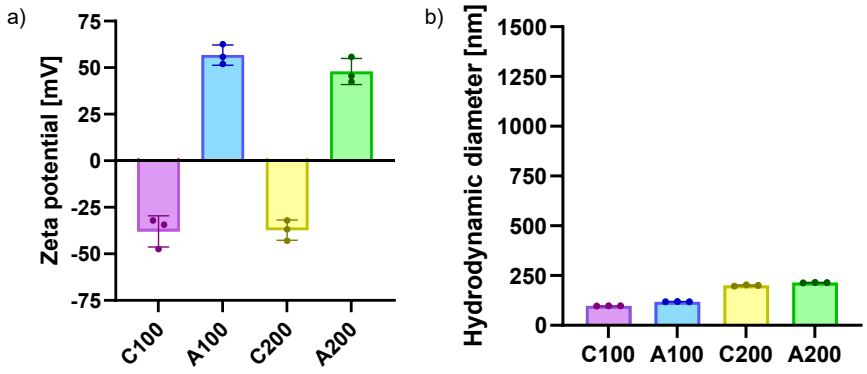

Supplementary Figure S3.1 Size and charge of carboxylated (negatively charged) and aminated (positively charged) nanoparticles (NPs). (a, b) a Zeta potential and **b** hydrodynamic diameter of 100 nm diameter carboxylated NPs, 100 nm diameter aminated NPs, 200 nm diameter carboxylated NPs, and 200 nm diameter aminated NPs in MilliQ water. Measurements were done using a Zetasizer Nano (Malvern Panalytical, Malvern, UK). Each point represents an independent replicate and error bars indicate the standard deviation (n=3).

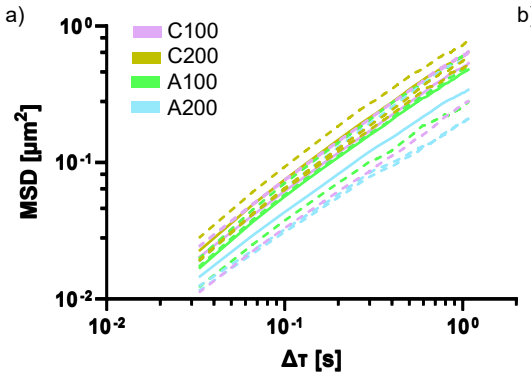

b)

	α
C100	0.99±0.02
C200	0.90±0.07
A100	0.92±0.11
A200	0.99±0.05

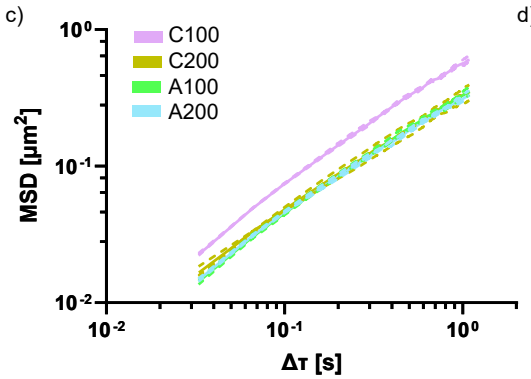

d)

	α
C100	0.99±0.02
C200	0.90±0.07
A100	0.92±0.11
A200	0.99±0.05

Supplementary Figure S3.2 Mean squared displacements (MSDs) and diffusional exponents (α) of nanoparticles in mucin gels. (a, b) a Mean squared displacement (MSD) as a function of lag time ($\Delta\tau$) and **b** summary table of anomalous diffusion exponents α for carboxylated 100 nm (C100) and 200 nm (C200) diameter nanoparticles in 1% Muc2. Dashed lines in **a** denote the ensemble-average MSD of an individual experiment and solid lines denote the average over all experiments. The reported numbers in **b** represent the average±standard deviation. **(c, d) c** Mean squared displacement (MSD) as a function of lag time ($\Delta\tau$) and **d** summary table of anomalous diffusion exponents α for nanoparticles in 1% Muc5AC. Dashed lines in **c** denote the ensemble-average MSD of an individual experiment and solid lines denote the average over all experiments. The reported numbers in **d** represent the average±s.d.

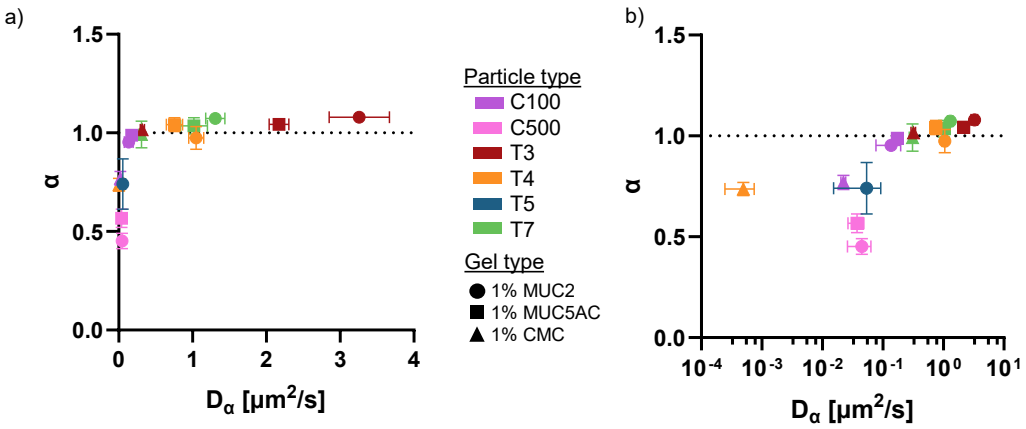

Supplementary Figure S3.3 Diffusion exponent (α) as a function of generalized diffusion coefficient (D_α). The diffusion exponent and generalized diffusion coefficient were determined from a fit of equation 3.4 to the ensemble MSDs of particles in 1% Muc2 (circles), Muc5AC (squares), and CMC (triangles). **(a, b)** Values were plotted on **a** linear-linear plot and **b** log-linear plot. Horizontal and vertical error bars represent the standard deviation of D_α and α, respectively. Three replicate measurements were performed for each particle type in each gel. The dotted line denotes α =1.

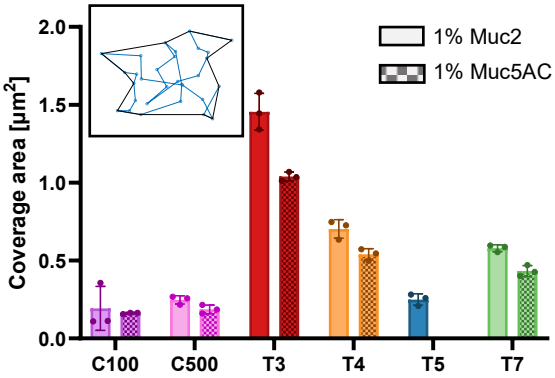

Supplementary Figure S3.4 Phages cover more area in mucus than nanoparticles of comparable size. Median coverage area of phages (T3, T4, T5, and T7), carboxylated 100 nm diameter (C100) and 500 nm diameter nanoparticles (C500). 1% Muc2 is represented by a solid color and 1% Muc5AC is represented by a checker pattern. Each point represents an independent replicate and error bars indicate the standard deviation (n=3).

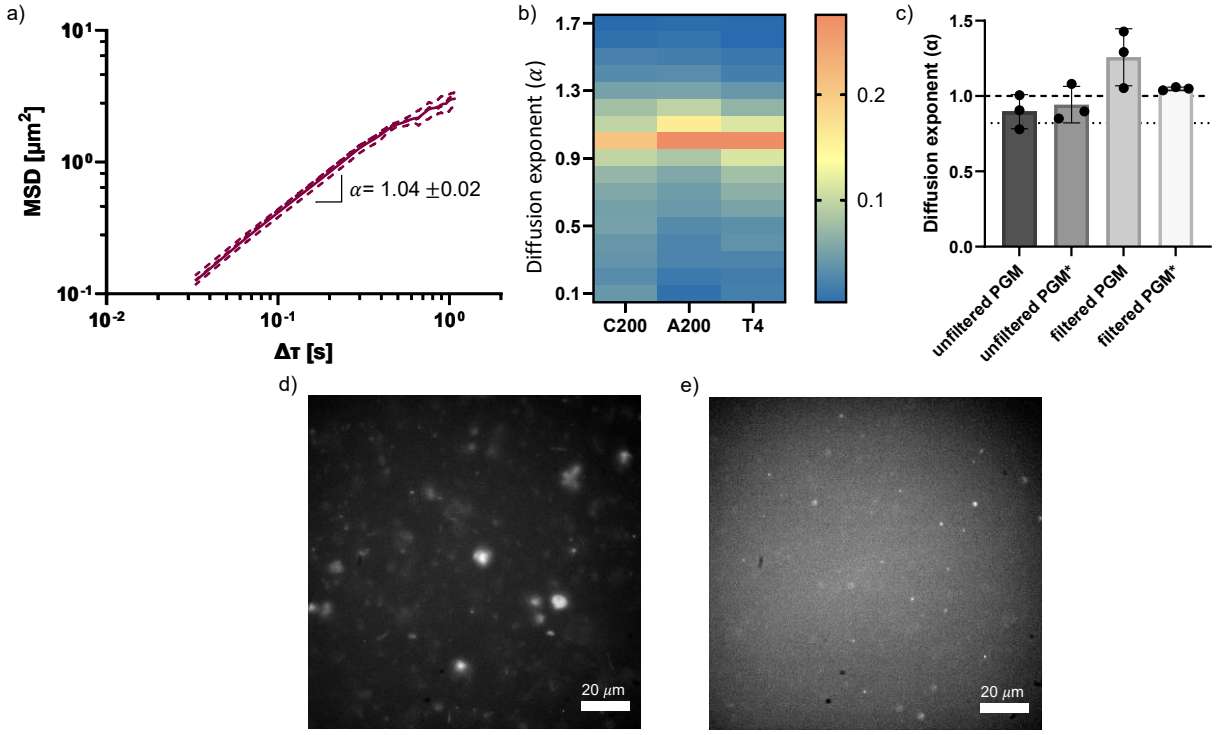

Supplementary Figure S3.5 Diffusion of T4 in 1% porcine gastric mucin (PGM) from Sigma. a Mean squared displacement (MSD) as a function of lag time ($\Delta\tau$) for T4 in 1% PGM solution. Dashed lines denote the ensemble-average MSD of an individual experiment and solid lines denote the average over all experiments. **b** Heatmap histogram of individual diffusional exponents from time-averaged mean squared displacements (TAMSDs) of T4, carboxylated 200 nm diameter particles (C200), and aminated 200 nm diameter particles (A200). The legend indicates the color that corresponds to the proportion of trajectories with a particular diffusional exponent. **c** Diffusion exponent of T4 in different preparations of 1% PGM solutions (e.g., filtered and unfiltered; see Methods). The asterisk indicates post-processing was done on the single particle tracking data (see Methods). Dashed line denotes α =1 and the dotted line denotes α =0.82 in reference to [12]. Each point represents an independent replicate and error bars indicate the standard deviation (n=3). **(d, e)** Microscopy images of T4 suspended in **d** unfiltered and **e** filtered 1% PGM solutions. Fluorescent aggregates in **d** are aggregates of insoluble PGM and phage.

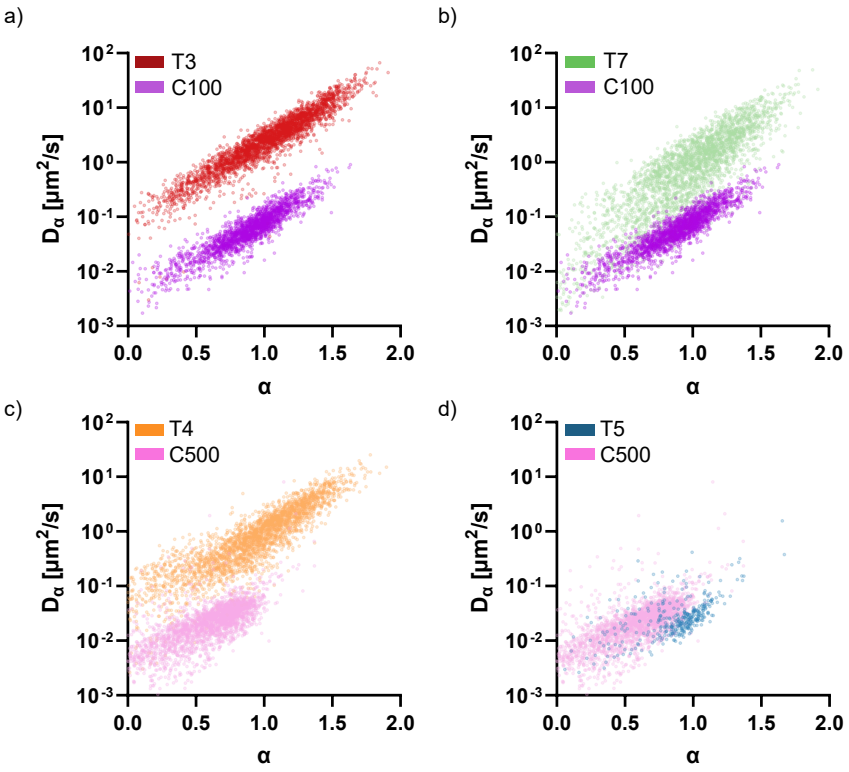

Supplementary Figure S3.6 Particle diffusivities and diffusional exponents of phages and nanoparticles (NPs) in 1% Muc2. (a, b, c, d) Diffusivity (D_α) as a function of diffusional exponent (α) for **a** T3 and carboxylated 100 nm diameter NPs (C100), **b** T7 and C100, **c** T4 and carboxylated 500 nm diameter NPs (C500), and **d** T5 and C500.

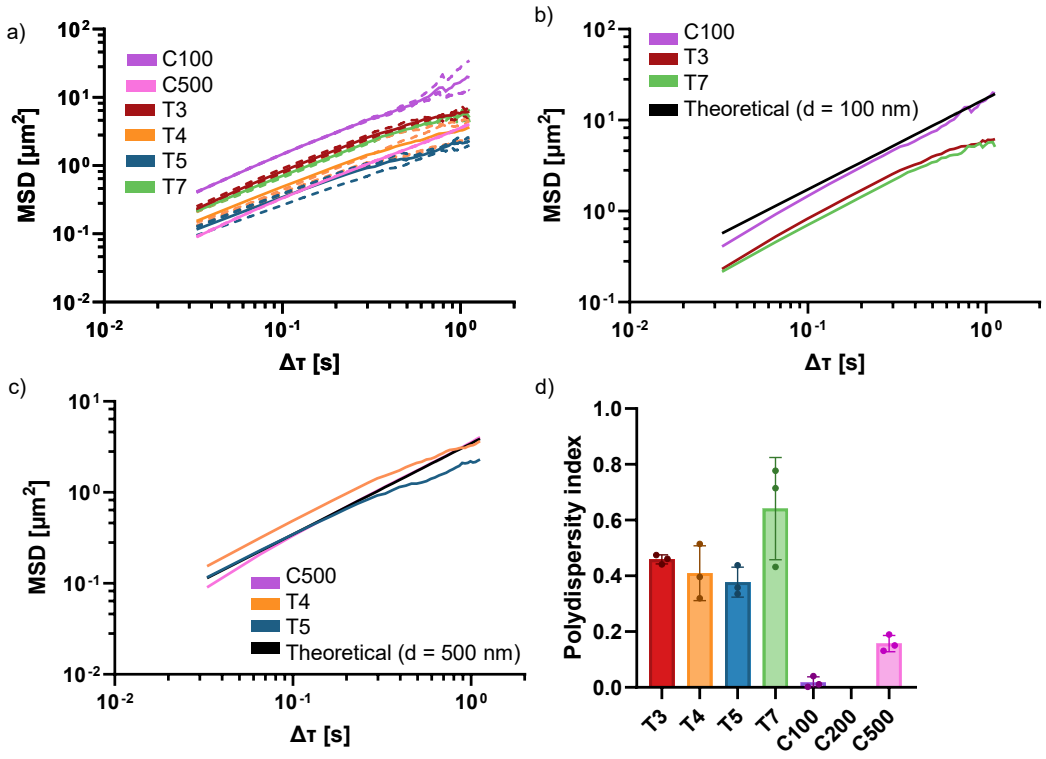

Supplementary Figure S3.7 Diffusion of phage and nanoparticles in SM buffer. a Mean squared displacement (MSD) as a function of lag time ($\Delta\tau$). Dashed lines denote the ensemble-average MSD of an individual experiment and solid lines denote the average over all experiments. **b** MSD as a function of $\Delta\tau$. Black line denotes the theoretical MSD for a spherical particle with diameter (d) of 100 nm in a fluid with viscosity of water at room temperature. Remaining solid lines denote the average over all replicate experiments for carboxylated 100 nm diameter nanoparticle (C100), T3, and T7. **c** MSD as a function of $\Delta\tau$. Black line denotes the theoretical MSD for a spherical particle with diameter (d) of 500 nm in a fluid with viscosity of water (0.001 Pa-s) at room temperature (T = 20 °C). Other solid lines denote the average over all replicate experiments for carboxylated 500 nm diameter nanoparticle (C500), T4, and T5. **d** Polydispersity index reported from Zetasizer Nano (Malvern Panalytical, Malvern, UK).

a)

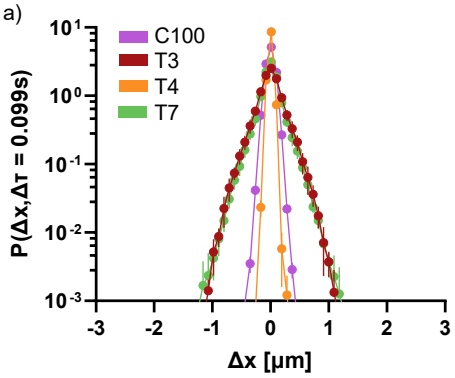

b)

	$\kappa(0.099s)$	α
C100	0.10±0.01	0.77±0.03
T3	0.49±0.11	1.02±0.0
T4	0.28±0.05	0.74±0.03
T5	NA	NA
T7	0.83±0.22	0.99±0.06

Supplementary Figure S3.8 Diffusion of phage in 1% carboxymethylcellulose (CMC). a van Hove correlations (i.e., distribution of all particle step sizes) in the x-direction (Δx) at lag time ($\Delta\tau$) 0.099s for 1% CMC. Each point represents the average of three replicates and the error bars represent the corresponding standard deviation (s.d.). **b** Summary table of non-Gaussian parameters κ and the anomalous diffusion exponents α are presented for different phage and carboxylated 100 nm diameter nanoparticles (C100).

Chapter 4

Experimental instruments and techniques

4.1 Introduction

Rheology is the study of how materials deform or flow in response to stress. Studying materials under shear deformations provides insight into how materials behave in different shear-dominated flows, such as flows experienced in the respiratory tract during a cough or sneeze. Liquid-solid mixtures, such as polymer solutions and biological hydrogels, are a particular class of materials that behave as both a solid and a liquid in response to a deformation; these materials are typically referred to as “viscoelastic”. In addition to shear rheology, extensional rheology, or the response of viscoelastic materials to elongational flow fields, is relevant to physiological flows where biological hydrogels are stretched and atomized, including during the formation of mucosalivary droplets and fragmentation mucus layers. For highly elastic materials, such as solutions with high concentrations of high molecular weight polymers, various methods exist to measure extensional rheology. However, the rheological measurement of weakly viscoelastic fluids and sample-limited fluids poses several challenges. In this chapter, we present a detailed description of experimental instruments and techniques to measure the rheological properties of the materials studied in this thesis; we present relevant theoretical background used for interpreting rheological data and experimental considerations for the fluids and fluid-particle systems tested in **Chapter 5**.

4.2 Shear rheology measurements

Controlled shear drag flows are applied using a rheometer and parallel plate geometries (such as sliding plates, concentric cylinders, cone and plate, and parallel disks), wherein the sample is positioned between two plates: one stationary plate and one moveable plate [1]. In our work, we used a “cone and plate” configuration, where the top plate is a moveable plate and is available with different geometries (e.g., plate radius, cone angle); smaller plates may be preferred for limited sample volumes. However, this impacts the size of the experimental window where data is reliable; the experimental window is affected by several limitations including the instrument’s

low-torque limit and inertial and secondary flow limits. These limitations are often problems for soft, low-viscosity biological fluids that may also have surface active components (e.g., surfactants) that modify the liquid-air interface and thereby obscure the fluid's true shear rheological response [2].

The shear rheological response of fluids tested in **Chapter 5** was measured using 2 common experiments: steady-state shear flow tests and small amplitude oscillatory shear (SAOS) tests. SAOS flow is used to determine the viscoelastic moduli of the sample and steady-state shear flow is used to measure the steady-state viscosity of the sample as a function of shear rate. All shear rheology measurements were performed using a strain-controlled rheometer (ARES-G2, TA instruments, New Castle, DE, USA) and Peltier plate at a constant temperature. For all configurations, the air–sample interface was coated in mineral oil to limit sample evaporation. This coating has been shown not to impact the viscoelastic moduli [3].

4.2.1 Steady state shear rheology

In steady-state (cone-and-plate) shear flow experiments, the top plate and bottom plate are separated by a defined gap. The top plate is rotated at a constant shear rate, generating a stress parallel to the fluid and inducing fluid movement that results in a velocity gradient across the gap. The shear deformation corresponds to a steady state viscosity value associated with the corresponding shear rate. The shear rate is varied to extract a flow curve for viscosity across a range of shear rates. For Newtonian fluids, the relationship between shear rate and viscosity is linear and constant. This is in contrast to non-Newtonian fluids, which can exhibit shear-thinning or shear-thickening behavior [4]. Shear thinning fluids exhibit a decrease in viscosity as the shear rate increases. Many biological fluids, such as blood, respiratory mucus, and cervical mucus display shear-thinning viscosity [5,6]. Depending on the source of the mucus (e.g., saliva, sputum, tears, etc.), both the viscosity at low shear rates and the slope of the viscosity versus shear rate can vary [7]. This can be attributed to the disentanglement, unraveling, and alignment of mucin polymer chains in the flow direction, which are characteristic effects of shear deformation in polymer solutions [4,8].

Measurement of shear rheology over a wide range of shear rates for low-viscosity fluids is challenging because there is a limitation on the lowest torque that can be reliably measured. The low torque limit for shear viscosity is given by [9]

$$\eta_{min} = \frac{FT_{min}}{\dot{\gamma}} \quad 4.1$$

where $\dot{\gamma}$ is the shear rate and F is a geometric factor; for a cone-and-plate setup, $F = \frac{3}{2\pi R^3}$ and for a parallel plate setup, $F = \frac{2}{\pi R^3}$ where R is the geometry radius. The low torque limit, T_{min}, is provided by the manufacture and is 0.1 μN-m for the ARES-G2 rheometer used in this thesis.

At high enough shear rates, high flow velocities can cause secondary flows on top of the primary shear flow due to sample inertia [9, 10]. Cone-and-plate and parallel plate configurations can also have a secondary flow that occurs at a fixed rotational velocity which causes an outward flow at the rotating boundary [9, 11]. The strength of the flow is based on the dimensionless Reynolds number, which describes the relative importance of inertial forces to viscous forces within a fluid flow [12]. Secondary flow increases the measured torque and erroneously increases the measured fluid viscosity giving the appearance of shear-thickening behavior in some cases. The "secondary flow limit" is given by:

$$\eta_{max} = \frac{L^3/R}{Re_{crit}}\rho\dot{\gamma} \quad 4.2$$

with

$$L = \beta R \quad 4.3$$

where β is the angle between the cone and plate and for a parallel plate setup it is the height of the gap, Re_{crit} is a critical Reynolds number, and ρ is the fluid density. Three plates were used for measurements: an 8 mm parallel plate, a 25 mm parallel plate, and a 40 mm 2° cone-and-plate fixture. The height of the gap in the 8 mm parallel plate configuration was 200 μm and for the 25 mm parallel plate was 150 μm. Solutions with limited sample volumes, such as mucin gels, were measured using 8 mm plates whereas samples with larger available volumes such as mucosalivary fluid were measured with a 40 mm plate. Because the measured torque is predicted to depend on the Reynolds number, the critical number Reynolds number in equation 4.2 is based on an error bound on the measured torque relative to the ideal torque. Here, we use a critical Reynolds number of 4 which correspond to a 1% error [9]. In general, we observed that the "secondary flow limit" restricted access to high shear rates ($\gg$ 1000 s^{-1}) for all plate geometries. As a result, a shear rate of 1000 s^{-1} was the highest shear rate investigated in our experiments. From equations 4.1 through 4.3, the geometry of the plate changes the instrument flow limit and hence the range of accessible shear rates.

Several empirical equations have been proposed to describe shear-rate dependent viscosity including models defined by Cross, Carreau, Yasuda, and Bird. The Cross model is a four-parameter constitutive relationship [13,14]:

$$\mu(\dot{\gamma}) = \mu_\infty + \frac{\mu_0 - \mu_\infty}{1+(\lambda\dot{\gamma})^{1-n}}, \quad 4.4$$

where μ is the effective viscosity of the fluid as a function of shear rate, $\dot{\gamma}$, $\mu_\infty$is the infinite shear viscosity, μ_0 is the zero-shear viscosity, λ is a constant with dimensions of time, and n is the power-law index. This model has fixed, non-zero viscosity at zero shear rate and infinite shear rate limits. The Carreau model is a three parameter model [15]:

$$\mu(\dot{\gamma}) = \frac{\mu_0}{(1+(\lambda\dot{\gamma})^2)^{1-n/2}}. \quad 4.5$$

In contrast with the Cross model, the Carreau model provides a fixed viscosity at zero shear rate, but has a zero viscosity in the infinite shear rate limit. Yasuda modified the Carreau model and introduced a fourth free parameter by substituting the constant number 2 in the Carreau model with a as a variable to represent better the transition from the low shear region to the power-law region. This formulation is as follows [16]:

$$\mu(\dot{\gamma}) = \frac{\mu_0}{(1+(\lambda\dot{\gamma})^a)^{1-n/a}}, \quad 4.6$$

Bird [4] defined the 'Carreau-Yasuda' model which is a five-parameter model and appears as a variation of Carreau and Yasuda's models but includes the infinite shear rate viscosity parameter. This model is of the form:

$$\mu(\dot{\gamma}) = \frac{\mu_0 - \mu_\infty}{(1+(\lambda\dot{\gamma})^a)^{1-n/a}}, \quad 4.7$$

The models differ in the number of fitting parameters and some models have been shown to more accurately describe the rheological response of specific classes of complex fluids. The Carreau and Carreau-Yasuda models were utilized in several studies to fit data from rheology experiments involving mucus [17,18] and other biopolymer solutions, including solutions of carboxymethylcellulose (CMC) [19], a common ingredient in artificial saliva. In **Chapter 5**, we use the Carreau model to extract a characteristic viscosity of polymer solutions because of its fit to the experimental data and its relatively small number of fitting parameters.

4.2.2 Small amplitude oscillatory shear rheology

SAOS flows apply sinusoidal deformations to study the linear viscoelastic response of materials by decomposing the material stress into frequency-dependent components corresponding to a storage modulus (G'(ω)) and loss modulus (G"(ω)). The storage or elastic modulus corresponds to the solid-like character of the material, while the loss or viscous modulus corresponds to the liquid-like contributions to the overall material behavior. For polymer solutions, a typical SAOS response shows that for sufficiently slow deformations, the material's response is liquid-like (G">G') and beyond this, at high enough frequencies, the material responds as solid-like (G'>G").

Time oscillation measurements were first conducted to determine whether any of the materials underwent any structural changes over a certain period of time (e.g., over the time of strain sweep or frequency tests). To perform the SAOS experiments in this thesis, the top plate is oscillated with a time-varying strain described by

$$\gamma(t) = \gamma_0 \sin(\omega t), \tag{4.4}$$

where γ_0 is the strain amplitude and ω is the oscillation frequency. Because these experiments probe the linear viscoelastic regime of the material, strain sweep experiments were done for all materials prior to frequency sweep experiments; in strain sweep experiments, the frequency is kept constant and the largest strain value ($\gamma_{0,c}$) for which the material responds linearly is determined. Following the determination of $\gamma_{0,c}$, any strain amplitude less than or equal to this critical value is used for frequency sweep experiments and the frequency is varied. For weakly viscoelastic materials, it is suggested to use the largest value possible value of γ_0 in order to maintain the resulting torque above the minimum torque limit of the rheometer.

The minimum storage or loss modulus is related to the minimum torque limit by [9]

$$G_{min} = \frac{FT_{min}}{\gamma_0}, \tag{4.5}$$

where F is a geometric factor, for a cone-and-plate setup, $F = \frac{3}{2\pi R^3}$ and for a parallel plate setup, $F = \frac{2}{\pi R^3}$, and R is the geometry radius. At high frequencies, low viscosity materials have a greater propensity for inertial and secondary flow effects. An approximate limit of the viscoelastic moduli scales as [3,9]

$$|G^*| \sim \rho\omega^2 H^2, \tag{4.6}$$

where ρ is the fluid density, ω is the frequency, and H is the geometry gap; this scaling approximates the "sample inertia limit".

4.3 Elongational rheology measurements

In addition to mechanical properties under shear, polymer macromolecules can undergo stretching and orientation in shear-free extensional flows. For example, for mucus, extensional rheological properties are essential for physiological processes such as mucociliary clearance. Commonly, a commercially available technique, the Capillary Break-up Extensional Rheometer (CaBER), is used to establish an extensional flow by applying a discrete step-strain to a sample between two parallel plates; the primary measurement is the neck radius (the narrowest point) of the thinning liquid bridge formed which is used to extract a characteristic extensional relaxation time (λ) associated with the material [20]. However, often an experimental challenge of low viscosity ($\eta < 20$ mPa-s), low elasticity fluids ($\lambda <$1 ms), including aqueous polymer solutions, is that the liquid pinches off before complete plate separation (~50 ms) [20, 21]. This makes it difficult to capture the elastocapillary regime, the regime where elastic and capillary forces are in balance and relaxation time is extracted [20,21]. Beyond the limitations associated with plate separation, inertial effects can also be worse for low viscosity fluids and affect measurement because the liquid thread can undergo oscillations [20] or the beads-on-string morphology [22] which may make it difficult to reliably measure relaxation time.

Other specialized instrumentation has been developed for low viscosity and low relaxation time fluids, for example: 1) dripping [23], where pinch-off results from a balance between gravitational drainage and capillary forces, 2) jetting [24,25], where a capillary instability develops on a fluid jet and analysis is based on the understanding of the nonlinear fluid dynamics underlying the jetting process, and 3) slow retraction method (SRM) [26], a modified CaBER protocol. The initial step-strain required in CaBER and SRM measurements can disrupt the fluid microstructure, thus affecting the observed extensional rheology behavior [27]. Although the jetting-based rheometry technique, called the Rayleigh Ohnesorge Jetting Extension Rheometer (ROJER) enables measurement of low relaxation times, the method requires high flow rates and large volumes of liquid; pre-shearing before filament stretching may also breakdown the solution's microstructure [28,29]. As an alternative to jetting, we built a climate-monitored aerosolization chamber for visualizing the aerosolization of weakly viscoelastic biopolymer solutions to study droplet break up (**Figure 4.1**). Briefly, the experimental setup comprises a rectangular chamber constructed from acrylic sheets, housing several temperature and humidity sensors. The chamber's conditions were continuously monitored in real-time during the experiments, encompassing the period prior to spraying, the

spraying process itself, and the post-spray phase. Sprays were released into the chamber via a circular inlet. Due to restricted sample volumes for reconstituted mucin gels, we modified a nozzle head to fit 2mL centrifuge tubes and secured it using parafilm. The spraying processed was recorded using a high-speed camera, positioned at a distance from the spray inlet. To restore the chamber's climate to its pre-spray state (room conditions, $T \approx 21$ ºC and $RH \approx 30\%$), any remaining moisture was absorbed using silica particles. This was enhanced by a vacuum line connected to a valve on the side of the chamber and the interior of the chamber was cleaned between experiments. We characterized extensional properties separately using dripping methods that are applicable to small sample volumes.

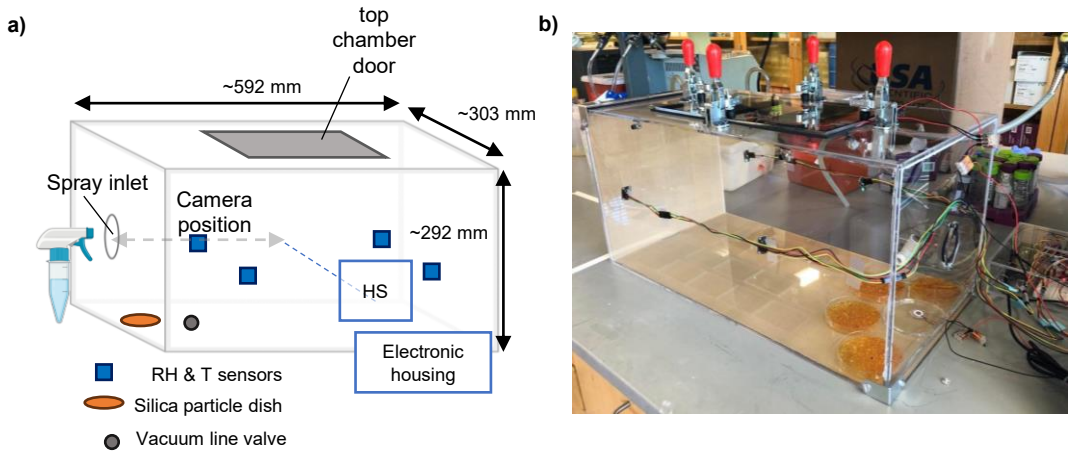

Figure 4.1 Climate-monitored aerosolization chamber. a Detailed schematic of experimental chamber. The detailed schematic shows the placement of four humidity and temperature sensors (RH & T sensors) inside the chamber, which were connected to an electronic housing on the outside of the chamber. The electronic housing contained an Arduino Mega 2560 to record the humidity and temperature reading in real time. Sprays were released into the chamber via a circular opening (noted as spray inlet in the schematic) and were imaged with a high-speed camera (HS) placed at a distance away from the inlet. Silica particles were used after spray tests to absorb residual moisture from sprays in order to return chamber conditions to room conditions (T ≈ 21 ºC and RH ≈ 30%). After sprays, tubing connected to a vacuum line was also attached to a valve on the side of the box to expedite removal of residual moisture from sprays. A panel at the top of the chamber gave access to the interior of chamber. **b** Image of experimental chamber on lab bench.

Dinic et al. [30] developed a dripping protocol, where a pendant drop drips onto a substrate and the thinning is analyzed from experimental images taken with a high speed camera. The dripping-onto-substrate (DoS) method is preferable over dripping alone where the neck location varies as the drop descends; with a fixed neck location, the high-speed camera can be placed as close as possible to the liquid thread in order to maximize image resolution. Apart from the relaxation time, the thread lifetime is also of interest in our work because it has been reported to systematically vary with particle size and particle concentration [31,32]. The aspect ratio, denoting the relationship between the height of the gap between the nozzle and the substrate, and the diameter of the nozzle, can be varied in the DoS setup. Consequently,

this impacts the thread lifetime: a wider gap results in shorter thread lifetimes, while a narrower gap leads to longer lifetimes. To maintain consistency in our experiments, we maintained a constant aspect ratio. This approach allowed us to explore the impact of nanoparticles, serving as surrogates for virions, on thinning dynamics. Notably, prior work by Dinic et al. identified an optimal aspect ratio of 3 [30,33]. For our experiments, we constructed a similar setup in the lab using a lab jack, lab stand, and clamp to secure a blunt needle and hold a microscope slide in place (**Figure 4.2**). The thinning of thread was recorded using a high-speed camera, while an LED lamp provided backlighting to illuminate the filament thread from behind. This illumination significantly improved the visibility of the filament thread's contour shape, a critical factor for extracting the neck radius of the thinning filament over time.

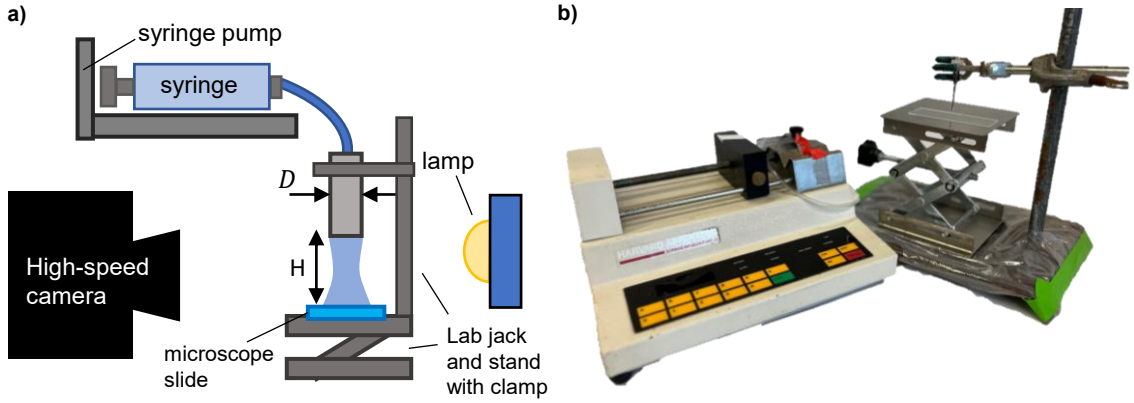

Figure 4.2 Lab-made dripping-onto-substrate (DoS) setup. a Schematic of DoS setup. The DoS setup was built using a lab jack and lab stand with clamp. The clamp held a blunt needle of diameter D in place, which was connected to tubing and a syringe. A syringe pump was used to push fluid through the needle, enabling controlled dripping on a microscope slide. The height (H) was adjusted by positioning the clamp to achieve an aspect ratio (H/D) of approximately 3. A high-speed camera was positioned in alignment with an LED lamp, with the needle positioned between the camera and the backlighting source. **b** Image of lab-made DoS setup.

Upon contact with the solid substrate, the liquid thread initiates a thinning process driven by various forces (including viscous, elastic, and inertial forces) that counteract capillary effects. This process continues until the thread pinches off completely. Initially, the neck undergoes a Newtonian regime that exhibits self-similar thinning in which inertial or viscous effects balance capillary effects; these regimes are referred to as inertiocapillary (IC) or viscocapillary (VC).

Depending on the relative importance of viscous and inertial effects, either the IC or VC regime will be observed; the balance between viscous and inertial effects is described by the dimensionless number known as the Ohnesorge number (Oh) which is a ratio of the viscous timescale (t_V) and Rayleigh timescale (t_R). The Oh number is given by [34]:

$$\text{Oh} = \frac{t_V}{t_R} = \frac{\mu R/\sigma}{\left(\frac{\rho R^3}{\sigma}\right)^{1/2}} = \frac{\mu}{(\rho\sigma R)^{1/2}}, \qquad 4.7$$

where μ is the fluid viscosity, R is a characteristic length scale, σ is the fluid surface tension, and ρ is fluid density. When Oh>1, the VC regime is observed and when Oh<1, the IC response is observed. The initial regime is followed by an elastocapillary regime and then terminal visco-elastocapillary regime due to finite extensibility effects.

4.4 Surface tension measurements

Surface tension is a phenomenon that results from the difference in energy between molecules at a fluid interface when compared to the bulk. There are various techniques to measure interfacial tension with differences in capabilities and limitations including, Wilhelmy plate, maximum bubble pressure, spinning drop, Du Nouy Ring, Capillary rise, and Pendant drop [35]. In terms of instrumentation, the simplest and most versatile method is the pendant drop method, which is suitable for surfactant solutions or fluids with surface-active molecules (e.g., polyethylene oxide solutions [36] and mucus [37]) [38]. In other methods like Wilhelmy Plate, Du Noüy Ring, and sessile drop, the presence of surface-active molecules or impurities may alter the wetting properties of the plate surface or ring. This effect is attributed to the adsorption of surface-active molecules to liquid-solid interfaces in addition to their adsorption to liquid-liquid interfaces [39]. As a result, this may alter measurement conditions and be a possible source of error [40]. While these effects can be eliminated by using rings or plates designed to eliminate or minimize this adsorption effect, practical implementation can be challenging due to the limited availability of ring and plates of different materials [38].

In this work, we employ the pendant drop method, wherein the surface tension is determined from the shape of a pendant drop deformed by gravity; broadly, the drop profile is extracted from an experimental image, and the Young-Laplace equation (equation 4.8) is iteratively solved to determine the best fit parameters [35]. Two parameters of the pendant drop that are first experimentally determined are the equatorial diameter D and the diameter d at a

distance D from the bottom of the drop. These known parameters are then applied to the Young-Laplace equation:

$$\gamma = \frac{\Delta\rho g D^2}{H}, \qquad 4.8$$

where $\Delta\rho$ is the difference between the pendant drop fluid density and the fluid density of the surrounding liquid (in this case, air density), g is gravity, and H is a shape dependent factor that depends on the value of a “shape factor” defined by d/D.

In the preparation of nanoparticles for SPT, the nanoparticle solution is diluted 1:12,000 (nanoparticle: mucin solution) which significantly dilutes the surfactant solution that nanoparticles are suspended in. In contrast, in **Chapter 5**, where we apply the abovementioned rheological methods, the concentration of nanoparticles is varied between 0.001% and 0.1% wt concentrations. As a result, this also varies the amount of surfactant present in the solution which we found to have non-negligible effects on the surface tension of buffer. Therefore, in order to assess the influence of nanoparticles independent of the effect of surfactant molecules, we used centrifugation to remove the aqueous supernatant part of the solution from the solid particle content (described in the methods of **Chapter 5**).

4.5 References

[1] C.W. Macosko, Rheology: Principles, Measurements, and Applications, 1994.

[2] V. Sharma, A. Jaishankar, Y.C. Wang, G.H. McKinley, Rheology of globular proteins: Apparent yield stress, high shear rate viscosity and interfacial viscoelasticity of bovine serum albumin solutions, Soft Matter. 7 (2011) 5150–5160. https://doi.org/10.1039/c0sm01312a.

[3] C.E. Wagner, Micro- and macro-rheological studies of the structure and association dynamics of biopolymer gels, PhD Thesis. (2018).

[4] R.B. Bird, R.C. Armstrong, O. Hassager, Dynamics of Polymeric Liquids, Fluid Mechanics (Volume 1), Wiley and Sons, 1987.

[5] S.K. Lai, Y.Y. Wang, D. Wirtz, J. Hanes, Micro- and macrorheology of mucus, Adv. Drug Deliv. Rev. 61 (2009) 86–100. https://doi.org/10.1016/j.addr.2008.09.012.

[6] R.A. Cone, Mucus, in: Mucosal Immunol., 2005: pp. 49–72.

[7] D.B. Yeates, B.G. J., L.B. Wong, Physicochemical properties of mucus and its propulsion, in: Lung Sci. Found., Lippincott-Raven Publishers, Philadelphia, 1997.

[8] R.G. Larson, The structure and rheology of complex fluids, Oxford University Press, New

York, 1999.

[9] R.H. Ewoldt, M.T. Johnston, L.M. Caretta, Experimental challenges of shear rheology: how to avoid bad data, Complex Fluids Biol. Syst. 7 (2015) 3866–3871. https://doi.org/10.1002/app.

[10] R.G. Larson, Instabilities in viscoelastic flows, Rheol. Acta. 31 (1992) 213–263. https://doi.org/10.1007/BF00366504.

[11] H.P. Sdougos, S.R. Bussolari, C.F. Dewey, Secondary floww and turbulence in a cone-and-plate device, J. Fluid Mech. 138 (1984) 379–404.

[12] G.H. McKinley, Dimensionless Groups For Understanding Free Surface Flows of Complex Fluids, SOR Rheol. Bull. (2005) 1–8. http://citeseerx.ist.psu.edu/viewdoc/download?doi=10.1.1.516.6467&rep=rep1&type=pdf.

[13] M.M. Cross, Rheology of non-Newtonian fluids: A new flow equation for pseudoplastic systems, J. Colloid Sci. 20 (1965) 417–437. https://doi.org/10.1016/0095-8522(65)90022-X.

[14] M.M. Cross, Relation between viscoelasticity and shear-thinning behaviour in liquids, Rheol. Acta. 18 (1979) 609–614. https://doi.org/10.1007/BF01520357.

[15] A. Jaishankar, G.H. McKinley, A fractional K-BKZ constitutive formulation for describing the nonlinear rheology of multiscale complex fluids, J. Rheol. (N. Y. N. Y). 58 (2014) 1751–1788. https://doi.org/10.1122/1.4892114.

[16] K. Yasuda, Investigation of the analogies between viscometric and linear viscoelastic properties of polystyrene fluids, 1979.

[17] D. Schieppati, R. Germon, F. Galli, M.G. Rigamonti, M. Stucchi, D.C. Boffito, Influence of frequency and amplitude on the mucus viscoelasticity of the novel mechano-acoustic Frequencer™, Respir. Med. 153 (2019) 52–59. https://doi.org/10.1016/j.rmed.2019.04.011.

[18] A. Aghakhani, A. Pena-Francesch, U. Bozuyuk, H. Cetin, P. Wrede, M. Sitti, High shear rate propulsion of acoustic microrobots in complex biological fluids, Sci. Adv. 8 (2022) 1–12. https://doi.org/10.1126/sciadv.abm5126.

[19] C.G. Lopez, R.H. Colby, J.T. Cabral, Electrostatic and Hydrophobic Interactions in NaCMC Aqueous Solutions: Effect of Degree of Substitution, Macromolecules. 51 (2018) 3165–3175. https://doi.org/10.1021/acs.macromol.8b00178.

[20] L.E. Rodd, T.P. Scott, J.J. Cooper-White, G.H. McKinley, Capillary break-up rheometry of low-viscosity elastic fluids, Appl. Rheol. 15 (2005) 12–27. https://doi.org/10.3933/ApplRheol-15-12.

[21] J. Dinic, M. Biagioli, V. Sharma, Pinch-off dynamics and extensional relaxation times of intrinsically semi-dilute polymer solutions characterized by dripping-onto-substrate rheometry, J. Polym. Sci. Part B Polym. Phys. 55 (2017) 1692–1704. https://doi.org/10.1002/polb.24388.

[22] P.P. Bhat, S. Appathurai, M.T. Harris, M. Pasquali, G.H. McKinley, O.A. Basaran, Formation of beads-on-a-string structures during break-up of viscoelastic filaments, Nat. Phys. 6 (2010) 625–631. https://doi.org/10.1038/nphys1682.

[23] J.J. Cooper-White, J.E. Fagan, V. Tirtaatmadja, D.R. Lester, D. V. Boger, Drop formation dynamics of constant low-viscosity, elastic fluids, J. Nonnewton. Fluid Mech. 106 (2002) 29–59. https://doi.org/10.1016/S0377-0257(02)00084-8.

[24] V. Sharma, S.J. Haward, J. Serdy, B. Keshavarz, A. Soderlund, P. Threlfall-Holmes, G.H. McKinley, The rheology of aqueous solutions of ethyl hydroxy-ethyl cellulose (EHEC) and its hydrophobically modified analogue (hmEHEC): Extensional flow response in capillary break-up, jetting (ROJER) and in a cross-slot extensional rheometer, Soft Matter. 11 (2015) 3251–3270. https://doi.org/10.1039/c4sm01661k.

[25] B. Keshavarz, V. Sharma, E.C. Houze, M.R. Koerner, J.R. Moore, P.M. Cotts, P. Threlfall-Holmes, G.H. McKinley, Studying the effects of elongational properties on atomization of weakly viscoelastic solutions using Rayleigh Ohnesorge Jetting Extensional Rheometry (ROJER), J. Nonnewton. Fluid Mech. 222 (2015) 171–189. https://doi.org/10.1016/j.jnnfm.2014.11.004.

[26] L. Campo-Deaño, C. Clasen, The slow retraction method (SRM) for the determination of ultra-short relaxation times in capillary breakup extensional rheometry experiments, J. Nonnewton. Fluid Mech. 165 (2010) 1688–1699. https://doi.org/10.1016/j.jnnfm.2010.09.007.

[27] E. Miller, C. Clasen, J.P. Rothstein, The effect of step-stretch parameters on capillary breakup extensional rheology (CaBER) measurements, Rheol. Acta. 48 (2009) 625–639. https://doi.org/10.1007/s00397-009-0357-9.

[28] A. Bhardwaj, D. Richter, M. Chellamuthu, J.P. Rothstein, The effect of pre-shear on the extensional rheology of wormlike micelle solutions, Rheol. Acta. 46 (2007) 861–875. https://doi.org/10.1007/s00397-007-0168-9.

[29] M. Rodríguez-Hakim, L. Räz, J. Vermant, Variations in human saliva viscoelasticity affect aerosolization propensity, Soft Matter. 18 (2022) 2528–2540. https://doi.org/10.1039/d1sm01581h.

[30] J. Dinic, Y. Zhang, L.N. Jimenez, V. Sharma, Extensional Relaxation Times of Dilute, Aqueous Polymer Solutions, (2015). https://doi.org/10.1021/acsmacrolett.5b00393.

[31] R.J. Furbank, J.F. Morris, An experimental study of particle effects on drop formation, Phys. Fluids. 16 (2004) 1777–1790. https://doi.org/10.1063/1.1691034.

[32] M.S. van Deen, T. Bertrand, N. Vu, D. Quéré, E. Clément, A. Lindner, Particles accelerate the detachment of viscous liquids, Rheol. Acta. 52 (2013) 403–412. https://doi.org/10.1007/s00397-013-0691-9.

[33] J. Dinic, V. Sharma, Macromolecular relaxation, strain, and extensibility determine elastocapillary thinning and extensional viscosity of polymer solutions, Proc. Natl. Acad. Sci. U. S. A. 116 (2019) 8766–8774. https://doi.org/10.1073/pnas.1820277116.

[34] G.H. McKinley, M. Renardy, Wolfgang von Ohnesorge, Phys. Fluids. 23 (2011). https://doi.org/10.1063/1.3663616.

[35] J.D. Berry, M.J. Neeson, R.R. Dagastine, D.Y.C. Chan, R.F. Tabor, Measurement of surface and interfacial tension using pendant drop tensiometry, J. Colloid Interface Sci. 454 (2015) 226–237. https://doi.org/10.1016/j.jcis.2015.05.012.

[36] B.H. Cao, M.W. Kim, Molecular weight dependence of the surface tension of aqueous poly(ethylene oxide) solutions, Faraday Discuss. 98 (1994) 245–252.

https://doi.org/10.1039/FD9949800245.

[37] S. Girod, J.M. Zahm, C. Plotkowski, G. Beck, E. Puchelle, Role of the physicochemical properties of mucus in the protection of the respiratory epithelium, Eur. Respir. J. 5 (1992) 477–487.

[38] J. Drelich, Measurement of Interfacial Tension in Fluid-Fluid Systems, Encycl. Surf. Colloid Sci. (2002) 3152–3166. http://www.informaworld.com/10.1081/E-ESCS-120000636.

[39] F. Staniscia, H. V. Guzman, M. Kanduč, Tuning Contact Angles of Aqueous Droplets on Hydrophilic and Hydrophobic Surfaces by Surfactants, J. Phys. Chem. B. 126 (2022) 3374–3384. https://doi.org/10.1021/acs.jpcb.2c01599.

[40] CR, Technical Note. Rings are for fingers, plates are for surface tension, Krüss Tech. Note. (2004). https://www.kruss.de/services/education-%0Ahttps://www.kruss-scientific.com/fileadmin/user_upload/website/literature/kruss-tn308-en.pdf.

Chapter 5

Mucins modulate the fate of respiratory droplets

5.1 Abstract

The biophysics of transmission remain a critically understudied aspect of infectious diseases, yet an important role for mucus is becoming increasingly apparent. Here, we investigate the effect of mucins, the primary solid component of mucus, and viral-sized particles on mucus breakup and droplet formation. Specifically, we report the shear, extensional rheology, and surface tension of mucin gels as we all as other model biopolymer solutions, and correlate these properties with the spray behavior of the solutions. We record the sprays using high-speed imaging and a stain assay to quantify key features of fragmentation dynamics including droplet size and spray speed as well as spray spatial patterns. Consistent with previous studies, we find that biopolymers such as mucin modulate the size and spread of sprayed droplets, particularly by increasing fluid elasticity. Critically, we observe that the presence of nanoparticles, which we use as surrogates for viruses, modifies droplet size distributions in a charge-dependent manner, with important implications for disease transmission. Overall, an understanding of the impact of mucin and pathogen load on the breakup of mucus outside of the body is critical to several aspects: designing mitigation strategies, developing cross-scale disease models, and bridging dynamics across in-host and population-level length scales.

5.2 Introduction

A critical objective when a new respiratory infectious disease emerges is to determine its primary route of transmission, as this guides public health recommendations aimed at controlling and mitigating the spread of disease. Yet, the complex biophysics of this process have resulted in it being understudied and frequently oversimplified when incorporated into models for population-level disease spread [1]. Infectious respiratory diseases often involve an

accumulation of virus particles in the mucus coating the epithelial surfaces of the mouth and lungs. In the respiratory tract, mucus not only provides the ‘first line of defense’ against inhaled pathogens but it is also the site where high shear forces can be generated to expel mucus [2]. When infected individuals cough or sneeze, mucus is emitted and breaks into droplets of different sizes bearing virus particles [3]. The distribution of droplet sizes determines the fate of the droplets. Large droplets may either deposit directly into the respiratory tract of a susceptible host, or settle on surfaces to be taken up by direct contact (also referred to as fomites) [4]. However, there is increasing evidence that many respiratory infections are spread by aerosols, i.e. small droplets containing viral particles that stay suspended in the air for extended periods of time [4]. Viruses in small aerosol droplets are believed to preferentially be able to infect the deep airways of the lower respiratory tract, which is associated with more pathogenic infections [5]. In this way, mucus’ droplet size distribution influences the transmission routes and spread of respiratory disease. Understanding the breakup and dispersal of mucus droplets upon emission is therefore critical for fighting the spread of illness.

Mucus is known to modify viral dynamics both within host and external to the host. In the host, mucosal barriers modulate the transport of biological and synthetic particles including viruses [6–9] (**Figure 5.1a**). It is thought that mucins, polymerized chains of densely glycosylated and negatively charged proteins [10,11], in the body function as potential site receptor “decoys” to certain pathogens or as physical barriers limiting their progression and to some degree determining their ability to infect [12,13]. Externally to hosts (**Figure 5.1b**), the presence of mucus components in droplets has been shown to modulate viral survival [14,15], yet key questions remain unanswered in this area. For instance, it is well known that the presence of polymers strongly impacts the dynamics of fragmentation and final size distribution of fluids [16–19], however the influence of mucins on droplet formation of mucus has been less studied. Droplet formation of sprayed fluids is known to be governed by fluid properties including shear and extensional rheology and surface tension [20]. In the case of mucus, these properties depend strongly on the composition of mucus. While mucus is predominantly water (constituting ≥ 95% of its composition), the small contribution of mucins (up to 2% in the airways [21]) plays a crucial role in shaping the viscoelastic and gel-like properties of mucus [22,23]. Mucin gels reconstituted from lab-purified mucin have been shown to be a well-controlled and reproducible mucus model system that can emulate properties of native mucus in specific cases [24]. Yet, their scientific application to study processes such as mucociliary clearance or mucus breakup has been limited to date.

In addition to mucins, the presence of viruses themselves, which typically range from tens to hundreds of nanometers in size and feature biochemically complex surfaces with alternating positive and negative charges, may also impact fragmentation dynamics. Prior work has found that adding large, non-colloidal particles to Newtonian liquids during fragmentation modifies the timing of droplet pinch-off, and may alter the number and size of generated satellite droplets [25,26]. Yoo et al. found that adding spherical particles 2 μm in size to dilute polymer solutions generally increased the size of droplets during jetting experiments, which they attributed to changes in fluid viscosity [27]. Although they did not evaluate droplet breakup, Han et al. studied the effect of adding rod shaped particles 400-1500nm in length to dilute polymer solutions and found that the extensional viscosity of the suspension decreased with increasing particle volume fraction [28]. These studies and the known ability of viruses to interact with mucin molecules [29], suggest that charged nanoparticles may alter the physical properties and spray behavior of mucin gels.

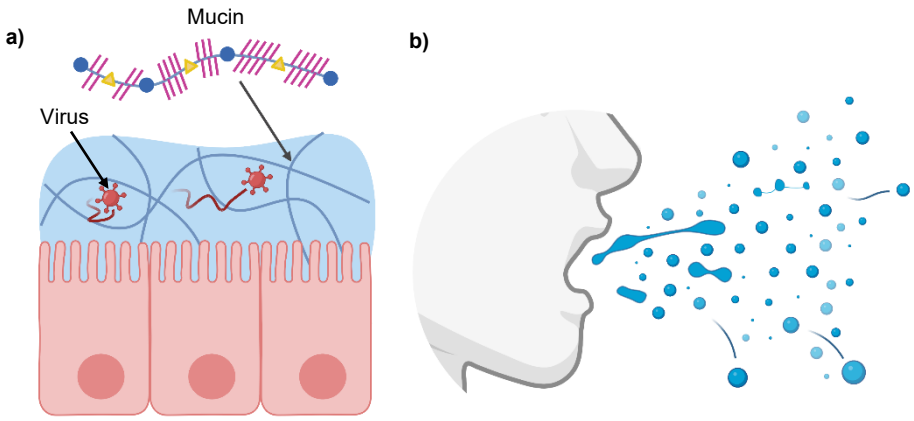

Figure 5.1 Mucin gives mucus its bioactive and viscoelastic properties. a Illustration of mucins forming the mucus layer lining epithelium and interacting with viruses. **b** Illustration of mucus breakup following a violent exhalation; mucus forms a range of droplet sizes and stretched fluid ligaments that may remain suspended in the air, settle onto nearby surfaces, or be introduced into another individual's mucosa.

We hypothesize that the fluid properties and spray behavior of mucus and model biopolymer solutions is controlled by the fluid composition. To test this hypothesis, we investigated the shear and extensional rheology and surface tension of biopolymer solutions and mucosalivary fluid. We correlated fluid properties with measurements of sprays of biopolymer solutions performed with high-speed imaging and a stain assay, and find that polymer elasticity strongly influences the spray characteristics. We further demonstrate that the

addition of nanoparticles to mucin gels alters their surface tension and elastic properties in a charge-dependent manner and, as a result, the size and spread of sprayed droplets in a unique way compared to other model biopolymer systems. Collectively, the results demonstrate the importance of mucins and particles in the formation, size distribution, and dispersal of mucus droplets. An improved understanding in the breakup and dispersal of respiratory droplets is expected to enable improved disease transmission models, guide public health recommendations, and ultimately mitigate the spread and severity of infectious disease.

5.3 Results

5.3.1 Bulk rheology and surface tension

We first conducted a range of rheological tests (**Figure 5.2a**) in order to establish how bulk physical properties contribute to the size and spatial dispersion of droplets from sprays. Specifically, we measured the viscosity, relaxation time, and surface tension of mucus polymer models and mucosalivary fluid from 3 to 5 donors. To evaluate the viscosity of our samples, we performed steady shear measurements across a range of shear rates using an ARES-G2 rheometer. Solutions with limited sample volumes such as Muc5AC mucin gels were measured using 8 mm plates, whereas samples with larger available volumes such as mucosalivary fluid were measured with a 40 mm plate. Viscosity as a function of shear rate for Muc5AC gels with different mucin concentrations and mucosalivary fluid from 5 donors (inset) are plotted in **Figure 5.3a**. The plots show that the viscosity decreases with increasing shear rate, a phenomenon known as shear thinning. Shear thinning fluids can be described by the viscosity in the limit of low shear rates, called the zero-shear viscosity, η_0, and the rate of shear thinning, captured by a power law index, n. For shear thinning fluids, the range of n lies between 0 and 1, with n=1 corresponding to Newtonian fluids; lower n values indicate a greater degree of shear thinning behavior. Data that exhibited shear thinning were fit to the Carreau model for all solutions (see Methods) to extract η_0 and n. For samples that did not exhibit shear thinning (e.g., buffer and Sigma mucin (**Supplementary Figure S5.1a**)), an average over all viscosity values was taken as the zero-shear rate viscosity. The polymer concentration dependence of the zero-shear rate viscosity is plotted in **Figure 5.3b**. Overall, the zero-shear viscosity of polymer solutions increased with increasing concentration. PEO solutions exhibited relatively lower shear viscosities compared to viscosities measured for mucosalivary fluids (range: 0.015-0.165 mPa-s for η_0), indicated by the gray box in the figure. The shear viscosities of 0.5% CMC solutions,

0.5% and 1.0% Muc5AC solutions, and Sigma solutions were more comparable. The degree of shear thinning also increased with higher polymer concentration, particularly noticeable in Muc5AC gels (**Supplementary Figure S5.1b**). At the highest concentration of Muc5AC, the viscosity decreased approximately an order of magnitude over the range of shear rates tested. Similarly large degrees of shear thinning were also observed in mucosalivary fluid as we have previously reported [23] (**Supplementary Figure S5.2**). PEO and CMC solutions showed lesser degrees of shear thinning behavior (**Supplementary Figure S5.1c**, **S5.1d**), along with a more obvious low shear rate plateau viscosity.

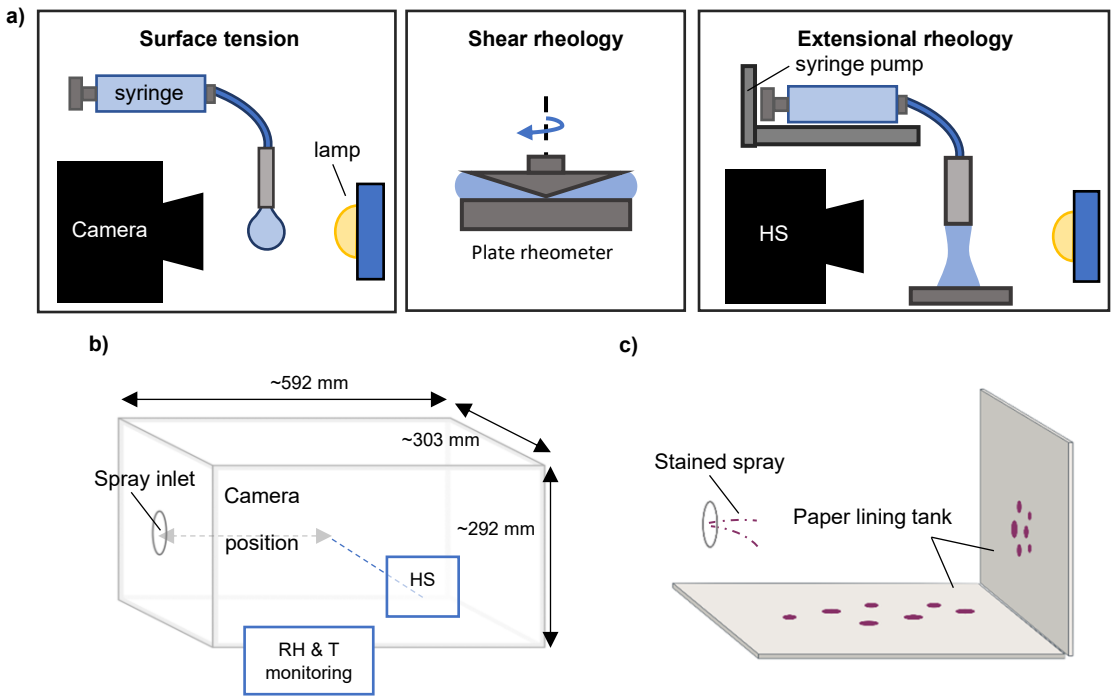

Figure 5.2 Schematic of experimental setups used to study mucus breakup. a Instruments/methods for measuring surface and bulk rheological properties of solutions, including (left to right) pendant drop method, shear rheometry, and dripping-onto substrate. **b** Experimental chamber for spray visualization and sizing of droplets with a high-speed camera (HS, RH & T: relative humidity and temperature). **c** Stain assay to capture stained spray droplets for quantification of spatial dispersion.

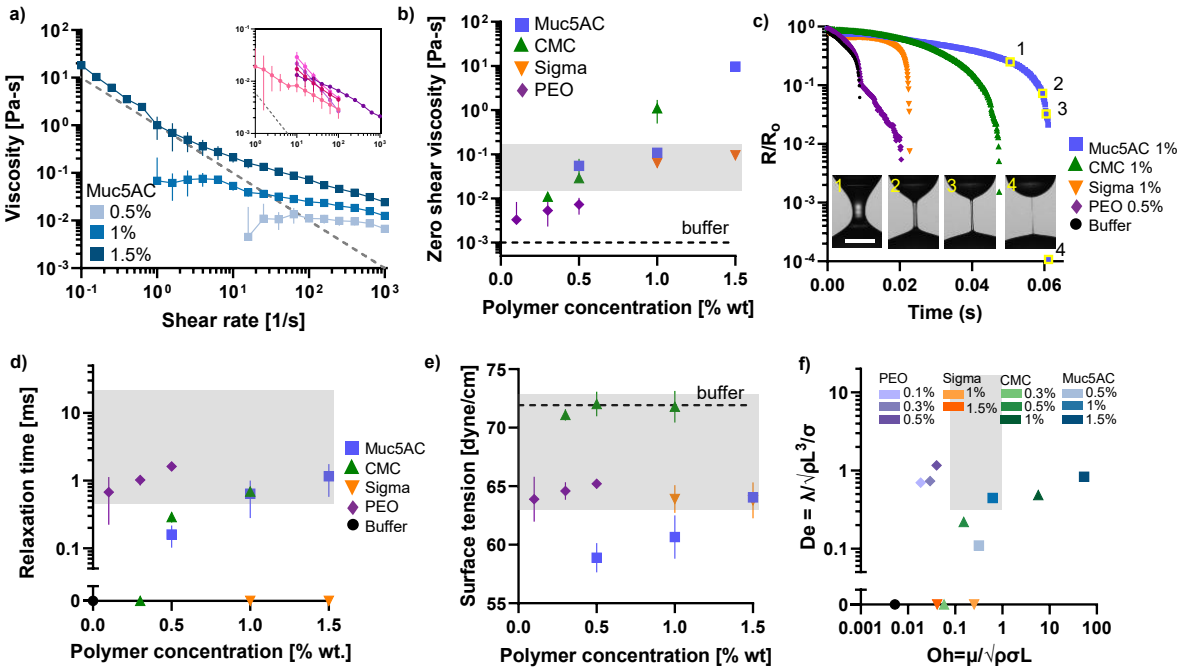

Figure 5.3 Surface and bulk rheological properties of mucus polymer models. a Steady state shear flow viscosity measurements of Muc5AC gels. Dashed line denotes the low torque limit for the ARES-G2 with an 8 mm parallel plate. Inset shows flow curves of mucosalivary fluid from 5 donors and the low torque limit for a 40 mm cone plate. Each point represents the average of three replicates and the error bars indicate standard deviation (s.d.). **b** Zero shear viscosity as a function of polymer concentration for Muc5AC (blue squares), CMC (green triangles), Sigma (orange inverted triangles), and PEO (purple diamonds). The shaded area denotes the measured range of values for mucosalivary fluid from 5 donors. The black dashed line denotes the average measurement for buffer. Each point represents the average of three to five replicates and the error bars indicate s.d. **c** Non-dimensional radius evolution (R/R_0) of liquid threads under capillary-driven thinning for select solutions, where R_0 is the nozzle radius. The colors and symbols correspond to those in b for a given polymer, and the black circles are experiments with buffer. Inset images show the thinning dynamics of 1% Muc5AC gels with a scale bar of 1 mm. **d** Relaxation time, determined from exponential fitting of equation (5.2) to the elastocapillary regime of the radius evolution data (see Methods), as a function of polymer concentration. The shaded area denotes the measured range for mucosalivary fluid from 3 donors. Each point represents the average of three to five replicates and the error bars indicate s.d. An axis break on the y-axis is used to include fluids that had immeasurable relaxation time. **e** Surface tension as a function of polymer concentration for Muc5AC (blue squares), CMC (green

triangles), Sigma (orange inverted triangles), and PEO (purple diamonds). The shaded area denotes the measured range of values for mucosalivary fluid from 5 donors. The black dashed line denotes the average measurement for buffer. Each point represents the average of three to five replicates and the error bars indicate s.d. **f** Regime map of dimensionless numbers, Deborah number (De = $\frac{\lambda}{\sqrt{\frac{\rho L^3}{\sigma}}}$) and Ohnesorge number (Oh = $\frac{\eta}{\sqrt{\rho\sigma L}}$), where λ is relaxation time, ρ is fluid density, σ is surface tension, η is zero shear viscosity, and L is the nozzle diameter. The shaded area indicates the range of De and Oh for mucosalivary fluid from donors. The symbols correspond to those in **b-e**, with the shading denoting polymer concentration (see legend). An axis break on the y-axis is used to include fluids that had De=0.

In addition to viscosity, elasticity is an important property governing droplet formation of biopolymer solutions. Droplet formation involves extensional fluid flow as liquid filaments thin and break. Dilute polymer solutions in extensional flows often exhibit elasticity due to stretching of polymer chains, which can delay the process. The influence of elasticity is described by the elastic relaxation time of the polymer chains, with larger relaxation times leading to a delay droplet breakup. We measured the relaxation time of mucosalivary fluid from several donors and solutions of mucus polymer models using Dripping-onto-Substrate (DoS) rheometry, a technique ideal for evaluating the extensional properties of low viscosity and weakly elastic fluids [30]. In this technique, a liquid droplet extruded from a nozzle is brought into contact with a glass substrate, resulting in the formation of a liquid filament. The thinning of the liquid filament is recorded with a high-speed camera, and the resulting videos are analyzed to extract the filament radius, R, as a function of time.

Representative data of the non-dimensional radius, R/R_0, over time, where R_0 is the intitial filament radius, is shown in **Figure 5.3c** for select polymer solutions and buffer. The plots show that, for each solution, the filament radius decreases with time. The non-dimensional radial evolution of the 0.5% PEO solution (purple diamonds) shows a distinct transition from initial inertiocapillary thinning to elastocapillary thinning: the linear portion of the data on the log-linear plot [20]. The insets show images taken at four times during the thinning of a filament of 1% Muc5AC gels, corresponding to the four highlighted points on the plot. The images show that Muc5AC gels are also elastic in nature but have a short interval corresponding to elastocapillary thinning which we similarly observed in 1% CMC. Buffer and 1% Sigma mucin

show an evolution of R/R_0 known as intertiocapillary thinning that is characteristic of Newtonian fluid. The longer time to breakup of the Sigma mucin solution relative to buffer can be attributed to the increased viscosity. For solutions exhibiting elastocapillary thinning, the slope of the linear region is inversely proportional to the elastic relaxation time, λ. The elastocapillary thinning regime for each material was fitted with an exponential function (see Methods) to extract relaxation times for all solutions, which we plot in **Figure 5.3d**. Due to the challenge of analyzing thinning with beads-on-a-string dynamics for some donor mucosalivary fluid, the relaxation time range for mucosalivary fluid (range: 0.45-22.1 ms) was based on 3 donors whose mucosalivary fluid did not form beads-on-a-string. All polymer solutions, except Sigma mucin, were weakly elastic and had relaxation times less than 3 ms, corresponding to the least elastic mucosalivary fluids. The relaxation time of CMC and Muc5AC solutions increased roughly linearly with increasing polymer concentration. A detailed summary of the variability in rheological properties for mucosalivary fluids is provided in **Supplementary Figure S5.2**.

To assess the surface tension of mucosalivary fluid and other solutions investigated here, we used the pendant drop method. Surface tension measurements for each solution are plotted as a function of polymer concentration in **Figure 5.3e**. The surface tension of mucosalivary fluid from 5 donors varied between 63.0 and 71.9 dyne/cm and is shown as a gray box in the figure. Although native mucus contains surfactant molecules such as phospholipids and surface-active proteins, reconstituted Muc5AC mucin gels and Sigma mucin alone exhibited surface-active properties and lowered the surface tension relative to buffer. Similarly, PEO, which is known to be a surface-active molecule that forms a monolayer at the air-water interface [31], lowered the surface tension of buffer even at low polymer concentrations. On the other hand, the addition of CMC polymer to buffer did not affect the surface tension within the range of polymer concentrations tested. Overall, the addition of polymers decreased the surface tension of water by at most 20%. This change is low compared to the changes in viscosity and relaxation time induced by the polymers. Therefore, changes in surface tension are not expected to dominate the spray behavior of the polymer solutions.

To identify the dominant physics governing droplet formation of our samples, we considered dimensionless numbers obtained from ratios of characteristic timescales. The combined effects of viscosity, elasticity, and surface tension on droplet formation are described by three characteristic timescales [32,33]: the viscous timescale $t_{visc} = \mu L/\sigma$ over which surface tension breaks a viscous filament, the Rayleigh timescale $t_R = \sqrt{\rho L^3/\sigma}$ over which surface tension breaks an inviscid filament, and the timescale of polymer relaxation λ. Here, μ is the fluid viscosity,

L is the nozzle diameter, σ is the surface tension of the fluid, and ρ is the fluid density. Ratios of these timescales yield two dimensionless numbers: the Deborah number $De = \lambda/t_R = \lambda/\sqrt{\rho L^3/\sigma}$, reflecting the importance of elasticity; and the Ohnesorge number $Oh = t_{visc}/t_R = \mu/\sqrt{\rho\sigma L}$, reflecting the importance of viscosity. When Oh>>1, viscosity dominates over surface tension; in a similar manner, when De>>1, elasticity dominates over surface tension.

The Deborah number and Ohnesorge number for each fluid tested are plotted in **Figure 5.3f**. The dimensionless number regime map demonstrates that the breakup of mucus polymer models is influenced by distinct fluid behaviors depending on polymer type and polymer concentration. This underscores the importance of carefully selecting an appropriate model system to mimic the mechanical properties of mucus. The Oh of mucosalivary fluid from donors ranged between 0.07 and 0.94 and the De ranged between 0.33 and 16.8. In comparison, the Oh of mucus polymer models spanned a wider range with values greater than 1 for solutions with greater polymer concentration (e.g., 1% CMC and 1.5% Muc5AC). The De of mucus polymer models remained below 1.2 and was zero for buffer, Sigma mucin solutions, and 0.3% CMC. For CMC and Muc5AC, increasing polymer concentration corresponds to a transition from weakly viscoelastic behavior (De ≈ Oh ≈ 0.1) to predominantly viscous behavior (De << Oh). PEO solutions showed predominantly elastic behavior (De >> Oh). The plots show that buffer has De ≈ Oh ≈ 0, indicating that elasticity and viscosity are negligible, and that droplet formation is dictated by the balance of surface tension and inertia. Sigma mucin shows De ≈ 0 and Oh ≈ 0.1, indicating that viscosity weakly contributes to droplet formation. These results highlight that mucosalivary fluids exhibit high degrees of elasticity despite modest shear viscosities, whereas mucus polymer models had limited elasticity despite containing physiologically relevant polymer concentrations.

5.3.2 Spray Assays

To investigate differences in fragmentation dynamics between mucus polymer models, high-speed camera imaging was used to visualize and measure droplet size distributions and average droplet radius. Solutions were sprayed into an experimental temperature-and-humidity-monitored chamber via a circular inlet and a high-speed camera was use to record videos of sprays at different distances from the nozzle (**Figure 5.2b**).

To assess the distribution of droplet sizes of the sprays, we recorded videos of the spray region approximately 100 mm away from the nozzle. **Figure 5.4a** shows an example image of a

spray of 1% Muc5AC gels with a picture inset of an average sized droplet. A summary of spray images for all solutions is shown in **Supplementary Figure S5.3**. For each spray, a tracking algorithm was used to identify and determine the size of droplets. **Figure 5.4b** shows representative probability density functions (PDFs) of droplet size for different concentrations of Muc5AC. Higher mucin concentrations both shifted and broadened these droplet size distributions, resulting in increases in the average droplet radius. The probability distribution functions for each polymer were used to calculated the average particle size, which are plotted as a function of polymer concentration in **Figure 5.4c**. Like Muc5AC mucin, the average droplet radius of PEO and CMC sprays increased with increasing polymer concentration. For a given concentration, the average droplet radius of PEO was largest, followed by CMC, Muc5AC, and Sigma mucin. Sprays of Sigma mucin (which exhibited no shear thinning (**Supplementary Figure S5.1c**)) and no elasticity (**Figure 5.3e**) were qualitatively very similar to those of buffer (**Supplementary Figure S5.3**), and yielded densely packed, small droplets. The higher shear viscosity of Sigma mucin compared to buffer demonstrates that an increase in the Oh number alone (**Figure 5.3f**) is insufficient to increase the average droplet size. The larger average droplet sizes observed in other polymers, in particular PEO which had low Oh but relatively high De, are then likely attributable to elastic effects. One exception was 0.3% CMC, which did not have measurable elasticity using the DoS method (**Figure 5.3e**) and had similar Oh to 1.5% Sigma mucin yet produced significantly larger droplets (**Supplementary Figure S5.3**). Comparing the average droplet sizes of polymers as a function of De and Oh, respectively, shows that there is not a strict relationship to drop size across all polymers (**Supplementary Figure S5.4**). Here, other factors such as differences in polymer network structure (e.g., polymer properties not accounted by bulk properties), may have played a role.

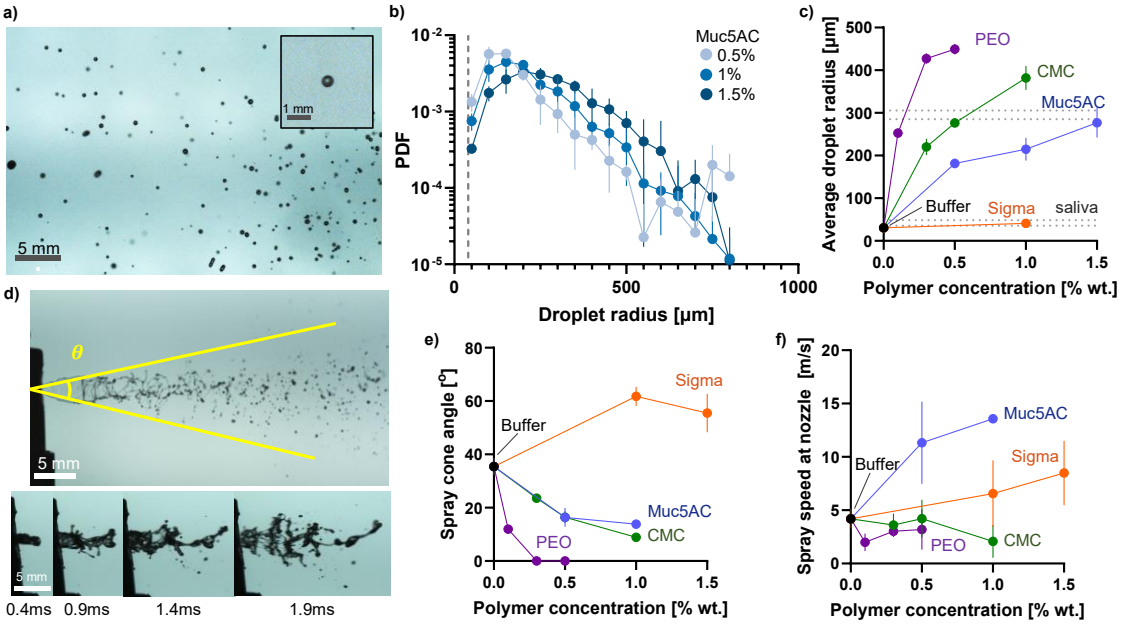

Figure 5.4 Polymer solutions show a range of droplet sizes and dispersion in the air upon spraying. a High-speed (HS) image of a spray of 1% Muc5AC gels with a picture inset of an average sized droplet. **b** Probability density function (PDF) as a function of droplet radius for Muc5AC gels. The dashed line indicates the minimum resolution of the HS camera setup (~approximately 40 μm). The average number of droplets tracked per spray replicate is summarized in Supplementary Table S5.1. **c** Average droplet radius as a function of percent weight polymer concentration. Dotted lines are the average droplet radii for sprayed mucosalivary fluid from 4 donors. The average number of droplets tracked per spray replicate is summarized in Supplementary Table S5.1. **d** HS images of spray cone angle and spray front near the nozzle for 1% Muc5AC gels. **(e, f) e** Spray cone angle and **f** spray speed

For mucosalivary fluids, we observed large differences in fragmentation for a given sample between several sprays. As a result, we retained the first spray only for a given sample to extract the average droplet size. We found that the average droplet size of mucosalivary fluid exhibited a broad range; average radii from different donors are indicated by dashed lines in **Figure 5.4c**. In particular, samples that produced average droplet sizes comparable to buffer and Sigma mucin were generally those with the lowest elasticity or low De while the samples that produced larger droplets on average were more elastic by comparison (**Supplementary Figure S5.4**). In addition to average droplet radius, we investigated the spread of droplets in the air by measuring the spray cone angle and spray speed at the nozzle. Example images of the

spray cone angle measurement and sequence images used to measure the speed of the spray front are shown in **Figure 5.4d** for 1% Muc5AC gels. Additional spray cone angle images for other fluids are shown in **Supplementary Figure S5.3**. The spray cone angle of Muc5AC and CMC decreased with increasing polymer concentration indicating reduced dispersion (**Figure 5.4e**). On the other hand, Sigma mucin had a larger cone angle compared to the buffer solution demonstrating increased spread. PEO jetted out of the nozzle and therefore did not have a measurable cone angle. The spray speed of Muc5AC and Sigma mucin increased with increasing polymer concentration (**Figure 5.4f**) while that of CMC and PEO was lower than that of buffer, and decreased overall with increasing polymer concentration. We hypothesize that the heterogeneity of the mucin gels samples and / or the presence of insoluble aggregates in Sigma mucin may make the spray flow more unsteady which may lead to qualitative differences in spray speed and cone angle. In addition, we hypothesize that the relatively high degree of shear thinning in Muc5AC mucin gels may contribute to its higher speed relative to other polymer solutions that displayed only small degrees of shear thinning.

5.3.3 Effect of charged nanoparticles

Viruses are known to present chemically complex, charged surfaces that have been proposed to form strong electrostatic interactions with other biological components [34]. Based on the charged nature of mucins, we hypothesized that the presence of viruses may influence the network structure and droplet formation of mucus. To test this, we added charged nanoparticles 200nm in diameter in size, as virus surrogates, to 1 wt. % solutions of the various biopolymers. The concentration and charge of the nanoparticles (carboxylated – net negatively charged, or aminated – net positively charged) was varied to simulate variations in pathogen type and viral load. Viral loads in infectious disease vary widely and depend on various factors including disease severity, physiological site [35–37]. In our study, we vary the particle load approximately between 10^8 and 10^{10} particles/mL. We first repeated our rheological measurements of the polymer solutions with nanoparticle suspensions. We observed that carboxylated (negatively charged) nanoparticles decreased the surface tension of Muc5AC mucin gels in a concentration-dependent manner (**Figure 5.5a**). The addition of aminated (positively charged) nanoparticles further decreased the surface tension of Muc5AC mucin gels compared to carboxylated ones (**Figure 5.5b**). By contrast, the surface tension of Sigma mucin, CMC, and buffer was unchanged by the addition of either carboxylated or aminated nanoparticles. Notably,

these changes in surface tension could not be probed by shear rheological measurements. The addition of nanoparticles did not affect the shear viscosity and viscoelastic moduli (G' and G") of Muc5AC or CMC gels compared (**Supplementary Figure S5.5**).

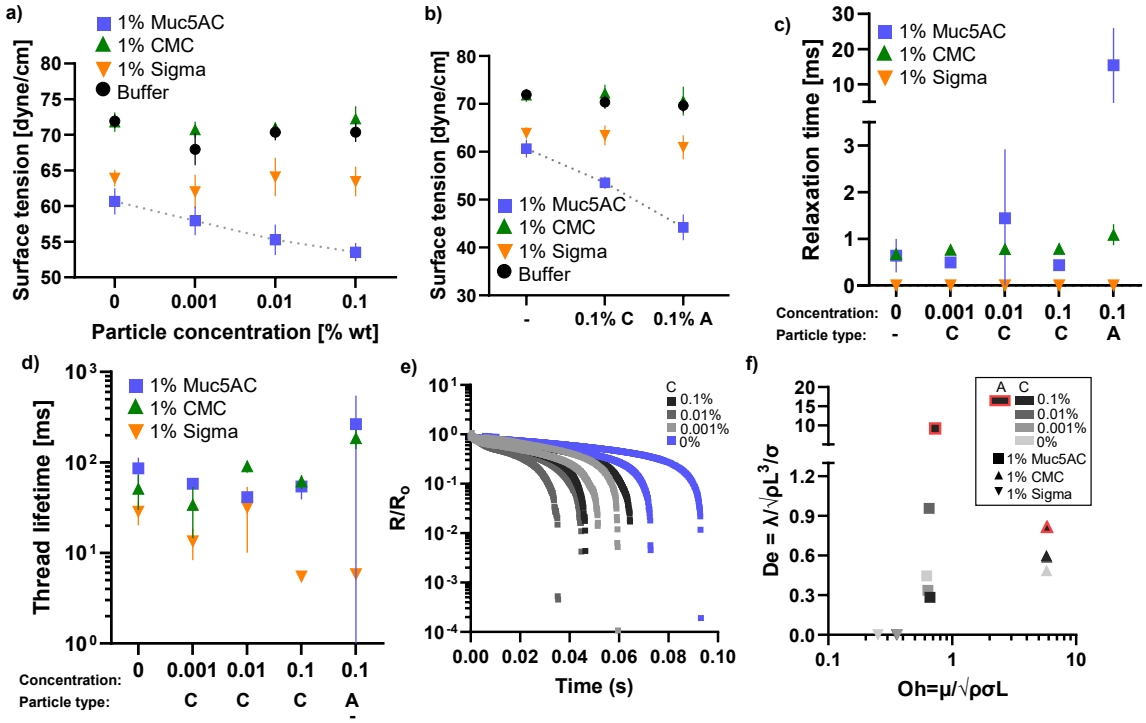

Figure 5.5 Charged nanoparticle suspensions modulate the bulk physical properties of Muc5AC gels. a Surface tension of polymer solutions with varied concentrations of 200 nm diameter carboxylated nanoparticles. The symbols correspond to 1% Muc5ac (blue squares), 1% CMC (green triangles), 1% Sigma (inverted triangles), and buffer (black circles). **b** Surface tension of polymer solutions with suspensions of 0.1% 200 nm diameter carboxylated (C) and aminated (A) nanoparticles. Each point represents the average of three or more replicates and the error bars indicate standard deviation (s.d.). The dotted line highlights the decreasing trend in 1% Muc5AC gels. **(c, d) c** Relaxation time and **d** thread lifetime of polymer solutions with varied concentrations of carboxylated (C) and aminated (A) nanoparticles. Each point represents the average of three or more replicates and the error bars indicate s.d. **e** Non-dimensional radius evolution of liquid threads under capillary-driven thinning for 1% Muc5AC gels containing varied concentrations of C nanoparticles. Two replicates are shown for each condition; one above and one below the measured average thread lifetime in **d**. **f** Regime map of dimensionless Deborah ($De = \frac{\lambda}{\sqrt{\frac{\rho L^3}{\sigma}}}$) and Ohnesorge ($Oh = \frac{\eta}{\sqrt{\rho\sigma L}}$) numbers for solutions with and without nanoparticle suspensions, where λ is relaxation time, ρ is fluid density, σ is surface tension, η is zero shear viscosity, and L is the nozzle diameter. Note the y-axis break used to include the higher relaxation time of 1% Muc5AC gels with 0.1% A. Also note that De and Oh were determined using the average values of measured bulk properties.

We next studied the effect of nanoparticles on the extensional rheology of solutions of Muc5AC, CMC, and Sigma mucin. In addition to the relaxation time (**Figure 5.5c**), we also report the thread lifetime (**Figure 5.5d**) to reflect the contribution of nanoparticles to the overall dynamics of filament thinning. The plots show that the addition of positively charged particles to Muc5AC gels greatly increased the relaxation time and widely varied the thread lifetime (additionally reference **Supplementary Figure S5.6**). By contrast, the addition of positively charged nanoparticles to CMC only slightly increased the relaxation time and increased the thread lifetime. Positively charged particles did not affect the relaxation time of Sigma mucin, which remained immeasurable. Negatively charged particles did not substantially affect the relaxation times of the polymers tested. However, negatively charged particles did reduce the thread lifetime (**Figure 5.5d**), particularly for Muc5AC gels, by reducing the duration of the Newtonian thinning regime (**Figure 5.5e**). While the relaxation time of Sigma mucin was unchanged by the addition of nanoparticles, a general decrease in thread lifetime was also observed with increasing particle concentration but was independent of particle charge (**Figure 5.5d**).

To summarize the effect of nanoparticles on the relaxation time of polymer solutions, we again plot the dimensionless De and Oh numbers for 1% CMC, Muc5AC, and Sigma gels with and without the charged nanoparticles (**Figure 5.5f**). The plot shows Sigma mucin gels are negligibly impacted by the addition of nanoparticles. On the other hand, the large increase in relaxation time from the addition of the aminated nanoparticles results in substantial increases to the De of the Muc5AC gels, with minimal changes to the Oh (from a decrease in surface tension).

Sigma mucin and Muc5AC may exhibit varying responses to charged particles due to differences in their mucin structures. Sigma mucin possess damaged or absent mucin structures (e.g., hydrophobic terminal domains or mucin glycans), stemming from industrial processing [38]. Consequently, this may lead to modified interactions between mucin and particles. Additionally, the compromised mucin structures might induce conformational changes in the Sigma mucin polymer, rendering specific regions inaccessible to charged particles which may result in different rheological properties. In contrast to Sigma Mucin, we found that CMC, a hydrophobic and negatively charged polymer like mucin, followed the De trends observed in Muc5AC, but only had minimal increases in De (from minimal increase in relaxation time and no change in surface tension). Hence, properties other than polymer charge (e.g., geometrical

influences of the network structure on particles) may dictate how charged particles arrange themselves in the bulk fluid or the fluid's interface during capillary thinning.

Our observations of the effects of particles on relaxation time are consistent with previous studies. Harich et al. found that non-Brownian particles added to polymer solutions also increased the relaxation time with increasing polymer concentration and increasing particle volume fraction [39]; the authors found that extensional properties were sensitive to the presence of aggregates that formed as a result of polymers introducing depletion (attractive) interactions in suspensions of non-interacting particles. From microscopy images, we observed more aggregation in suspensions of aminated particles compared to carboxylated particles (**Supplementary Figure S5.7**). Our results in thread lifetime share similar observations with earlier works as well. For example, Thievenaz and Sauret report that the thinning of non-Brownian (polystyrene) suspensions becomes faster at a critical filament diameter than for a fluid of equivalent viscosity with increasing volume fractions [40]. Similarly, van Deen et al. found that small volume fractions of particles in viscous fluids, which did not change the viscosity of the interstitial fluid, also accelerated pinch-off and subsequently shortened the length of the filament [25]. These effects were attributed to particle rearrangement in the thinning thread that leads to an onset of heterogeneity in the flows of suspensions and local particle concentration. Importantly, the observations from the literature highlight that the influence of particles can be independent of bulk viscosity and that particles can influence the dynamics of thinning on length scales much larger than the particle size. Although we observed an overall decrease in the surface tension of 1% Muc5AC gels with nanoparticles, the rearrangement of particles in the fluid thread during thinning may lead to local surface tension gradients [41] which cannot be predicted by the bulk surface tension alone; in our results, we also see that the degree of interaction between particles and between particle and polymer are important for understanding the dynamics of polymer-particle solutions.

We next sprayed the 1% wt. polymer solutions with particle suspensions in the experimental chamber to investigate the influence of particle load and charge on droplet size, spray depth, and spray clustering. We observed that the median (**Figure 5.6a**) and average (**Figure 5.6b**) droplet size of Muc5AC solutions increased in the presence of negatively charged particles. However, droplet size was not a monotonic function of particle concentration: instead, the droplet size remained approximately constant for all particle concentrations (at a larger average value than in the case with no particles, **Figure 5.6b**). The average droplet size of CMC solutions with nanoparticles was minimally affected by the addition of nanoparticles; the average

droplet size lowered slightly with increasing particle concentration (**Figure 5.6c**). Positively charged particles appeared to not have an effect on the average droplet size of 1% Muc5AC gels or CMC (**Figure 5.6b**, **Figure 5.6c**). However, a closer look at the droplet size distribution of 1% Muc5AC gels showed that although the median droplet size was not substantially impacted by the presence of aminated particles (minimal shift in the PDF), the incidence of larger droplets was higher relative to the case with no particles (examine the distribution tails in **Figure 5.6a**).

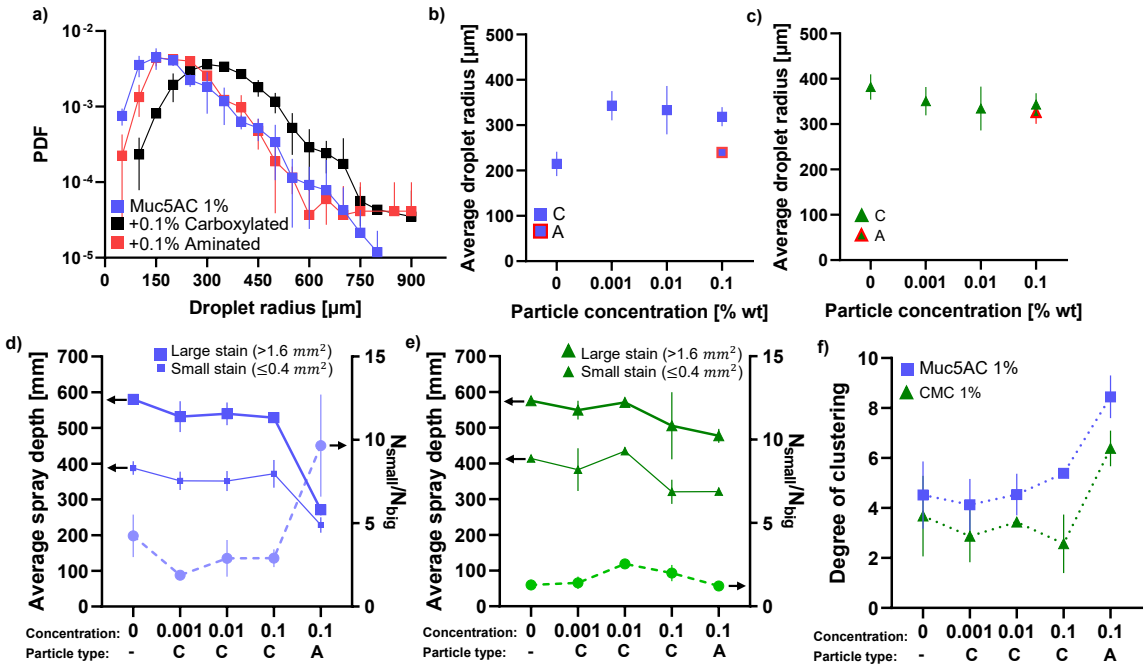

Figure 5.6 Nanoparticles modulate the droplet size and spatial dispersion of sprays. a Probability density function (PDF) of droplet sizes for 1% Muc5AC gels without nanoparticles (blue squares), with 0.1% carboxylated nanoparticles (red squares), and 0.1% aminated nanoparticles (black squares). Each point represents the average of three replicates and the error bars indicate standard deviation (s.d.). The average number of droplets tracked per spray replicate is summarized in Supplementary Table S5.2. **(b, c)** Average droplet radius of **b** 1% Muc5AC gels and **c** 1% CMC gels with varied concentrations of 200 nm diameter carboxylated (C) and aminated (A) particles. Each point represents the average of three replicates and the error bars indicate s.d. The average number of droplets tracked per spray replicate is summarized in Supplementary Table S5.2. **(d, e)** Average spray depth (solid lines) of small stains ($\leq 0.4\ mm^2$) and large stains ($> 1.6\ mm^2$) and ratio of number of big to small stains (dashed lines) of **d** 1% Muc5AC gels and **e** 1% CMC gels with varied concentrations of C and A particles. Each point represents the average of three replicates and the error bars indicate s.d. **f** Degree of clustering of stains from sprays of 1% Muc5AC and 1% CMC gels with different nanoparticle concentrations. Each point represents the average of three replicates and the error bars indicate s.d.

In addition to high-speed imaging, we studied the effect of nanoparticles on the spatial dispersal of droplets by staining the solutions with Rhodamine B dye prior to spraying into the experimental chamber (**Figure 5.2c**). Stained spray droplets were captured on white paper

lining the inside of the experimental chamber and the stained paper was imaged with a camera. Images were processed to extract stain features such as the size and locations of the stains to determine spray depth and spatial clustering of stains. We found that positively charged particles greatly reduced the average depth of large and small stains of Muc5AC droplets (see Methods) and produced a larger fraction of small stains relative to big stains (**Figure 5.6d** and compare **Supplementary Figure S5.8a**, **S5.8c**). Importantly, this effect was not seen in CMC (**Figure 5.6e** and compare **Supplementary Figure S5.8d**, **S5.8f**) or in Sigma mucin (**Supplementary Figure S5.9d** and compare **Supplementary Figure S5.9a, S5.9c**). On the other hand, negatively charged particles had minimal influence on either the spray depth or on the ratio of the number of small stains to the number of large stains for all three polymers (i.e., Muc5AC, CMC, and Sigma mucin). The spread of droplets was determined by calculating the degree of clustering using Voronoi cells (see Methods); a greater number indicates that droplets are tightly clustered. We found that positively charged particles produced a high degree of clustering in CMC and Muc5AC gels (**Figure 5.6f** and visually observed in **Supplementary Figure S5.8e and S5.8f**). By contrast, clustering remained approximately constant in the presence of varying concentrations of negatively charged particles. Sigma mucin sprays with and without nanoparticle loads produced a greater proportion of small droplets compared to either sprays of Muc5AC or CMC which contributed to a high degree of clustering (**Supplementary Figure S5.9e**).

5.4 Discussion

The biophysics of transmission remain a critically understudied area in the context of directly transmitted respiratory viral diseases. Viral particles must remain viable in the complex environment of emitted mucosalivary droplets subject to evolving biochemistries and mechanical stresses during droplet evaporation, and must then successfully cross the mucosal barriers of susceptible hosts to initiate infection. The critical role that mucus plays in infectious disease transmission both externally and within-host necessitates careful experimental consideration.

Here, we found that the presence of natively purified mucins modulates the fragmentation dynamics and final droplet size distribution during spraying in a unique way compared to other biopolymers or industrially purified Sigma mucins. Although we observed substantial variability between donors, mucosalivary solutions are generally characterized by

high degrees of elasticity and relatively modest shear viscosities that exhibit high degrees of shear thinning. Thus, elasticity appeared to be an important contributor to the increase in average droplet size compared to buffer solutions and Sigma mucin that we observed in Muc5AC gels. In terms of transmission dynamics, larger droplets may settle more quickly out of the air, favoring routes of disease such as direct or fomite transmission.

To simulate how viruses may modify the dynamics of transmission, we added virus-sized nanoparticles of net positive and negative charge to the biopolymer solutions. In reality, viral particles typically feature a wide array of alternating surface charges, which has been hypothesized to mitigate strong electrostatic interactions with other biological components [42]. Adding virus-sized particles of both charges to Muc5AC mucin gels reduced their surface tension and altered their filament thinning behavior, resulting in changes to the droplet size distributions of the fluid sprays. The effect of adding positively charged nanoparticles to the Muc5AC gels was particularly striking, and not observed for other biopolymers including CMC and Sigma mucin. Overall, aminated particles strongly increased the extensional viscosity of the Muc5AC gels, but in a heterogeneous fashion, resulting in widely varying lifetimes of thinning filaments. We hypothesize that mechanistically, this may be due to rearrangement of the mucin network structure via electrostatic binding into mucin-rich and mucin-poor regions [43]. It is worth highlighting that modifications to the microstructure may not manifest into measurable changes in the bulk mechanical properties of the material [44]. Indeed, adding aminated particles increased the ratio of small to large droplets in the Muc5AC gel sprays, and decreased the distance travelled by large droplets in particular. High degrees of elasticity in mucin-rich regions may result in the coalescence of adjacent droplets connected by liquid threads into larger droplets, which may settle more quickly under gravity. In contrast, mucin-poor phases and lower elasticity may lead to the formation of smaller droplets.

We found that adding negatively charged particles did not affect the relaxation time of Muc5AC gels, perhaps as a result of minimal interactions with the net negatively charged mucin network, but did reduce the lifetime of the thinning threads. In other words, in the air, the span of time for which ligaments stretch would be reduced in the presence of negatively charged particles. We may be able to compare this to results of Keshavarz et al. [19] who concluded that the reduced lifetime of viscoelastic solutions compared to Newtonian fluids of equivalent viscosity caused less stretching, shorter, and thicker viscoelastic ligaments which subsequently produced larger droplets on average.

Our results suggest that the presence and charge of viruses and their interactions with mucin polymers may impact the size of emitted droplets by infectious hosts, with important

implications for disease transmission. Indeed, respiratory viruses exhibit different tropism (i.e. preferences for cell types that are expressed in different parts of the airways [45], and droplet size may facilitate this (i.e. smaller aerosols may be able to preferentially reach the smallest airways of the deep lung). Compared to buffer alone, the presence of mucins may mitigate transmission via the aerosol route by favoring the production of larger respiratory droplets in the presence of charged nanoparticles. To validate this, future studies should build on these experiments using nanoparticles with surfaces chemistries closer to those of viruses (i.e., alternating charges) and / or using native virus systems. Combining these studies with evaluations of viral viability under spraying conditions will be critical for wholistically evaluating transmission biophysics, which will be key for developing mechanistic models for disease transmission and guiding public health recommendations in the face of new and emerging pathogens.

5.5 Methods

Experimental chamber

The experimental chamber used in this study was an in-house made setup (**Figure 5.2b**). The chamber was constructed with laser-cut acrylic sheets (McMaster-Carr, Elmhurst, IL, USA) to a final overall dimension of approximately 592 mm x 303 mm x 292 mm (l x w x h). The inside of the chamber was accessible via a rectangular opening at the top of the chamber; the top was sealed during all tests and opened for cleaning between tests or prepping the chamber for tests with the stain assay. Sprays were released through a circular inlet at the front wall of the chamber. Silica beads were used to remove the moisture in the chamber to ensure tests were at indoor conditions (T=21$\pm$1 °C and RH=30$\pm$5%). The temperature (T) and relative humidity (RH) conditions inside of the chamber were monitored using Arduino (Arduino, Model No. 2560 R3) and temperature and humidity sensors (Adafruit Industries, Part No. 3251).

Nanoparticle preparation

Fluorescent, negatively charged (carboxylated) microspheres (Magsphere Inc., Catalog No. CAYF-200NM) and positively charged (aminated) microspheres (Magsphere Inc., Catalog No. AMYF-200NM) of approximately 200 nm in diameter were used in experiments with nanoparticle suspensions. Nanoparticles was prepared to a final weight concentration of: 0.001 %, 0.01 %, and 0.1 % (w/v). Nanoparticles were originally in an aqueous suspension at 2.5

%w/v (~6x10^{11} particles/mL); the aqueous suspension typically includes surfactants that can interact with polymers via hydrophobic interactions and alter rheological properties such as surface tension at high enough concentrations. In **Supplementary Figure S5.10**, we show a comparison of surface tension measurements of 10 mM sodium phosphate buffer with and without the centrifugation process. Consequently, we used centrifugation to remove the aqueous part of the suspension. First, a measured volume of nanoparticle solution was diluted in 100 μL of MilliQ water and centrifuged for 25 min at 15.6 rcf. After centrifugation, the supernatant, which included the MilliQ water and the aqueous part of the nanoparticle solution, was removed with a micropipette. The observable pellet that remained was then combined with solubilized solutions after 24 hrs or immediately with buffer that was used for testing.

Preparation of CMC gels, Sigma solutions, and PEO solutions

Studies to simulate the breakup of mucus into droplets typically use water [46], ionic/protein solution [47], synthetic polymers (e.g. polyethylene oxide/glycol (PEO/PEG), carboxymethylcellulose (CMC)) [48], commercial mucin [49], or native mucus. In these studies, native mucus is typically either collected from human subjects and then artificially aerosolized [50] or released directly from a human subject following an exhalation (e.g. breathing, talking, coughing) [51]. While commercial sources of mucin, in particular, porcine gastric mucin (PGM) MUC5AC and bovine submaxillary mucin (BSM) MUC5B are heavily relied on as a source of mucin for research, they exhibit reduced biochemical activity and lack pH-responsiveness due to harsh treatment processes that have been associated with altered mucin structure [52,53]. Similarly, while synthetic polymers such as PEO/PEG and CMC are viscoelastic, they lack the unique biochemical responsiveness of mucins to changes in pH or salt. On the other hand, the high degree of variability in composition across individuals and even within individuals makes native mucus a challenging experimental system. Here, we prepare solutions of synthetic polymers and commercial mucins to compare with native mucus and reconstituted mucin gels.

CMC sodium salt, average molecular weight = 250 kDa and degree of substitution =0.7 (CAS: 9004-32-4) purchased from Acros Organics (Thermo Fisher Scientific, Waltham, MA, USA) was used to prepare a solution of CMC in distilled water at 50 mg/mL. The CMC solution was dialyzed against distilled water in an Amicon stirred cell (UFSC40001, Amicon) equipped with a 100 kDa molecular weight cut-off membrane. Dialysis was performed with two exchanges of water and the resulting solution was concentrated before lyophylization. Dried CMC was stored at -80 °C until use. CMC was weighed and solubilized for 24 hours with gentle shaking at

4 °C in 10 mM sodium phosphate buffer (pH 7) and gels were prepared the same day by combining the solubilized CMC with the appropriate reagents.

Porcine gastric mucin (Sigma Aldrich, St. Louis, MO, USA) was weighed and solubilized for 24 hours with gentle shaking at 4 °C in 10 mM sodium phosphate buffer (pH 7). PEO (molecular weight = 600 kDa) solutions were prepared by slowly mixing in weighed amounts of PEO in a falcon tube with 10 mM sodium phosphate buffer (pH 7) and then placing the tube on a rotating mixer overnight at 4 °C; this process prevented aggregation of PEO. Solutions were prepared the same day by combining with appropriate reagents.

Solutions were prepared at a 0.5% (w/v) concentration higher than needed for tests and then diluted with buffer to their final concentration. Centrifuged nanoparticles were resuspended in the buffer volume to be added to the concentrated polymer solution by vortexing for 10 s; this step was done to ensure nanoparticles were disaggregated prior to mixing with the concentrated polymer solution.

Collection of mucosalivary fluid samples

Unstimulated submandibular saliva was collected from 5 human volunteers using a custom vacuum setup described by Frenkel and Ribbeck [54]. Subjects were asked to refrain eating food or drinking liquids for at least 1.5 hours prior to their collection. Subjects placed cotton over the inside lining of the cheeks to absorb parotid gland secretions and expectorated secretions under the tongue to collect 5 mL of fluid. The collection tube was kept on ice during collection and throughout testing to preserve the sample. Measurements were done immediately after collection because of sensitivity to sample age and enzymatic degradation [23,55]. Protocols involving the use of human subjects were approved by Massachusetts Institute of Technology's Committee on the Use of Humans as Experimental Subjects.

Mucin purification and reconstitution of mucin hydrogels

MUC5AC mucins were purified from fresh pig stomach scrapings following the methods described previously [56]. Briefly, the isolated mucus layer was solubilized in sodium chloride buffer containing protease inhibitors and sodium azide to prevent mucin degradation and bacterial proliferation, respectively [57], and centrifuged to remove insoluble components. The mucins were isolated using gel filtration chromatography on a Sepharose column (CL2B), and then concentrated, desalted, and lyophilized [57]. Mucins were solubilized for 24 hours with gentle shaking at 4 °C in 10 mM sodium phosphate buffer (pH 7), and gels were prepared the same day as the experiments by combining the solubilized mucins with the appropriate

reagents. Mucin gels were prepared at a 0.5% (w/v) concentration higher than needed for tests and then diluted to their final concentration. Centrifuged nanoparticles were resuspended in the buffer volume to be added to the concentrated mucin gel by vortexing for 10s; this step was done to ensure nanoparticles were disaggregated. All gels were adequately mixed by micropipetting the sample up and down 10 times before performing tests.

Surface tension measurement

Surface tension measurements were performed using the pendant drop method [58] depicted in Figure 2A. A 16-gage needle was used along with Luer connectors, tubing, and a 5 mL syringe and held in place with a laboratory stand and clamp. A DSLR camera with a macro lens, teleconverter, and tube extension was used to record videos of pendant drops with illumination from behind by an LED lamp. Approximately 200 μL of each solution was prepared to generate 5 pendant drops. Videos were converted to frames in MATLAB (Natwick, MA) and select images were analyzed using ImageJ plugin Pendant drop [59]. A total of 3 to 5 measurements were collected and analyzed for each solution; fewer measurements were achieved in solutions that contained bubbles. Surface tension measurements for each solution were averaged and a standard deviation was determined.

Steady shear and oscillatory shear rheology measurement

The shear rheological response of fluids was measured using 2 common experiments: steady state shear flow tests and small amplitude oscillatory shear (SAOS) tests. SAOS flow is used to determine the viscoelastic moduli of the sample and steady state shear flow is used to measure the steady state viscosity of the sample as a function shear rate. All shear rheology measurements were performed using a strain-controlled rheometer (ARES-G2, TA instruments, New Castle, DE, USA), with either a 40 mm 2° cone-and-plate fixture, a 25 mm parallel plate with a gap width of 150 μm, or an 8 mm parallel plate fixture with a gap width of 200 μm (Fig. 2A). Experiments were performed on a Peltier plate at a constant temperature T = 25 °C. For each sample, steady shear measurements were performed on samples in triplicate at shear rates ranging from 10^{-2} to 10^{3} 1/s. SAOS tests were also performed on samples in triplicate using a 25 mm parallel plate and each replicate was measured 2 to 5 times at frequencies ranging from 1 to 100 rad/s. All SAOS tests were performed at a strain amplitude within the linear viscoelastic regime of each gel which was determined from separate strain sweep experiments. For all configurations, the air–sample interface was coated in mineral oil to limit sample evaporation. The instrument and secondary flow limits of steady shear and oscillatory

measurements were calculated using equations described by Ewoldt et al. [60]. A characteristic viscosity was determined for all polymer solutions by fitting steady shear data $(\eta(\dot{\gamma}))$ to the Carreau model [61]:

$$\eta(\dot{\gamma}) = \frac{\eta_0}{(1+(\dot{\gamma}\tau)^2)^{(1-n)/2}} \quad 5.1$$

where η_0 is the zero-shear rate viscosity, $\dot{\gamma}$ is the shear rate, τ is a characteristic time, and n the power law exponent of the apparent viscosity in the shear thinning regime. For samples that were Newtonian (e.g., buffer) or did not observably exhibit shear thinning behavior (e.g., Sigma mucin), an average over all viscosity values was taken as η_0.

Dripping-onto-substrate

Transient extensional rheology of tested solutions was measured using a dripping-onto-substrate rheometry setup previously described by Dinic et al. [30] and illustrated in **Figure 5.2a**. Using a syringe pump, fluid is deposited onto a glass substrate placed a distance, H, below a 16-gage dispensing needle (D_0 = 1.65 mm); the aspect ratio selected was H/ $D_0 \approx 3$. Fluid is delivered at low flow rates and the syringe pump is stopped after fluid touches the glass substrate. After touching the substrate, the fluid spreads and the liquid bridge formed undergoes capillary-driven thinning and breakup. The thinning and breakup of the liquid bridge was recorded with a high-speed camera (FASTCAM Mini AX200 type 900K-C-32GB) at a frame rate of 10,000 frames per second (fps). The videos were analyzed using MATLAB (Natwick, MA) which extracted the neck radius of the thinning filament as a function of time. Each measurement was repeated 3 to 5 times; fewer measurements were achieved in fluids that contained bubbles. The non-dimensional radius as a function of time was plotted as a log-linear plot. The relaxation time of each sample was determined by fitting the exponentially thinning region (the observable linear region in the log-linear plot) of the data $(R(t)/R_0)$ to a decaying exponential function of the form [62]:

$$\frac{R(t)}{R_0} = \left(\frac{GR_0}{2\sigma}\right)^{1/3} e^{-t/3\lambda} \quad 5.2$$

where G is the elastic modulus, R_0 is the initial radius, σ is the surface tension, and λ is the relaxation time.

Spray and high-speed camera experiment

Approximately 300 μL of gel solutions was prepared in small centrifuge tubes and a modified nozzle (Zoizocp, Part no. Zoizocp-0312) was attached and sealed with paraffin film to generate 3 sprays per solution. The nozzle diameter measured 0.5 mm. Depending on the availability of the polymer, up to 6 sprays (either from the same sample preparation or additional sample preparations) were generated and analyzed (including buffer). Sprays were imaged at 10,000 fps at room temperature with a FASTCAM Mini AX200 type 900K-C-32GB. The high-speed camera was placed outside of the chamber and positioned perpendicular to the long side of the chamber; the camera was placed approximately 100 mm from the inlet of the chamber for droplet-sizing tests. An LED light was placed behind the chamber as backlighting and calibration images were taken. The number of frames exported for analysis depended on the duration of the spray; images were processed in MATLAB (Natwick, MA) using a publicly available particle tracking code [63] to extract droplet trajectories and droplet size. The code failed to track buffer and Sigma mucin sprays due to high droplet density in the field of view; hence, Sigma and mucin sprays were manually tracked. The center positions of drops were used to set a local threshold around the drop and built-in MATLAB functions were used to binarize the region around the drop and extract size. To measure spray cone angle and spray speed at the nozzle, the nozzle and tube containing the sample were sprayed from inside of the chamber to image the ejection of fluid directly at the nozzle opening. The camera was placed such that the nozzle head was in the field of view.

Stain assay

Prepared gel solutions were mixed with a 1% (w/v) Rhodamine B (Thermo Fisher Scientific, Catalog No. A13752.18) solution to a final concentration of 0.13% (w/v) which produced a violet tinted solution. We established that this concentration sufficiently stained the solution for visibility on white paper, without impacting the surface tension of the aqueous solution (**Supplementary Figure S5.11**). Importantly, we found that the median stain area from sprays of buffer, CMC, and mucin with and without nanoparticles qualitatively ordered in a manner consistent with droplet sizing done with the high-speed camera (compare **Supplementary Figure S5.12** to **Figure 5.4c**, **Figure 5.6b** and **Figure 5.6c**).

White paper was used to line the back wall and bottom surface of the interior chamber and spray droplets from stained gel solutions were captured on the paper as shown in **Figure 5.2c**. Approximately ~300 μL of gel solutions was prepared in small centrifuge tubes and a modified nozzle was attached and sealed with paraffin film to produce 2 to 3 sprays. White paper was replaced after each spray and repeated 3 times for each sample. A DSLR camera was used to

image the stained white paper with a ruler for calibration. All images were processed through MATLAB (Natwick, MA) and stain features were extracted including area and center position of droplet stains.

Calculation of average spray depth and drop clustering

Dispersal of droplets was assessed by two metrics: average spray depth and drop clustering (i.e., the spatial density of drops). The droplet stain y-coordinates (y-axis, along the longest side of the chamber) were binned by their stain area. Average spray depth was then calculated for small stains ($\leq 0.4\ mm^2$) and large stains ($> 1.6\ mm^2$) separately as follows:

$$\frac{\sum_{i=1}^{N} Y_{pos,i}}{N}, \tag{5.3}$$

where N is the number of small or large stains and $Y_{pos,i}$ is the y-coordinate of stain i.

Droplet clustering was studied using Voronoi diagrams, where scattered points on a plane are subdivided into tessellating polygons, referred to as cells, enclosing a portion of the plane that is closest to each point. Voronoi diagrams have been previously used in other works to study the accumulation of droplets in two-phase flows [64]. For each spray, the center positions of stains on the x-y plane (bottom of the experimental chamber) were divided into Voronoi cells using MATLAB functions. Clustered drops correspond to small Voronoi cells, while drops in areas with fewer drops or void regions correspond to large cells. The area of Voronoi cells was calculated and normalized by the average Voronoi cell area for that spray. The degree of clustering was then quantified as follows:

$$\sigma_{rel} = \frac{\sigma_{expt} - \sigma_{RPP}}{\sigma_{RPP}}, \tag{5.4}$$

where the degree of clustering is a relative standard deviation (σ_{rel}) comparing the standard deviation of measured normalized Voronoi cell areas (σ_{expt}) and normalized Voronoi cell areas distributed by the Random Poisson Process (RPP) (σ_{RPP}). The standard deviation of the 2 dimensional (2D) RPP distribution function is equal to 0.53 [65]; this was previously determined by an exact analytical result determined by Gilbert and additionally supported by Ferenc and Neda who proposed a compact analytical formula using a two-parameter gamma function fit and Monte Carlo-type simulations to describe the Voronoi cell area distribution in 2D [65]. We simulated the 2D RPP process for the number of droplets in each spray on a rectangular area equivalent to the size of the bottom surface of the experimental chamber. The x and y coordinates were uniformly sampled on intervals corresponding to the length and width of the

rectangular region. In alignment with previous works, we found σ_{RPP} to be between 0.5 and 0.6. When $\sigma_{rel} > 0$, the spray deviates from the RPP distribution indicating an accumulation of drops in a particular region and a higher degree of clustering. An overall average and standard deviation were calculated based on repeat spray measurements.

5.6 References

[1] C. Duchaine, C.J. Roy, Bioaerosols and airborne transmission: Integrating biological complexity into our perspective, Sci. Total Environ. 825 (2022) 154117. https://doi.org/10.1016/j.scitotenv.2022.154117.

[2] M. Zanin, P. Baviskar, R. Webster, R. Webby, The Interaction between Respiratory Pathogens and Mucus, Cell Host Microbe. 19 (2016) 159–168. https://doi.org/10.1016/j.chom.2016.01.001.

[3] L. Bourouiba, Fluid Dynamics of Respiratory Infectious Diseases, Annu. Rev. Biomed. Eng. 23 (2021) 547–577. https://doi.org/10.1146/annurev-bioeng-111820-025044.

[4] N.H.L. Leung, Transmissibility and transmission of respiratory viruses, Nat. Rev. Microbiol. 19 (2021) 528–545. https://doi.org/10.1038/s41579-021-00535-6.

[5] L.A. Reperant, T. Kuiken, B.T. Grenfell, A.D.M.E. Osterhaus, A.P. Dobson, Linking Influenza Virus Tissue Tropism to Population-Level Reproductive Fitness, PLoS One. 7 (2012). https://doi.org/10.1371/journal.pone.0043115.

[6] O. Lieleg, I. Vladescu, K. Ribbeck, Characterization of particle translocation through mucin hydrogels, Biophys. J. 98 (2010) 1782–1789. https://doi.org/10.1016/j.bpj.2010.01.012.

[7] L. Kaler, E. Iverson, S. Bader, D. Song, M.A. Scull, G.A. Duncan, Influenza A virus diffusion through mucus gel networks, Commun. Biol. 5 (2022) 1–9. https://doi.org/10.1038/s42003-022-03204-3.

[8] N.A. Licata, B. Mohari, C. Fuqua, S. Setayeshgar, Diffusion of Bacterial Cells in Porous Media, Biophys. J. 110 (2016) 247–257. https://doi.org/10.1016/j.bpj.2015.09.035.

[9] S.S. Olmsted, J.L. Padgett, A.I. Yudin, K.J. Whaley, T.R. Moench, R.A. Cone, Diffusion of macromolecules and virus-like particles in human cervical mucus, Biophys. J. 81 (2001) 1930–1937. https://doi.org/10.1016/S0006-3495(01)75844-4.

[10] R. Bansil, B.S. Turner, The biology of mucus: Composition, synthesis and organization, Adv. Drug Deliv. Rev. 124 (2018) 3–15. https://doi.org/10.1016/j.addr.2017.09.023.

[11] R. Bansil, B.S. Turner, Mucin structure, aggregation, physiological functions and biomedical applications, Curr. Opin. Colloid Interface Sci. 11 (2006) 164–170. https://doi.org/10.1016/j.cocis.2005.11.001.

[12] M. Cohen, R. Schooley, M. Cohen, X. Zhang, H.P. Senaati, H. Chen, N.M. Varki, R.T. Schooley, Influenza A penetrates host mucus by cleaving sialic acids with neuraminidase Influenza A penetrates host mucus by cleaving sialic acids with neuraminidase, Virol. J. 10 (2013) 1. Virology Journal.

[13] X. Yang, L. Steukers, K. Forier, R. Xiong, K. Braeckmans, K. Van Reeth, H. Nauwynck, A beneficiary role for neuraminidase in influenza virus penetration through the respiratory mucus, PLoS One. 9 (2014) e110026. https://doi.org/10.1371/journal.pone.0110026.

[14] Y. Thomas, G. Vogel, W. Wunderli, P. Suter, M. Witschi, D. Koch, C. Tapparel, L. Kaiser, Survival of influenza virus on banknotes, Appl. Environ. Microbiol. 74 (2008) 3002–3007. https://doi.org/10.1128/AEM.00076-08.

[15] K. Lin, C.R. Schulte, L.C. Marr, Survival of MS2 and Φ6 viruses in droplets as a function of relative humidity, pH, and salt, protein, and surfactant concentrations, PLoS One. 15 (2020) e0243505. https://doi.org/10.1371/journal.pone.0243505.

[16] B. Keshavarz, E.C. Houze, J.R. Moore, M.R. Koerner, G.H. McKinley, Rotary atomization of newtonian and viscoelastic liquids, Phys. Rev. Fluids. 5 (2020). https://doi.org/10.1103/PhysRevFluids.5.033601.

[17] B. Keshavarz, E.C. Houze, J.R. Moore, M.R. Koerner, G.H. McKinley, Ligament Mediated Fragmentation of Viscoelastic Liquids, Phys. Rev. Lett. 117 (2016) 1–6. https://doi.org/10.1103/PhysRevLett.117.154502.

[18] B. Keshavarz, Nonlinear dynamics of complex fluids in fragmentation and fracture, (2017) 337. http://hdl.handle.net/1721.1/113546.

[19] B. Keshavarz, V. Sharma, E.C. Houze, M.R. Koerner, J.R. Moore, P.M. Cotts, P. Threlfall-Holmes, G.H. McKinley, Studying the effects of elongational properties on atomization of weakly viscoelastic solutions using Rayleigh Ohnesorge Jetting Extensional Rheometry (ROJER), J. Nonnewton. Fluid Mech. 222 (2015) 171–189. https://doi.org/10.1016/j.jnnfm.2014.11.004.

[20] G.H. McKinley, Visco-elasto-capillary thinning and break-up of complex fluids, Rheol. Rev. 3 (2005) 1–48.

[21] D.F. Rogers, Airway Mucus Hypersecretion in Asthma and COPD: Not the Same?, in: Airw. Dis., 2009: pp. 211–223. https://doi.org/10.1016/B978-0-12-374001-4.00017-1.

[22] C.E. Wagner, B.S. Turner, M. Rubinstein, G.H. McKinley, K. Ribbeck, A Rheological Study of the Association and Dynamics of MUC5AC Gels, Biomacromolecules. 18 (2017) 3654–3664. https://doi.org/10.1021/acs.biomac.7b00809.

[23] C.E. Wagner, G.H. McKinley, Age-dependent capillary thinning dynamics of physically-associated salivary mucin networks, J. Rheol. (N. Y. N. Y). 61 (2017) 1309–1326. https://doi.org/10.1122/1.4997598.

[24] C.E. Wagner, M. Krupkin, K.B. Smith-Dupont, C.M. Wu, N.A. Bustos, K. Ribbeck, A comparison of the physicochemical properties of native mucus and reconstituted mucin gels, 24 (2022) 628–639. https://doi.org/10.1021/acs.biomac.2c01016.

[25] M.S. van Deen, T. Bertrand, N. Vu, D. Quéré, E. Clément, A. Lindner, Particles accelerate the detachment of viscous liquids, Rheol. Acta. 52 (2013) 403–412. https://doi.org/10.1007/s00397-013-0691-9.

[26] R.J. Furbank, J.F. Morris, An experimental study of particle effects on drop formation, Phys. Fluids. 16 (2004) 1777–1790. https://doi.org/10.1063/1.1691034.

[27] H. Yoo, C. Kim, Generation of inkjet droplet of suspension in polymer solution, Korea Aust. Rheol. J. 27 (2015) 137–149. https://doi.org/10.1007/s13367-015-0014-z.

[28] H. Han, C. Kim, Extensional behavior of rod suspension in dilute polymer solution, Korea Aust. Rheol. J. 27 (2015) 197–206. https://doi.org/10.1007/s13367-015-0020-1.

[29] O. Lieleg, C. Lieleg, J. Bloom, C.B. Buck, K. Ribbeck, Mucin biopolymers as broad-spectrum antiviral agents, Biomacromolecules. 13 (2012) 1724–1732. https://doi.org/10.1021/bm3001292.Mucin.

[30] J. Dinic, Y. Zhang, L.N. Jimenez, V. Sharma, Extensional Relaxation Times of Dilute, Aqueous Polymer Solutions, (2015). https://doi.org/10.1021/acsmacrolett.5b00393.

[31] B.H. Cao, M.W. Kim, Molecular weight dependence of the surface tension of aqueous poly(ethylene oxide) solutions, Faraday Discuss. 98 (1994) 245–252. https://doi.org/10.1039/FD9949800245.

[32] G.H. McKinley, Dimensionless Groups For Understanding Free Surface Flows of Complex Fluids, SOR Rheol. Bull. (2005) 1–8. http://citeseerx.ist.psu.edu/viewdoc/download?doi=10.1.1.516.6467&rep=rep1&type=pdf.

[33] G.H. McKinley, M. Renardy, Wolfgang von Ohnesorge, Phys. Fluids. 23 (2011). https://doi.org/10.1063/1.3663616.

[34] J. Witten, K. Ribbeck, The particle in the spider's web: Transport through biological hydrogels, Nanoscale. 9 (2017) 8080–8095. https://doi.org/10.1039/c6nr09736g.

[35] R. Sender, Y.M. Bar-On, S. Gleizer, B. Bernshtein, A. Flamholz, R. Phillips, R. Milo, The total number and mass of SARS-CoV-2 virions, Proc. Natl. Acad. Sci. U. S. A. 118 (2021) 1–9. https://doi.org/10.1073/pnas.2024815118.

[36] R. Wölfel, V.M. Corman, W. Guggemos, M. Seilmaier, S. Zange, M.A. Müller, D. Niemeyer, T.C. Jones, P. Vollmar, C. Rothe, M. Hoelscher, T. Bleicker, S. Brünink, J. Schneider, R. Ehmann, K. Zwirglmaier, C. Drosten, C. Wendtner, Virological assessment of hospitalized patients with COVID-2019, Nature. 581 (2020) 465–469. https://doi.org/10.1038/s41586-020-2196-x.

[37] N. Lee, P.K.S. Chan, D.S.C. Hui, T.H. Rainer, E. Wong, K. Choi, G.C.Y. Lui, B.C.K. Wong, R.Y.K. Wong, W. Lam, I.M.T. Chu, R.W.M. Lai, C.S. Cockram, J.J.Y. Sung, Viral Loads and Duration of Viral Shedding in Adult Patients Hospitalized with Influenza, J. Infect. Dis. 200 (2009) 492–500. https://doi.org/10.1086/600383.

[38] M. Marczynski, K. Jiang, M. Blakeley, V. Srivastava, F. Vilaplana, T. Crouzier, O. Lieleg, Structural Alterations of Mucins Are Associated with Losses in Functionality, Biomacromolecules. 22 (2021) 1600–1613. https://doi.org/10.1021/acs.biomac.1c00073.

[39] R. Harich, A. Deblais, A. Colin, H. Kellay, Depletion forces induce visco-elasto-capillary thinning of non-Brownian suspensions, Epl. 114 (2016) 0–6. https://doi.org/10.1209/0295-5075/114/58006.

[40] V. Thiévenaz, A. Sauret, The onset of heterogeneity in the pinch-off of suspension drops, Proc. Natl. Acad. Sci. U. S. A. 119 (2022) 1–9. https://doi.org/10.1073/pnas.2120893119.

[41] M. Roché, M. Aytouna, D. Bonn, H. Kellay, Effect of surface tension variations on the pinch-off behavior of small fluid drops in the presence of surfactants, Phys. Rev. Lett. 103 (2009). https://doi.org/10.1103/PhysRevLett.103.264501.

[42] J. Witten, K. Ribbeck, The particle in the spider's web: Transport through biological hydrogels, Nanoscale. 9 (2017) 8080–8095. https://doi.org/10.1039/c6nr09736g.

[43] E.Y.T. Chen, Y.C. Wang, C.S. Chen, W.C. Chin, Functionalized positive nanoparticles reduce mucin swelling and dispersion, PLoS One. 5 (2010). https://doi.org/10.1371/journal.pone.0015434.

[44] C.E. Wagner, B.S. Turner, M. Rubinstein, G.H. McKinley, K. Ribbeck, A Rheological Study of the Association and Dynamics of MUC5AC Gels, Biomacromolecules. 18 (2017)

3654–3664. https://doi.org/10.1021/acs.biomac.7b00809.

[45] T. Kuiken, J.K. Taubenberger, Pathology of human influenza revisited, Vaccine. 26 (2008) D59–D66. https://doi.org/10.1016/j.vaccine.2008.07.025.

[46] P. Dey, S.K. Saha, S. Sarkar, Study of the interactions of sneezing droplets with particulate matter in a polluted environment, Phys. Fluids. 33 (2021). https://doi.org/10.1063/5.0067517.

[47] H.T. Dao, K. Kim, Behavior of cough droplets emitted from Covid-19 patient in hostpial isolation room with different ventilation configurations, (2020).

[48] S. Berger, M. Mattern, J. Niessner, Face mask performance related to potentially infectious aerosol particles breathing mode and facial leakage, (2020).

[49] B. Chang, R.S. Sharma, T. Huynh, A. Kudrolli, Aerial mucosalivary droplet dispersal distributions with implications for disease mitigation, Phys. Rev. Res. 2 (2020). https://doi.org/10.1103/PhysRevResearch.2.043391.

[50] M. Rodríguez-Hakim, L. Räz, J. Vermant, Variations in human saliva viscoelasticity affect aerosolization propensity, Soft Matter. 18 (2022) 2528–2540. https://doi.org/10.1039/d1sm01581h.

[51] Z.Y. Han, W.G. Weng, Q.Y. Huang, Characterizations of particle size distribution of the droplets exhaled by sneeze Characterizations of particle size distribution of the droplets exhaled by sneeze, J. R. Soc. Interface. 10 (2013) 20130560.

[52] R. Bansil, J.P. Celli, J.M. Hardcastle, B.S. Turner, The influence of mucus microstructure and rheology in Helicobacter pylori infection, Front. Immunol. 4 (2013) 1–12. https://doi.org/10.3389/fimmu.2013.00310.

[53] R. Bansil, B.S. Turner, Mucin structure, aggregation, physiological functions and biomedical applications, Curr. Opin. Colloid Interface Sci. 11 (2006) 164–170. https://doi.org/10.1016/j.cocis.2005.11.001.

[54] E.S. Frenkel, K. Ribbeck, Salivary Mucins Protect Surfaces from Colonization by Cariogenic Bacteria, Appl. Environ. Microbiol. 81 (2015) 332–338. https://doi.org/10.1128/aem.02573-14.

[55] C.E. Wagner, Micro- and macro-rheological studies of the structure and association dynamics of biopolymer gels, PhD Thesis. (2018).

[56] E.S. Frenkel, K. Ribbeck, Salivary mucins protect surfaces from colonization by cariogenic bacteria, Appl. Environ. Microbiol. 81 (2015) 332–338. https://doi.org/10.1128/AEM.02573-14.

[57] N.L. Kavanaugh, A.Q. Zhang, C.J. Nobile, A.D. Johnson, K. Ribbeck, Mucins suppress virulence traits of Candida albicans, MBio. 5 (2014) e01911. https://doi.org/10.1128/mBio.01911-14.

[58] J.D. Berry, M.J. Neeson, R.R. Dagastine, D.Y.C. Chan, R.F. Tabor, Measurement of surface and interfacial tension using pendant drop tensiometry, J. Colloid Interface Sci. 454 (2015) 226–237. https://doi.org/10.1016/j.jcis.2015.05.012.

[59] A. Daerr, A. Mogne, ImageJ Plugin to Measure the Surface Tension from an Image of Pendent Drop, J. Open Res. Softw. 4 (2016) e3.

[60] R.H. Ewoldt, M.T. Johnston, L.M. Caretta, Experimental challenges of shear rheology: how to avoid bad data, Complex Fluids Biol. Syst. 7 (2015) 3866–3871. https://doi.org/10.1002/app.

[61] C.W. Macosko, Rheology: Principles, Measurements, and Applications, 1994.

[62] L.E. Rodd, T.P. Scott, J.J. Cooper-White, G.H. McKinley, Capillary break-up rheometry of low-viscosity elastic fluids, Appl. Rheol. 15 (2005) 12–27. https://doi.org/10.3933/ApplRheol-15-12.

[63] D.H. Kelly, N.T. Ouellette, Using particle tracking to measure flow instablities in an undergradaute laboratory experiment, Am. J. Phys. 79 (2011) 267–273.

[64] M. Manish, S. Sahu, Analysis of droplet clustering in air-assist sprays using Voronoi tessellations, Phys. Fluids. 30 (2018). https://doi.org/10.1063/1.5053473.

[65] J.S. Ferenc, Z. Néda, On the size distribution of Poisson Voronoi cells, Phys. A Stat. Mech. Its Appl. 385 (2007) 518–526. https://doi.org/10.1016/j.physa.2007.07.063.

[66] E. Villermaux. Fragmentation, Annu. Rev. Fluid Mech.39 (2007) 419-446.

[67] N. Bremond and E. Villermaux, Atomization by jet impact, J. Fluid Mech. 549 (2006) 273-306.

[68] A. Gaillard, R. Sijs, and D. Bonn, What determines the drop size in sprays of polymer solutions?, J. Non-Newton. Fluid Mech. 305 (2022) 104813.

5.7 Acknowledgements

We thank Jim Bales from MIT's Edgerton Center for access to the camera equipment used in this study and we thank him for his expertise on high-speed imaging.

5.8 Supplementary Materials

Supplementary Tables

Polymer type	Polymer concentration [% wt.]	Number of droplets per spray [average±s.d.]
PEO	0.1	1256±116
	0.3	310±30
	0.5	209±29
CMC	0.3	466±451
	0.5	928±824
	1.0	422±270
Muc5AC	0.5	235±72
	1.0	1052±309
	1.5	900±777
Buffer	0	109±27
Sigma	1.0	111±29
Saliva – Donor 1	-	55
Saliva – Donor 2	-	65
Saliva – Donor 3	-	228
Saliva – Donor 4	-	282

Supplementary Table S5.1 Number of droplets tracked with the high-speed imaging assay for each polymer solution and donor saliva. The average number of droplets tracked in three to four spray replicates and standard deviation (s.d.) are summarized for PEO, CMC, Muc5AC, Buffer, and Sigma mucin. The total number of droplets for the first spray in donor saliva is reported due to large differences in fragmentation for a given sample between several sprays.

Polymer solution	Particle Type	Particle concentration [% wt.]	Number of droplets per spray [average±s.d.]
1% CMC	C	0.001	433±215
	C	0.01	801±286
	C	0.1	764±242
	A	0.1	806±225
1% Muc5AC	C	0.001	200±186
	C	0.01	165±71
	C	0.1	583±235
	A	0.1	393±214

Supplementary Table S5.2 Number of droplets tracked with the high-speed imaging assay for 1% polymer solutions with varied concentrations of charged nanoparticles. The average number of droplets tracked in three to four spray replicates and standard deviation

(s.d.) are summarized for CMC and Muc5AC with different concentrations of aminated (A) and carboxylated (C) nanoparticles.

Supplementary Figures

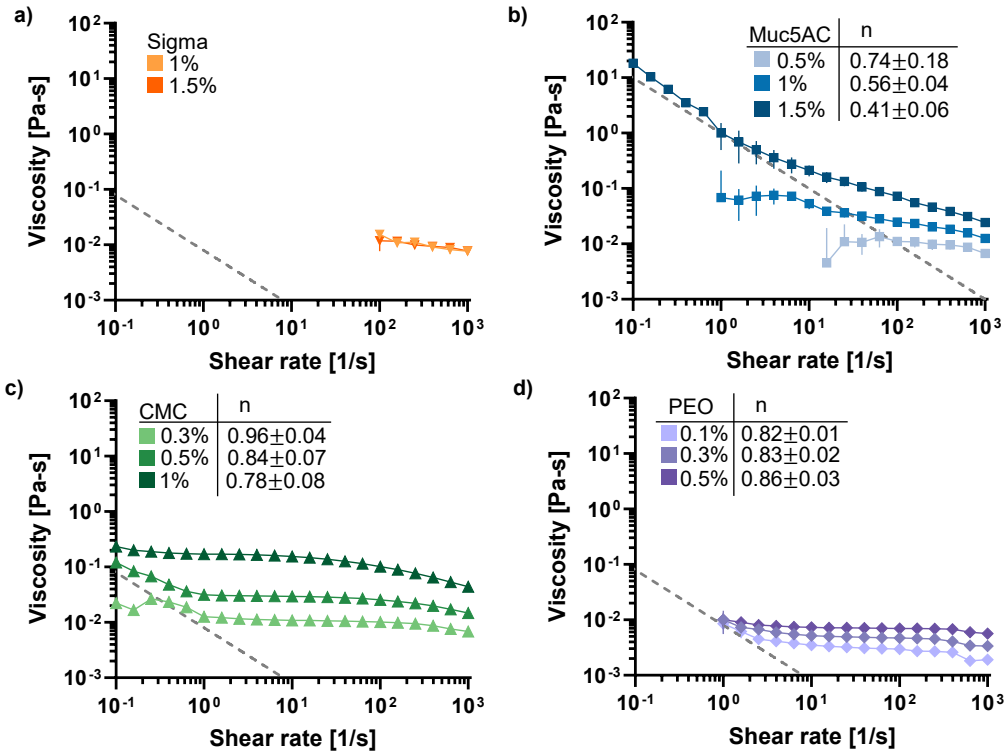

Supplementary Figure S5.1 Steady state shear viscosity of mucus polymer models. (a, b, c, d) Steady state shear viscosity as a function of shear rate for **a** Sigma **b** Muc5AC **c** CMC and **d** PEO. Each point represents the average of three replicates and the error bars indicate standard deviation (s.d.). Dashed line denotes the low torque limit for the ARES-G2 (8 mm parallel plate in **b** and 40 mm cone plate in **a, c,** and **d**). Shaded colors denote polymer concentration (see legend). The Carreau model (equation 5.1) was fitted to each replicate in **b-d** to extract the power law index (n) for each polymer concentration. The average and s.d. of the power law index are summarized in the tables corresponding to each polymer. The Carreau model was not fitted to the flow curves of Sigma mucin.

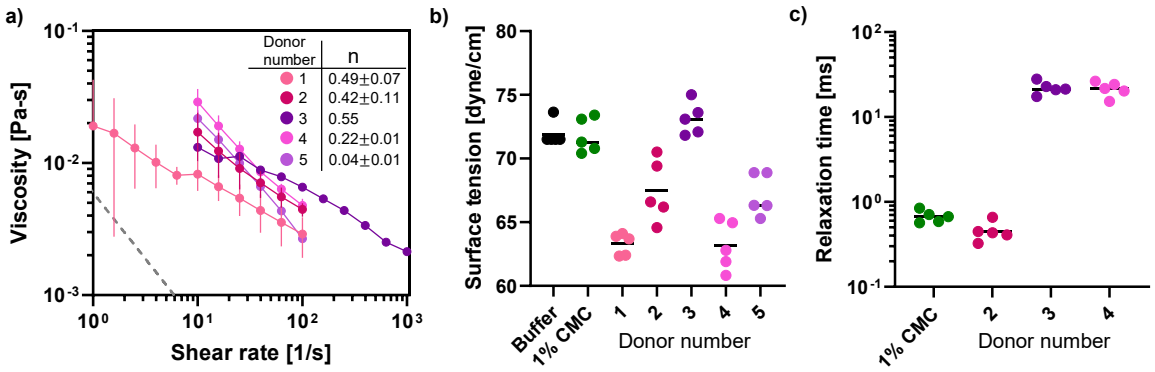

Supplementary Figure S5.2 Rheological properties of mucosalivary fluid from human volunteers. a Steady state shear flow viscosity measurements of mucosalivary fluid from 5 donors. Dashed line denotes the instrument low torque limit for the ARES-G2 with a 40 mm cone plate. Each point represents the average of two to four replicates and the error bars indicate standard deviation. The Carreau model (equation 5.1) was fitted to each replicate to extract the power law index (n) for each donor. The average and s.d. of the power law index are summarized in the table. The Carreau model was not fitted to the flow curves of Sigma mucin. **(b,c) b** Surface tension for five donors (shades of pink and purple circles) compared to buffer (black circle) and 1% CMC (green circle) and **c** Relaxation time for 3 donors (shades of pink and purple circles) compared to 1% CMC (green circle). Each point represents a repeat measurement and the horizontal line represents the average.

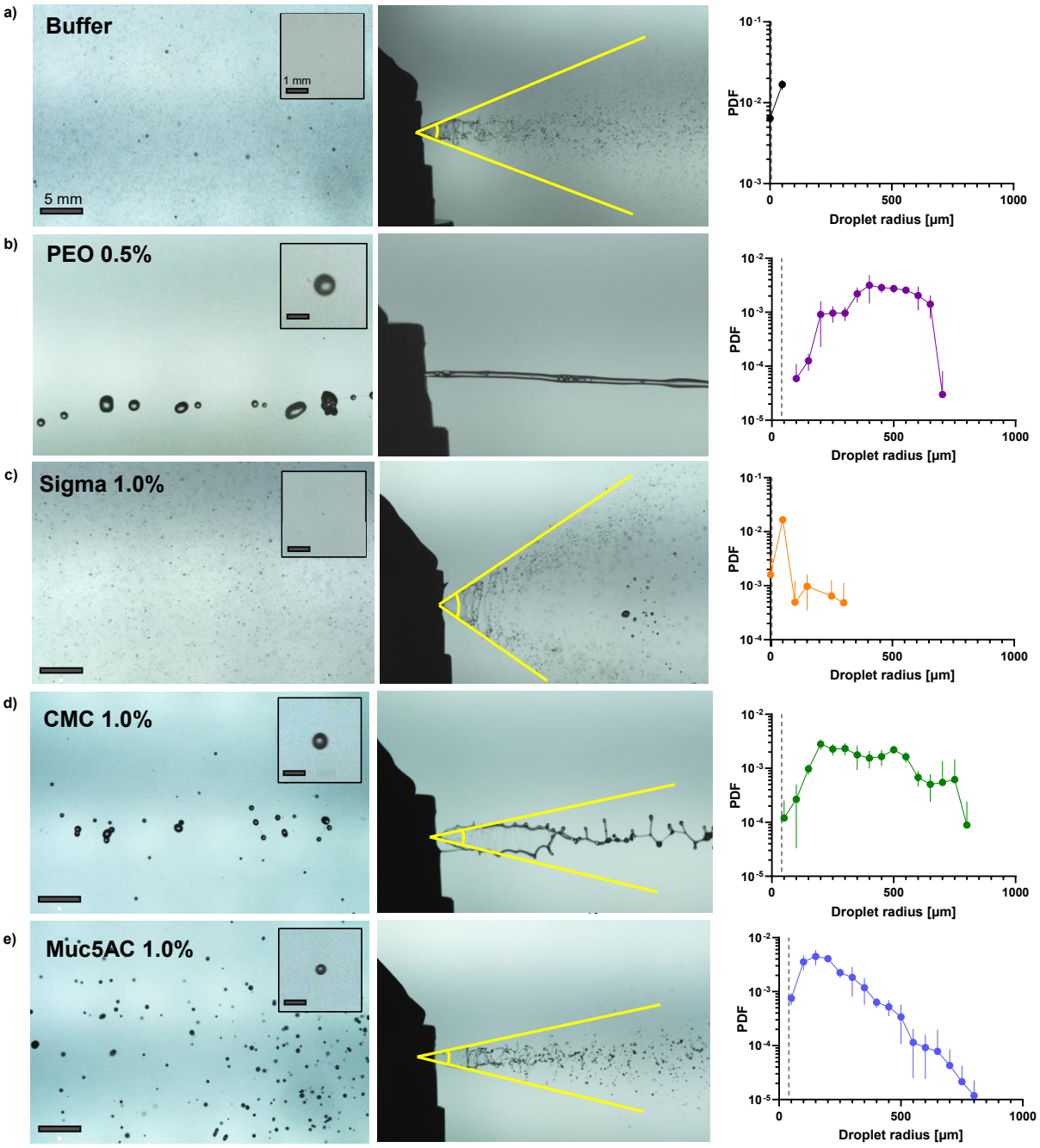

Supplementary Figure S5.3 High-speed (HS) camera examples of mucus polymer models and respective droplet size distributions. Left most column are HS images of sprays (**a** buffer, **b** 0.5% PEO, **c** 1% Sigma, **d** 1% CMC, and **e** 1% Muc5AC gels) with a picture inset of an average sized droplet. Scale bars in insets are 1 mm. Middle column are HS images at the nozzle head illustrating spray cone angle (yellow lines). Right most are the respective droplet size distributions (PDFs). The dashed lines in the PDFs correspond to the minimum camera resolution. Note that the resolution for buffer and 1% Sigma is approximately 5 μm and the resolution for 0.5% PEO, 1% CMC, and 1% Muc5AC is approximately 40 μm. Each point in the PDFs represents the average of three or more replicates and the error bars indicate standard deviation.

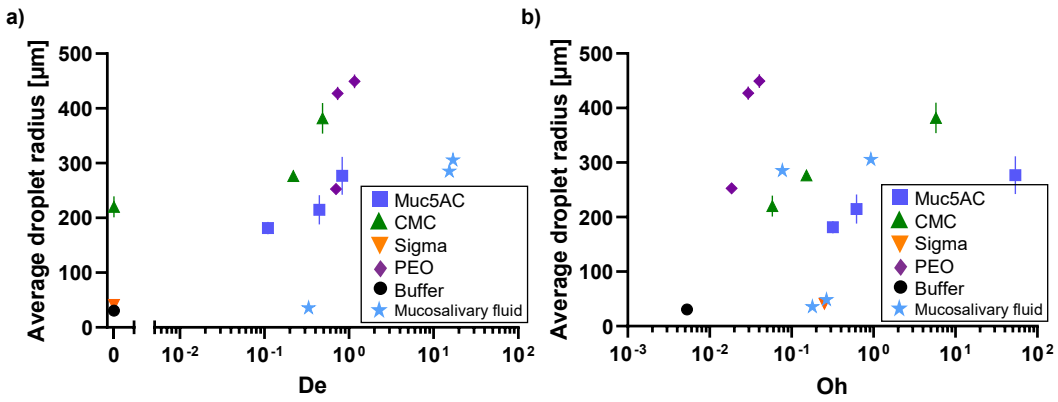

Supplementary Figure 5.4 Average droplet radius as a function of dimensionless numbers. (a, b) Average droplet radius as a function of the **a** Deborah number (De) and **b** Ohnesorge number (Oh) for polymer solutions and mucosalivary fluid from donors. Dimensionless numbers are defined as follows: De = $\frac{\lambda}{\sqrt{\frac{\rho L^3}{\sigma}}}$ and Oh = $\frac{\eta}{\sqrt{\rho \sigma L}}$, where λ is relaxation time, ρ is fluid density, σ is surface tension, η is zero shear viscosity, and L is the nozzle diameter. Polymer solutions are distinguished by color and symbol as follows: Muc5AC (blue squares), CMC (green triangles), Sigma (orange inverted triangles), PEO (purple diamonds), buffer (black circles), and mucosalivary fluid (light blue stars).

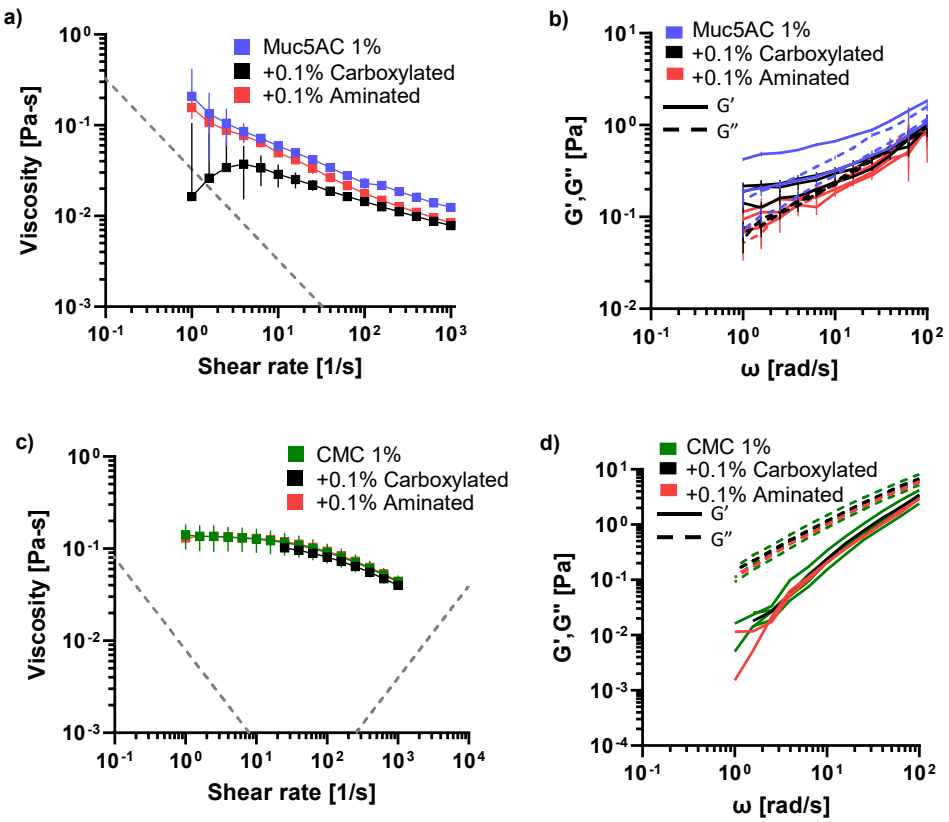

Supplementary FigureS5.5 Steady state and oscillatory shear measurements with nanoparticles. a Steady state shear flow viscosity of 1% Muc5AC gels with and without nanoparticle suspensions. Dashed line denotes the instrument flow limit for the ARES-G2 with a 25 mm parallel plate. Each point represents the average of three replicates and the error bars indicate standard deviation (s.d.). **b** SAOS results for 1% Muc5AC gels with and without nanoparticle suspensions. Solid lines denote the storage modulus (G') and dashed line denotes the loss modulus (G"). Error bars indicate s.d. of three replicates. **c** Steady state shear flow viscosity of 1% CMC with and without nanoparticle suspensions. Dashed line denotes the instrument flow limit for the ARES-G2 with a 25 mm parallel plate. Each point represents the average of three replicates and the error bars indicate s.d. **d** SAOS results for 1% CMC with and without nanoparticle suspensions. Solid lines denote the storage modulus (G') and dashed line denotes the loss modulus (G"). Error bars indicate s.d. of three replicates.

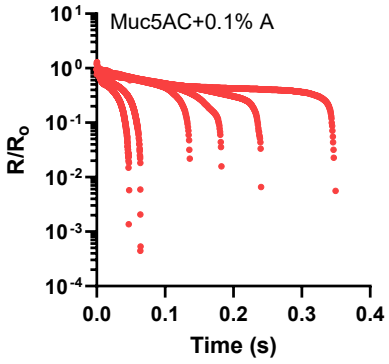

Supplementary Figure S5.6 Non-dimensional radius evolution of aminated nanoparticles in 1% Muc5AC gels. Non-dimensional radius evolution of liquid threads under capillary-driven thinning for 1% Muc5AC gels containing 0.1% aminated nanoparticles. Each curve represents a replicate (n=6).

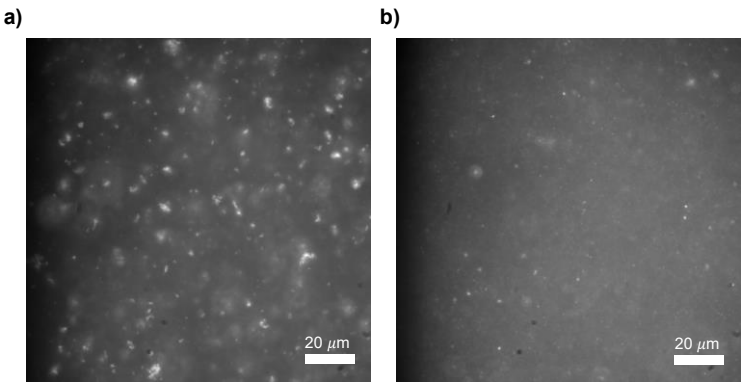

Supplementary Figure S5.7 Aminated nanoparticles form aggregates. (a, b) Microscopy image of **a** 0.1% aminated 200 nm diameter nanoparticles and **b** 0.1% carboxylated 200 nm diameter nanoparticles in 10 mM sodium phosphate buffer.

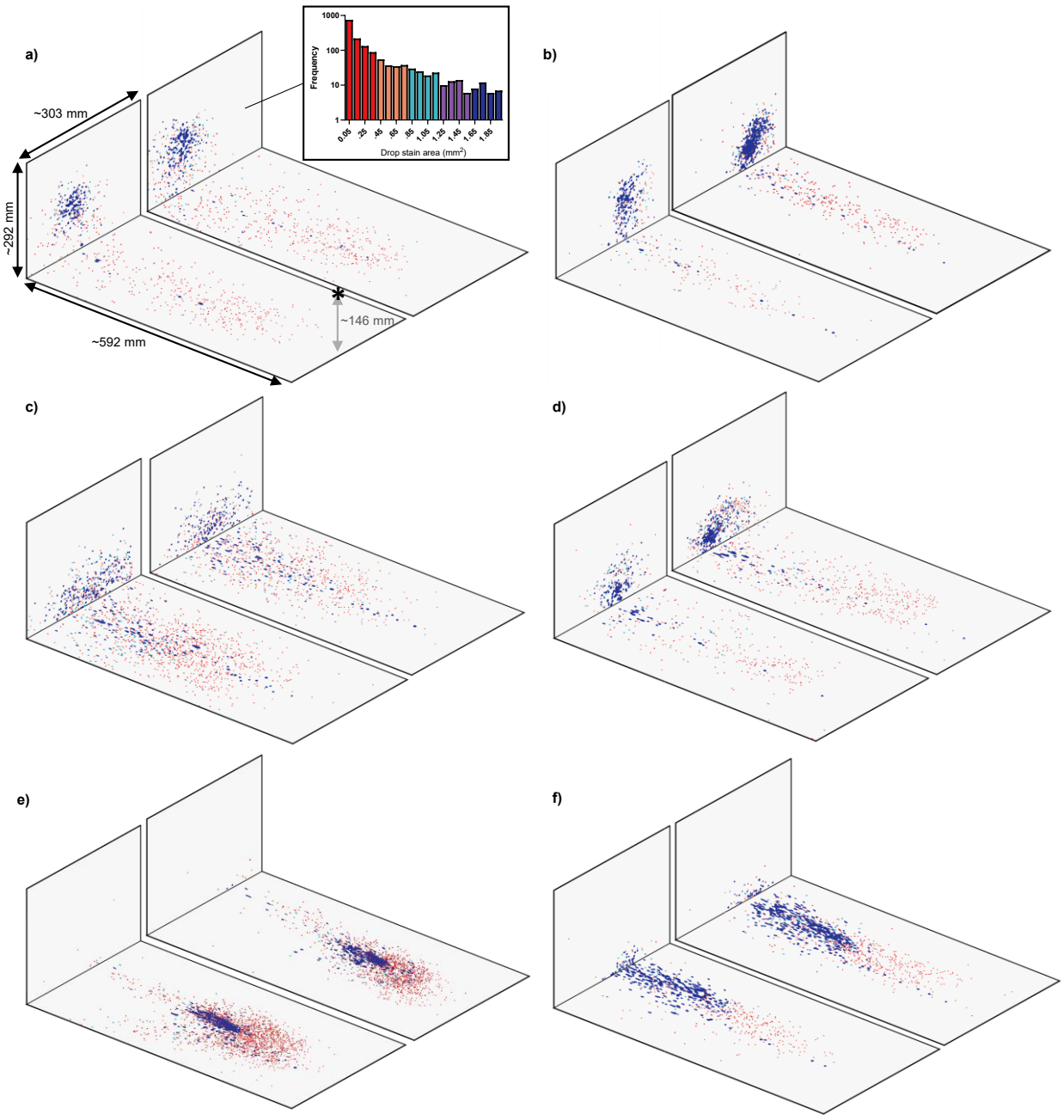

Supplementary Figure S5.8 Example stain assay plots for 1% Muc5AC gels and 1% CMC with and without nanoparticles. Stain assays of **a** 1% Muc5AC gels, **b** 1% CMC, **c** 1% Muc5AC gels with 0.1% carboxylated (C) 200 nm diameter nanoparticles, **d** 1% CMC with 0.1% C nanoparticles, **e** 1% Muc5AC gels with 0.1% aminated (A) 200 nm diameter nanoparticles, and **f** 1% CMC with 0.1% A. Stains in **a-f** are assigned different colors according to their size. The drop stain area histogram in **a** shows the colors that correspond to a given stain size for the indicated stain (black line from histogram to stain assay plot). Sprays in **a-f** are sprayed through the spray inlet which is marked by the asterisk in **a** (the center of the front wall of the chamber).

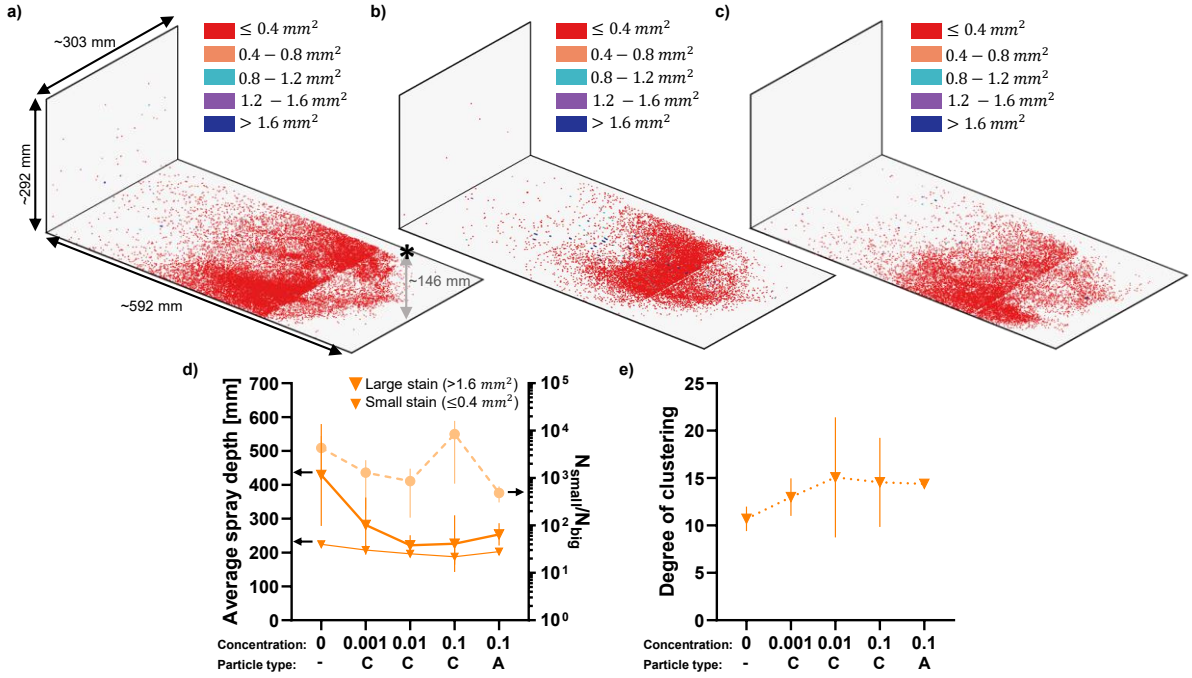

Supplementary Figure S5.9 Stain assay plots and spatial dispersion of 1% Sigma mucin with and without nanoparticles. Stain assay plots of **a** 1% Sigma, **b** 1% Sigma and 0.1% carboxylated nanoparticles, and **c** 1% Sigma and 0.1% aminated nanoparticles. Stains in a-c are assigned different colors according to their size (see legend). Sprays in **a-c** are sprayed through the spray inlet which is marked by the asterisk in **a** (the center of the front wall of the chamber). **d** Average spray depth (solid lines) of small stains ($\leq 0.4\ mm^2$) and large stains ($> 1.6\ mm^2$) and ratio of number of big to small stains (dashed lines) of 1% Sigma with varied concentrations of carboxylated (C) and aminated (A) particles. Each point represents the average of three replicates and the error bars indicate standard deviation (s.d.). **e** Degree of clustering of stains from sprays of 1% Sigma with different nanoparticle concentrations. Each point represents the average of three replicates and the error bars indicate s.d.

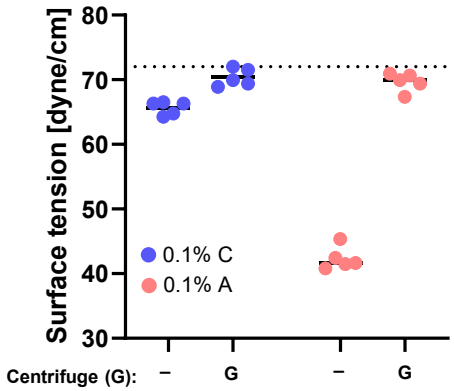

Supplementary Figure S5.10 Effect of centrifugation on the surface tension of nanoparticle suspensions. Plotted is the surface tension of 0.1% carboxylated (C) and 0.1% aminated (A) nanoparticles suspended in 10 mM sodium phosphate buffer. Centrifugation (G) was done to remove the nanoparticle aqueous solution (see Methods). Nanoparticles were resuspended and vortexed in 10 mM sodium phosphate buffer to their final concentration. The dotted line represents the surface tension of 10 mM sodium phosphate buffer alone. Each point represents a repeat measurement and the horizontal line represents the average (n=5).

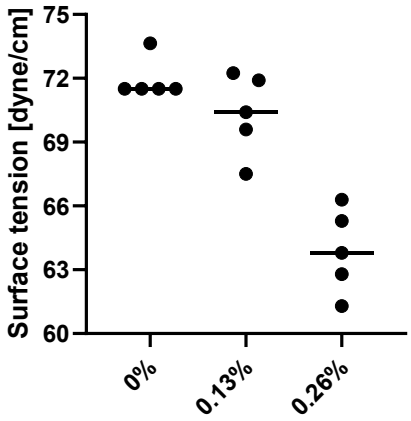

Supplementary Figure S5.11 Effect of Rhodamine B concentration on the surface tension of buffer. Plotted is the surface tension of 10 mM sodium phosphate buffer with different concentrations of Rhodamine B (Thermo Fisher Scientific, Waltham, MA, USA). Each point represents a repeat measurement and the horizontal line represents the average (n=5).

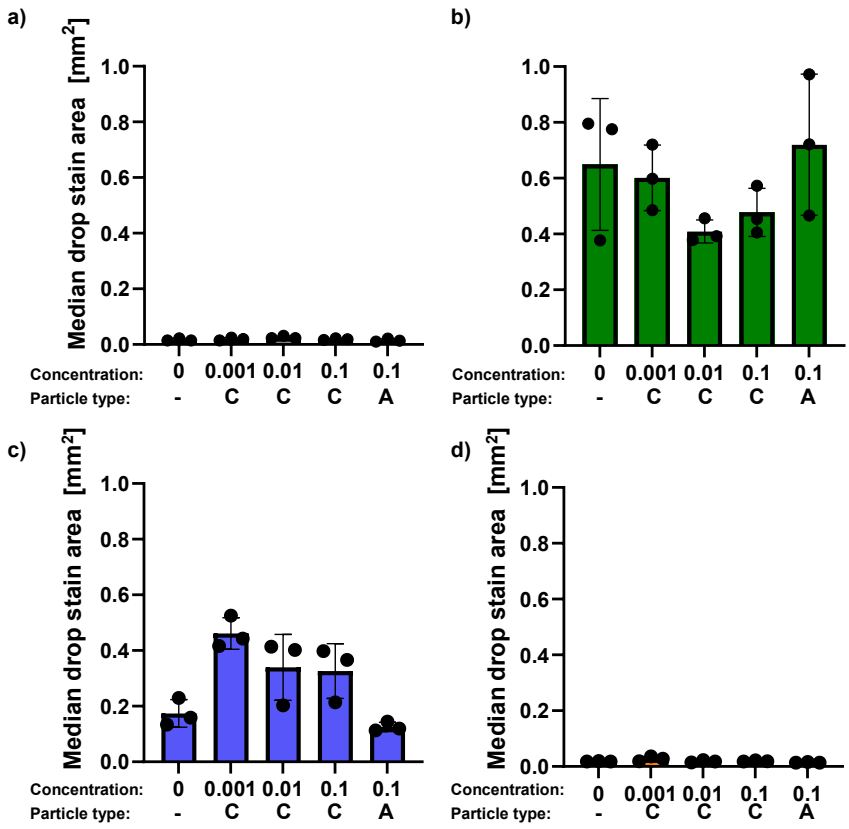

Supplementary Figure S5.12 Median drop stain area of sprayed mucus polymer models with and without nanoparticles. (a, b, c, d) Median drop stain area of **a** buffer, **b** 1% CMC, **c** 1% Muc5AC, and **d** 1% Sigma with different concentrations of carboxylated (C) and aminated (A) nanoparticles. Solutions contained 0.13% Rhodamine B solution which stained solutions a violet color. Each point represents a replicate and the error bars represent the standard deviation (n=3).

Chapter 6

Conclusions and future directions

The studies covered in this thesis highlight the importance of mucin-pathogen interactions in shaping outcomes of disease processes. Broadly, we demonstrate that mucin's physical and biochemical properties are a key feature of mucus that not only determine the ability of pathogens to penetrate mucus, but also modulates the formation and spread of pathogen-laden mucus droplets. In **Chapter 2**, we reviewed mucus' physicochemical properties and its influence on viral transport and transmission. In **Chapter 3**, we studied the transport of a semi-wild type virus system, bacteriophage, in mucin gels. We found that phage transport was influenced by hydrodynamic diameter, charge, and surface chemistry. We additionally found that step size distributions distinguished transport in different mucin types, and that diffusive transport across phage types was associated with a range of underlying step size distributions, ranging from Gaussian to non-Gaussian. Our observations of diversity in phage transport profiles through mucin gels despite similarities in their size and zeta potential suggest that such variation may also exist among human viruses. Indeed, it is believed that several human respiratory viruses (e.g., influenza, human coronaviruses) have evolved binding proteins important to their replication that also recognize certain mucin sites (e.g., sialic acid), which may differentially impact their transport profiles and, consequently, lead to differences in viral infection kinetics and transmissibility. In **Chapter 4**, we reviewed experimental techniques and the theoretical background relevant to performing macrorheological measurements on mucin gels. We then applied theoretical and experimental concepts to the study of mucin aerosolization. In **Chapter 5**, we studied the droplet size and spatial spread of sprayed reconstituted mucin gels using high speed imaging and a developed stain assay. We used macrorheological techniques to interrogate how physical properties of mucus and mucus polymer models containing particle loads modulate spray characteristics including spread in the air and deposition. We found that lab-purified native mucins and charged particles modulate the breakup and final droplet size distribution during spraying in a unique way compared to other mucus model polymers, including industrially purified Sigma mucins. These findings have important implications for disease transmission but also to drug development. Saline and mucolytics are often used to clear infection faster by loosening mucus. They are also associated

with reducing viral load which is attributed to various mechanisms such as improved mucociliary clearance and inhibition of viral replication (specifically, viruses sensitivity to high salt concentrations). While this may be beneficial to the host, altering the properties of the mucosal layer may change the transmissibility of the infection by altering the production or modifying the dispersion of generated droplets. Indeed, our findings suggest that decreasing the elasticity of fluids decreases the average size of generated droplets upon aerosolization. On the other hand, we found that adding aminated particles to the biopolymer solutions created droplets that clustered proximally to each close to the exit point of the spray. In light of this, an important and interesting future direction for this work will be to incorporate a native virus system into the biopolymer solutions to study fragmentation dynamics as well as to evaluate viral viability and quantify pathogen load in sprayed droplets. Doing so will enable us to assess transmission risks under different scenarios and develop disease transmission mitigating strategies.

Although the significance of mucus to disease progression and transmission is being increasingly recognized, the incorporation of all mucus properties (e.g., mechanical, biological, and chemical) in experiments remains technically challenging. Throughout this thesis, we use reconstituted mucin gels to model native mucus from different mucosal niches. However, there are several aspects of host physiology that are not captured in our mucin gel models. For example, mucosal niches in the body like the respiratory tract contain a combination of several mucins (e.g., Muc5AC, Muc5B, Muc7). Unlike the harvesting of Muc5AC from animal sources, Muc5B is harvested from human sources which often has lower yields of purified mucin. The limited availability of Muc5B makes it difficult to use in aerosolization experiments like those performed in this study which required several hundred microliters of solution. Native mucus also contains non-mucin components such as surfactants and several types of ions, which can influence both microscale and macroscale properties of mucus (e.g., alter hydrophobic crosslinks of mucin network structure, electrostatic screening interactions, macrorheological properties, etc.). In addition, while our system reflected the viscosity of human mucosalivary fluid, the range of elasticity seen in native mucosalivary fluid was not recapitulated in reconstituted mucin gels, yet, this is an important property that affects droplet formation. Indeed, highly elastic saliva produced larger droplets than samples with low elasticity. In addition, our in vitro system is a static system whereas in-host environment, the mucosal environment is dynamic: cilia protruding from epithelial cells beat to actively move invading pathogens out of the airways and mucus is constantly being produced and shed. Our model system allowed us to isolate the contributions of mucin alone. However, future work may incorporate other aspects of the airway environment in order to investigate mucosal-pathogen interactions in a more

physiologically complete context. Doing so would also allow for the incorporation of mucus representative of different diseased states; for example, comparing healthy mucus to mucus observed in chronic disease (e.g., asthma, COPD, or cystic fibrosis) or respiratory infectious disease.

While there are several areas of future work, our work has set the groundwork for the development of theoretical and experimental frameworks for incorporating mucosal biophysics and mucin/pathogen interactions into the study of disease processes and transmission. The two studies in this thesis highlight that the physicochemical properties of mucin gels play important roles across multiple length-scales, both within-hosts and at the point of transmission. We expect that the findings of this thesis will contribute to the development of biophysically informed disease models and guide the development of rationally designed materials and therapeutics with specific mucin-interaction profiles.

.